Understanding the Combustion Chemistry of Siloxanes: Reaction Kinetics and Fuel Interactions

by

Rachel A Schwind

A dissertation submitted in partial fulfillment
of the requirements for the degree of
Doctor of Philosophy
(Mechanical Engineering)
The University of Michigan
2019

Doctoral Committee:

Professor Margaret S. Wooldridge, Chair
Professor Johannes W. Schwank
Dr. Robert S. Tranter, Argonne National Laboratory
Professor Angela Violi

Rachel Schwind

schwinra@umich.edu

ORCID iD: 0000-0002-0116-3894

Dedication:

"To those who saw the potential in me when I didn't and those

who reminded me to breathe when I forgot how."

Acknowledgements

The following is the result of just over four years of work which would not have been possible to complete on my own. Whether it be through technical insights or support and friendship, many individuals have contributed to the success of this work.

First, I would like to thank my advisors, Professor Margaret Wooldridge and Dr. Robert Tranter, for supporting me in all of my research endeavors both technical and educational. Both have been immensely supportive of my career goals and helped put me in situations to help best prepare me for the next steps. While both of them encourage me to push myself technically, they have also been sure to encourage me to pursue a healthy work life balance and cultivate my myriad of interests outside of research. I could not have asked for a better advisors to support my technical and professional growth. I cannot think them enough for their candid insights and generous support over the years.

Additionally, I would like to thank Professor Johannes Schwank and Professor Angela Violi for serving on my committee. Their support of this work has been greatly appreciated and their insights have been valuable in recognizing ways to frame this research in the broader community as well as carry it forward. Further, I would like to thank Dr. Raghu Sivaramakrishnan for his guidance and contributions to the model development.

I don't know how I would have survived the past few years without the support and friendship of my current and former labmates. Dr. Mohammad Fatouraie, Dr. Scott Wagnon, Dr. Cesar Barraza Botet and Dr. Andrew Mansfield served as amazing teachers to help get me started on my research journey at UM. Dr. Dimitris Assanis, Dr. Ripudaman Singh, Dr. Luis

Gutierrez, Mario Medina and Miles Burnett served as great colleagues and friends and I owe them thanks for the many insightful conversations whether it be bouncing around technical ideas or discussing the latest happenings in sports and fitness or contemplating politics and philosophy.

I also owe many thanks to the amazing staff in the ME department from the wonderful ASO teams (both administrative and academic) to the amazing ME-IT staff. A special thank you to both Matt Navarre and Matt Jastrzembowski for their help through the renovation headaches and lab flood crisis. Everyone's positive attitudes and support has made the UM ME department a great place to work and provided some breaks and smiles during the occasionally long and grueling days.

Additionally, a thank you to my colleagues at Argonne for helping me always feel welcome and a part of the community. Especially my officemates, Dr. John Randazzo and Dr. Travis Sikes, for their help in working through ideas and also comradery during my stays at ANL. A further thank you to the larger Gas Phase Chemical Dynamics Group and support staff for always making me feel welcome at ANL and the many lively discussions over lunch and coffee.

I owe special thanks to my various gym families over the years who have helped me find a stress relieving outlet no matter where I happen to be. From the lifting group at the UM Rec centers to my boxing family at Bodyshot, I have always had a welcoming place to unwind and clear my head.

Finally, I can't thank my family and friends enough for their support and understanding over this time. There were many ups and downs throughout this process and you all were there to make sure I made it through them all whether it was joining in celebration or offering a shoulder to lean on. To my Ann Arbor friends who became family, I owe immense thanks for all the love

and support. To the friends made along my travels, a thank you for being a source of support and laughs no matter where we find ourselves. To the friends who have been around since before we were old enough to vote, an earnest thank you for being a source of never ending love and support no matter how far apart we are. To my family, thank you for always being there and putting up with my crazy schedules and stress. I am fortunate to have such an amazing and loving support system for which I will be eternally grateful. I could not have accomplished this without it.

Funding Acknowledgements:

This work has been generously funded by various agencies including the University of Michigan, University Turbine Systems Research program under National Energy Technologies Laboratory, National Science Foundation, U.S. Department of Energy Office of Basic Energy Sciences award DE-SC0019184 and based on work supported by the U.S. Department of Energy Office of Science, Office of Science Graduate Student Research (SCGSR) program which is administered by the Oak Ridge Institute for Science and Education (ORISE) for the DOE by ORAU under contract number DE-SC0014664. Additionally, this research used resources of the Advanced Light Source, a DOE Office of Science User Facility under contract no. DE-AC02-05CH11231.

Table of Contents

List of Tables

List of Figures

List of Appendices

Abstract

This work explores the reaction kinetics of three complimentary organosilicon structures important to waste-to-energy and material synthesis applications. The chemical kinetics of the siloxane compounds were investigated using oxidation/auto-ignition and pyrolysis/thermal decomposition experiments. The twofold approach enabled a large range of state conditions and reaction chemistries to be studied, often for the first time. The effects of trimethylsilanol (TMSO) and hexamethyldisiloxane (HMDSO) on syngas (H_2 and CO) auto-ignition behavior at temperatures of 1010 – 1070 K and pressures of 8 to 10.3 atm were quantified using a rapid compression facility (RCF). Trace concentrations of TMSO (100 ppm, mole basis) and HMDSO (100 ppm) were added to a surrogate syngas mixture of CO and H_2 (with a molar ratio of 2.34:1), air levels of dilution, with molar equivalence ratio of $\phi = 0.1$). The measured ignition delay times showed both siloxane species dramatically promoted reactivity of the H_2 and CO reactants as indicated by reduced ignition delay times, with TMSO decreasing ignition delay times by approximately 37% and HMDSO decreasing ignition delay times by approximately 50% compared with the reference syngas mixture which contained no siloxanes. HMDSO also demonstrated a marked increase in energy release with an increase in pressure rise of approximately 20% compared with the reference syngas mixture.

The thermal decomposition behavior of three organosilicon species, TMSO, HMDSO and hexamethylcyclotrisiloxane (HMCTSO), was investigated using two shocktube facilities: a diaphragmless shocktube (DFST) and a unique high-repetition rate shocktube (HRRST). This

work provided first-of-their-kind laser schlieren densitometry results for understanding the thermal effects of the decomposition process. All three siloxane compounds demonstrated strongly endothermic behavior. Time-resolved speciation data were also obtained during the pyrolysis experiments using time-of-flight mass spectrometry (TOF-MS). The first-of-their-kind data provided vital new information at conditions not studied previously. Additionally, TOF-MS experiments using photo-ionization energy from a synchrotron facility provided further insights into the species relevant for thermal decomposition. The data showed the HMDSO, TMSO and HMCTSO do not decompose into smaller silicon based intermediates, as expected based on the limited information on these species available in the literature. Instead, small hydrocarbons were observed as were spectra attributable to larger stable siloxane species.

The results of the oxidation and thermal decomposition experimental studies were used to propose and test hypotheses for siloxane reaction pathways important for this class of compounds. Importantly, the experimental data indicate significant reactivity at combustion conditions which may be attributed, in part, to increased production of the OH radical pool. However, the results also indicate direct reactions with the siloxane compounds or silicon-containing intermediates may be necessary to explain the observed behaviors.

Chapter 1: Combustion of Organosilicon Compounds

1. Introduction

Siloxanes are a subgroup of organosilicon compounds which contain Si-O-Si linkages. Siloxanes are increasing used in industrial and commercial applications due to their low thermal conductivity, high flexibility, and hydrophobicity. Research into these compounds as precursors for synthesizing silica products such as nano-particles and surface coatings [1] has been growing significantly in recent years. They are especially of interest in the semi-conductor industry as they can make up the backbone of many silicone polymers. A barrier to development in this area has been the lack of fundamental studies and understanding of the behavior of siloxane species.

In order to address the gaps in understanding, the chemical kinetics of three compounds representative of the common structures found in this class were investigated. Two experimental strategies were used for the studies. First, the effects of siloxanes on the auto-ignition properties of syngas (CO and H_2) were quantified using a rapid compression facility. Second, the thermal decomposition of the siloxanes were investigated through shocktube pyrolysis experiments. Three compounds were studies: hexamethyldisiloxane, trimethylsilanol and hexamethylcyclotrisiloxane. Table 1.1 shows key properties for the compounds while Table 1.2 shows the experimental methods explored in this work for each compound.

Table 1.1 Key properties of the siloxane compounds of interest in this study

	Hexamethyldisiloxane HMDSO	Trimethylsilanol TMSO	Hexamethylcyclotrisiloxane HMCTSO
Formula	$(CH_3)_3SiOSi(CH_3)_3$	$Si(CH_3)_3OH$	$Si_3O_3(CH_3)_6$
Structure		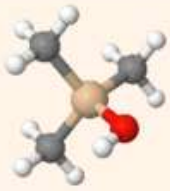	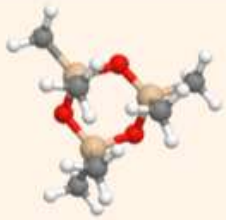
Molecular Weight	162	90	222
Number of Si Atoms	2	1	3
Number of O Atoms	1	1	3
Number of Methyl Groups	6	3	6
Vapor Pressure (25 °C)	42 Torr	16 Torr	10 Torr
H_0 (298K)*	-116.789 kcal/mol	-184.32 kcal/mol	---

Table 1.2 Experimental methods used to study the chemical kinetics of the compounds of interest in this study

Technique	Hexamethyldisiloxane HMDSO	Trimethylsilanol TMSO	Hexamethylcyclotrisiloxane HMCTSO
RCF IG Delay study (100 PPM in φ=0.1 syngas+air)	✖	✖	
DFST pyrolysis study Laser Schlieren	✖	✖	✖
DFST pyrolysis study TOF-MS (EI)	✖	✖	✖
HRRST pyrolysis study TOF-MS (ALS)	✖	✖	✖

2. Biogas Applications

As siloxane compounds are becoming more common in everyday products and processes, they are being introduced into waste-streams. This then leads to siloxanes being found in biogas recovered from landfills and waste water treatment facilities. Biogas is an attractive option as a second generation biofuel as the methane in biogas is a potent greenhouse gas. Fossil fuels have long been the global standard as the primary energy carriers due to their high energy densities, relative ease of production, and established infrastructure. However, combustion of fossil fuels results in the release of harmful emissions which have been shown to cause health problems and contribute to climate change. Significant advances in combustion strategies have been made which enable cleaner combustion and increased fuel economy. These gains have helped reduce the pollutants per kilowatt-hour of energy generated, but increasing energy demands over time have overshadowed these impacts and further developments are necessary. Landfill gas is of particular interest due to its high methane content which is a much more potent greenhouse gas than CO_2 (where CH_4 is approximately 30 times more effective as a greenhouse gas compared with CO_2 [2]). As of 2016, less than a quarter of U.S. landfills were capturing the released biogas[2]. Extensive studies have been conducted on the impact of common impurities found in coal-derived syngas, but much less in known on the impact of impurities from biomass-derived syngas (also known as biogas) especially regarding organic silicon compounds.

Trace concentrations of siloxanes have become a problem in biogas combustion applications as oxidation of silicon leads to the formation of abrasive silica particles which can deposit on engine components, heat exchangers, etc. For this reason, most prior research in this area has focused on identifying and quantifying the siloxanes in biogas and on their removal from the captured gas. Rasi et al. [3] conducted a study to identify the organic silicon compounds found in

gases from landfills, wastewater treatment plants and biogas plants. The most common compounds in gas derived from landfills were octamethylcyclotetrasiloxane (D4), hexamethyldisiloxane (L2 or HMDSO) and trimethyl silanol (TMSO) [3]. Dewil et al. [4] conducted a review of the fundamentals of siloxanes and the current problems they pose in the context of biogas as a fuel, which mainly focus on the damage caused by the production of abrasive microcrystalline silica when silicon containing gases were combusted [4]. While the previous work has explored the impact of silicon-containing compounds on engine operation, very little work has explored the impact these compounds have on ignition and combustion. The objective of this work was to quantify the effects of siloxane on the reaction chemistry relevant to combustion systems including oxidation and thermal decomposition reactions.

The most relevant previous study of siloxane combustion in biogas was conducted by Mansfield et al. [5], where the effects of trace amounts of TMSO were studied in auto-ignition experiments of syngas at 5 and 15 atm. The work showed notable impact from the addition of TMSO as well as experimentally demonstrating the occurrence of two stage ignition at higher pressures. Concentrations of 10 ppm and 100 ppm TMSO were tested at 5 and 15 atm for a range of temperatures from ~1010-1110 K. For both concentration levels, TMSO decreased auto-ignition delay times. While the work by Mansfield et al. [5] quantified the effects of trace amounts of TMSO on decreasing ignition delay times, the manner in which TMSO acts on the syngas combustion and how that could be extrapolated to other organosilicon compounds was not considered in the study. A key observation by Mansfield et al. [5] was the effects of TMSO on a syngas mixture were similar to the effects of SiH_4 on ignition of pure H_2 as observed in various SiH_4 studies (e.g., [6,7]) which indicates similar chemical kinetic causes may be the source of the behavior observed for a large range of silicon-based species. An improved

understanding of the fundamental reaction kinetics of these complex fuel interactions will provide a foundation for determining if advanced combustion strategies can leverage the energy content of siloxanes while mitigating the negative effects associated with these compounds.

3. Siloxane Chemistry

While gas-phase silicon chemistry is critical to many materials applications as well as energy systems, development of reaction kinetics has been limited, as empirical approaches and methods based on simple analogy to hydrocarbon compounds have been considered sufficient to date. For example, much of the early work known for gas phase silicon compounds focused on developing reaction kinetics and thermochemistry from analogies to similar carbon structures [6,8]. However, more recent work demonstrates empiricism and analogy are limiting advances in some material synthesis and combustion systems [9,10,11,12]. The processes where pyrolysis and oxidation of silanes and siloxanes are important span a broad range of conditions, temperatures in the range of 600 – 2000 K and pressures of 1 to 20 bar, which adds challenges to developing fundamental reaction chemistry that is accurate for the range of relevant state conditions.

To date most studies involving the combustion of silicon-based species have focused on compounds and conditions relevant to chemical vapor deposition of silicon films and accelerants like silane (SiH_4) [13,14,15,16,17]. A detailed mechanism for SiH_4 combustion was developed by Miller et al [18] including estimates for the $SiH_3 + O_2$ reaction, but the authors noted the need to revisit existing silicon thermochemistry. Feroughi et al. [9] subsequently used portions of the detailed reaction mechanism from Miller et al. [18] in their study of the synthesis of silicon dioxide nanoparticles in a hydrogen/oxygen laminar premixed flame seeded with small amounts of HMDSO. A global reaction for HMDSO + OH was proposed, but fully detailed reaction kinetics were identified as a source of uncertainty and possible discrepancy between the model

predictions and the experimental observations. The work of Miller et al. and Feroughi et al. heavily built upon the pioneering work by Chagger et al looking at the formation of SiO_2 from the combustion of HMDSO in methane-air flames [19]. A model for the production of SiO_2 from HMDSO was proposed in Chagger et al. [19], but mainly focused on the production of SiO and conversion of SiO into SiO_2. The initiating reactions involving HMDSO were not considered in detail due to the lack of thermochemical data.

Further prior work includes Cherneshev et al. who studied low temperature pyrolysis of HMDSO as a source of silanones and proposed reaction schemes which included the production of small organic species, such as CH_3, as well as growth to larger siloxanes [20]. Almond et al. examined low pressure pyrolysis of linear [21] and cyclic siloxanes [22] including HMCTSO at 1000 K. CH_3, CH_4, C_2H_2, C_2H_4, C_2H_6 and SiO were identified as significant pyrolysis products. While this appears to support mechanisms proposed as portions of the oxidation pathways, Almond et al. also noted these species may be produced through pathways that involve highly reactive intermediates, such as dimethylsilanone ($(CH_3)_2SiO$) and 2-silas butane ((CH_3SiCH_2)), and perhaps not by direct decomposition to the base organic radicals and SiO.

While the prior studies capture some of the characteristics of SiO and SiO_2 production, the reaction pathways are still relatively unknown. The three compounds explored in the study were chosen due to their complimentary structures which allow for an interrogation of the influence of the physical structure and chemical composition. The compounds represent various silicon to oxygen ratios (2:1 for HMDSO, 1:1 for TMSO and HMCTSO), methyl group content, and structural symmetries. These structures also represent the building blocks for larger compounds lending to the development of a foundation for class rules. Each experimental technique provides unique experimental data to provide further understanding of the gas-phase chemistry of these

compounds. The auto-ignition study provides valuable insight into the fuel interactions relevant for landfill gas applications isolated from complex flame behaviors and fundamental gas-phase chemistry of each compound can be isolated in the pyrolysis experiments. Identifying intermediates provides valuable information on the pathways important in these combustion systems and helps with the development and validation of detailed thermochemistry and reaction kinetics.

4. Citations

[1] A. Teleki, B. Buesser, M.C. Heine, F. Krumeich, M.K. Akhtar, S.E. Pratsinis, Ind. Eng. Chem. Res. 48 (2008) 85-92.

[2] Murray, B. C., Galik, C. S., Vegh, T., "Biogas in the United States. An Assessment of Market Potential in a Carbon-Constrained Future," Nicholas Institute Report, NI R 14-02, 2014.

[3] S. Rasi, J. Lehtinen, and J. Rintala, Determination of organic silicon compounds in biogas from wastewater treatments plants, landfills, and co-digestion plants, Renew. Energy 35 (2010) 2666–2673.

[4] R. Dewil, L. Appels, and J. Baeyens, Energy use of biogas hampered by the presence of siloxanes, Energy Convers. Manag. 47 (2006) 1711–1722

[5] A. B. Mansfield and M. S. Wooldridge, The effect of impurities on syngas combustion, Combust. Flame 162 (2015) 2286–2295.

[6] Jachimowski, C. J., McLain, A. G. A. (1983) Chemical Kinetic Mechanism for the Ignition of Silane/Hydrogen Mixtures, NASA Technical Report TP 2129.

[7] E.L. Petersen, D.M. Kalitan, M.J.A. Rickard, *J. Propuls. Power* 20 (2004) 665-674.

[8] Britten, J. A., Tong, J., Westbrook, C. K. (1990) "A numerical study of silane combustion," Proc. Combust. Inst. 23:195-202.

[9] O. M. Feroughi, L. Deng, S. Kluge, T. Dreier, H. Wiggers, I. Wlokas, and C. Schlulz, Experimental and numerical study of a HMDSO-seeded premixed laminar low-pressure flame for SiO2 nanoparticle synthesis, Proc. Combust. Inst. 36 (2017) 1045–1053.

[10] R. S. M. Chrystie, H. Janbazi, T. Dreier, H. Wiggers, I. Wlokas, and C. Schulz, Comparative study of flame-based SiO 2 nanoparticle synthesis from TMS and HMDSO: SiO-LIF concentration measurement and detailed simulation, Proc. Combust. Inst. 37 (2019) 1221–1229.

[11] Jalali, A., Motamedhashemi, M. M. Y., Egolfopoulos, F., Tsotsis, T. (2013) "Fate of siloxane impurities during the combustion of renewable natural gas," *Comb. Sci. Tech.* 185:953-974.

[12] Nair, N., Vas, A., Zhu, T., Sun, W., Gutierrez, J., Chen, J., Egolfopoulos, F., Tsotsis, T. T. (2013) "Effect of siloxanes contained in natural gas on the operation of a residential furnace," *Ind. Eng. Chem. Res.* 52:6253−6261.

[13] Allendorf, M. D., Osterheld, T. H. (1995) "Modeling the gas-phase chemistry of silicon carbide formation," *Materials Research Society Symposium - Proceedings* 363:39-44, Chemical Vapor Deposition of Refractory Metals and Ceramics III.

[14] Allendorf, M. D., Melius, C. F., Ho, P., Zachariah, M. R. (1995) "Theoretical study of the thermochemistry of molecules in the Si-O-H system," *J. Phys. Chem.* 99:15285–15293.

[15] Zachariah, M. R., Tsang , W. (1995) "Theoretical calculation of thermochemistry, energetics, and kinetics of high-temperature $Si_xH_yO_z$ reactions," *J. Phys. Chem. A* 99:5308–5318.

[16] Suh, S.-M., Zachariah, M. R., Girshick, S. L. (2002) "Numerical modeling of silicon oxide particle formation and transport in a one-dimensional low-pressure chemical vapor deposition reactor," *Aerosol Science* 33:943–959.

[17] Babushok, V. I., Tsang, W., Burgess, Jr., D. R., Zachariah, M. R. (1998) "Numerical study of low and high-temperature silane combustion," *Proc. Combust. Inst.* 27:2431–2439.

[18] Miller, T. A., Wooldridge, M. S., Bozzelli, J. W. (2004) "Computational modeling of the $SiH_3 + O_2$ reaction and silane combustion," *Combust. Flame* 137:73-92.

[19] Chagger, H. K., Hainsworth, D., Patterson, P. M., Pourkashanian, M., Williams, A. (1996) "The formation of SiO_2 from hexamethyldisiloxane combustion in counterflow methane-air flames," *Proc. Combust. Inst.* 26:1859-1865.

[20] Chernyshev, E. A., Krasnova, T. L., Sergeev, A. P., Abramova, E. S. (1997) "Siloxanes as sources of silanones," *Russian Chem. Bull*. 46:1586-1589.

[21] Almond, M. J., Becerra, R., Bowes, S.J., Cannady, J.P, Ogeden, J.S., Young, N.A., Walsh, R., A mechanistic study of the low pressure pyrolysis of linear siloxanes, *Phys. Chem. Chem. Phys.* 11 (2009) 9259–9267.

[22] Almond, M. J., Becerra, R., Bowes, S.J., Cannady, J.P, Ogeden, J.S., Walsh, R. A mechanistic study of cyclic siloxane pyrolyses at low pressures, *Phys. Chem. Chem. Phys.* 10 (2008) 6856-6861.

Chapter 2: Effects of Organosilicon Compounds on Syngas Auto-ignition Behavior

*Portions of this chapter appear in the paper Schwind, R.A. and Wooldridge, M.S, "Effects of Organic Silicon Compounds on Syngas Auto-ignition Behavior" *Combustion and Flame*, in press 2019, as well as the conference paper Schwind, R.A., Sivaramakrishnan, R., Wooldridge, M.S., Understanding siloxane combustion chemistry: computation and experimental studies of hexamethyldislioxane, *11th U.S. National Combustion Meeting*, Pasadena, CA. March 2019.

1. Introduction

Interest in syngas combustion applications has been growing as energy technologies move from fossil fuels to rely more on sustainable and renewable fuels. In particular, syngas derived from second generation feed stocks such as landfill gas and sewage gas is an important pathway to mitigate environmental impacts of landfills and wastewater treatment plants while simultaneously displacing fossil fuels. Currently landfill gas is under-utilized with less than a quarter of landfills reporting capture of the methane rich gas emissions as of 2016 [1].

The different sources for syngas production are introducing compounds that have not previously been present into biogas and syngas mixtures, like siloxanes. Siloxanes have become increasingly prevalent in industrial products and processes (e.g. shampoos, creams, food production, oil, etc.) and are making their way into landfills and wastewater and thus into the landfill gas emissions and biogas produced from landfills and sewage gas [2], [3]. Siloxanes present even at low concentrations in syngas can have dramatic impact on combustion applications, for example the nanoparticulate SiO_2 formed as a product of combustion can lead to significant fouling of surfaces found in heat exchangers and other appliances [3], [4] and can cause abrasive damage in reciprocating engines [2], [5], [6].

The most common organic silicon compounds found in gas derived from landfills are octamethylcyclotetrasiloxane (OMCTSO), hexamethyldisiloxane (HMDSO), and trimethylsilanol (TMSO) [2], [7]. Little is known about the combustion chemistry of these organic silicon compounds. The only combustion studies to date of TMSO are by Mansfield and Wooldridge [8] and of HMDSO by Feroughi et al. [9] and Chrystie et al. [10]. Mansfield and Wooldridge [8] conducted experimental studies of auto-ignition of syngas mixtures of H_2 and CO including the impact of trace amounts (10 ppm and 100 ppm, mole basis) of TMSO at 5 and 15 atm for a range of temperatures from ~1010-1110 K. The results showed notable impact from the addition of TMSO where the reactivity of the mixtures increased dramatically. The TMSO also affected the pressure dependence of the H_2 and CO mixtures. While Mansfield and Wooldridge [8] conjectured on the reaction pathways of TMSO leading to the observed behavior, the detailed kinetics were not identified. Feroughi et al. [9] studied synthesis of silicon dioxide nanoparticles in a hydrogen/oxygen laminar premixed flame seeded with small amounts (200 ppm) of HMDSO. A global reaction for HMDSO + OH was proposed and integrated into a detailed reaction mechanism for silane (SiH_4), but the approximation of the global reaction was identified as a source of uncertainty and possible discrepancy between the model predictions and the experimental observations. In a similar study, Chrystie et al [10] proposed a model for the decomposition of HMDSO to SiO and SiO_2. While the model proposed matched the SiO and SiO_2 experimental data reported, it does not capture the initial reaction kinetics.

The objective of the current study was to provide new qualitative and quantitative understanding of the combustion chemistry of siloxanes in order to better anticipate and control their effects on combustion applications. The new experimental data on HMDSO ignition were compared with results on TMSO ignition to understand the effects of siloxane chemical

structure. The technical approach used auto-ignition experiments to explore the effects of trace amounts of different siloxane compounds on the auto-ignition behavior of syngas (H_2 and CO) mixtures. Both existing ignition data on TMSO and new data were used for the comparison with HMDSO.

The chemical structures of TMSO and HMDSO are presented in Figure 2.1. Both compounds are directly relevant to biogas with siloxane impurities and comparison of the two species also emphasizes the effect of doubling the $Si(CH_3)_3$ structural contribution to the combustion chemistry. The results are interpreted in the context of possible reaction pathways leading to the observed ignition behaviors.

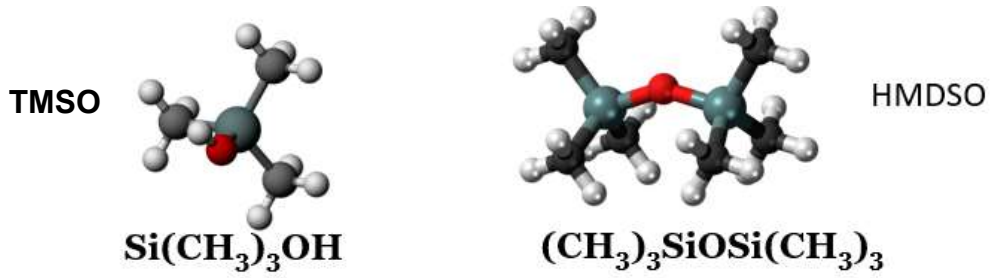

Figure 2.1: Molecular structures of siloxanes studied in the current work: trimethylsilanol (TMSO) and hexamethyldisiloxane (HMDSO)

While the exact mechanism for the effects remains unknown, the hypothesis of this work is that two potential mechanisms could lead to the observed ignition promoting characteristics of HMDSO. One potential mechanism could be akin to that of cetane enhancers used to promote ignition in diesel fuels. Such molecules typically have low bond strengths and rapidly dissociate to radicals that then propagate chain-branching oxidation. This was initially explored through seeding computational simulations with radicals (e.g., OH, CH_3, etc.) that would result from instantaneous decomposition of the parent molecules. In order to test this hypothesis, *ab initio* electronic structure calculations were used to characterize the energetics for the various

molecular and bond fission channels in HMDSO. The theoretical calculations were also used to determine heats of formation and thermochemical functions for relevant minima on the HMDSO potential energy surface. An alternate mechanism could involve the potential role of negative-temperature-coefficient (NTC) type chemistry induced by R + O_2 reactions of HMDSO that could be responsible for ignition promotion in syngas. Preliminary theoretical calculations for first and second O_2 addition to the HMDSO radical were also performed to probe this mechanistic possibility.

2. Methods

2.1 Rapid Compression Facility Experiments

The ignition behavior was studied utilizing the University of Michigan rapid compression facility (RCF). Three fuel mixtures were used: (1) H_2 and CO with a molar ratio of CO:H_2 = 2.34:1, (2) the same base mixture of H_2 and CO with 0.25% HMDSO (mole fraction basis of the total fuel), and (3) the base mixture of H_2 and CO with 0.25% TMSO (mole fraction basis of the total fuel). Each mixture had a fuel-to-oxidizer equivalence ratio of $\varphi = 0.1$ and was "air"-dilute with molar oxygen (O_2)-to-inert gas ratio of 1:3.76. The inert gases were mixtures of nitrogen (N_2) and argon (Ar) to achieve the desired test conditions. Table A1 of the appendix summarizes the mixture compositions, state conditions and ignition delay time results of the study. The base mixture was chosen due to the demonstrated strong, homogeneous ignition behavior (where strong ignition was defined as per Mansfield and Wooldridge [11]). Strong homogeneous ignition behavior is vital to chemical kinetics studies. Additionally, the base mixture of H_2 and CO exhibited two distinct stages of ignition in the temperature and pressure region of interest. The trace amounts of siloxanes used in the study are much higher than what has been found in landfill gas and other biogas sources. However, the higher siloxane concentrations allow more

observables to be detected and thereby provide higher confidence in the results and understanding of siloxane chemical kinetics. Additionally, the 100 ppm levels of HMDSO and TMSO used in the current work are still sufficiently small that the siloxane chemistry is dominated by the interactions with syngas and air and not self-reaction. So, in that respect, the chemistry is expected to be directly relevant to lower siloxane concentrations found in biogas.

The mixtures were made in a dedicated stainless-steel mixing tank and the compositions were determined by using the partial pressures of the constituents as measured using a capacitance manometer gage (MKS Baratron Model 690A13TRB). The amounts of HMDSO and TMSO were calculated to yield mole fractions of 100 ppm of the organic silicon species relative to the total gas mixture. The gases used for the mixtures were ultra-high purity (99.993%) O_2, ultra-high purity argon, ultra-high purity N_2, pre-purified grade H_2 and ultra-high purity (99.9%) CO, all obtained from Purity Plus. The TMSO and HMDSO were from Sigma Aldrich with purities of ≥97.5% for the TMSO (CAS Number 1066-40-6) and ≥98.5% for the HMDSO (CAS Number 107-46-0). Each mixture was stirred continuously for at least one hour prior to the ignition experiments.

Ignition experiments were performed using the RCF to produce pressures of approximately 9 to 10 atm with a temperature range of 1010 K to 1070 K. A thorough description of the device and studies characterizing the RCF performance are detailed in He et al. [12] and Donovan et al. [13]. A brief description is provided here. The RCF consists of three sections: the driver section and the driven section, which are separated by a fast actuating globe valve, and a test section which is connected to the open end of the driven section. A free piston is installed at the upstream end of the driven section and in front of the globe valve, to drive the rapid compression of test gas mixture.

Prior to compression, the test volume is evacuated with a pump and filled with the desired test gas mixture. The driver section is then pressurized and the globe valve is opened. The pressure launches the free piston down the length of the driven section, rapidly compressing the test gas into the test section volume which is ~50 mm long with a 50 mm diameter cross-section. The cross-section of the driven section decreases before the test section (via a convergent section) so the nose cone of the free piston achieves an annular interference fit to seal the test section. At the end of compression, the test section is filled with a uniform mixture which has been isentropically compressed to the desired state conditions, i.e. the targeted end-of-compression pressure and temperature. The test section is instrumented with a piezoelectric pressure transducer (6125B Kistler, Amherst, NY) and charge amplifier (5010 Kistler, Amherst, NY) to collect pressure data. The transducer is rated to an uncertainty of ≤1% of total range (100 Torr, 1000 Torr) and data are collected at 100 kHz sampling frequency. The test section also has a polycarbonate endwall to provide optical access for high-speed imaging which is used to confirm homogeneous ignition behavior. A digital camera (V711-8G-MAG-C Phantom by Vision Research) with a Navitar 50 mm lens (F0.95), a Hoya 62 mm lens (2x zoom), and a Hoya 62 mm UV(0) filter is used to record the high-speed image sequences at 25,000 frames per second with the CMOS array with a resolution of 512x512 pixels and an exposure time of 39.3 μs.

2.2 Theoretical Calculations for HMDSO

In collaboration with researchers at Argonne National Laboratory, the rovibrational properties of the minima and transition states (the molecular channels only) for the relevant thermal decomposition steps in HMDSO were determined at the M06-2X/cc-pvtz level of theory. Higher level energy estimates for the stationary points were obtained using the CCSD(T)/cc-

pV∞Z method, where the infinite basis set limits are estimated from an extrapolation of results obtained from sequences of cc-pVnZ where n = (D,T,Q) basis sets[14,15]. More specifically for the CCSD(T)/cc-pV∞Z method, the results use a CCSD(T)/cc-pVnZ n=(D,T) extrapolation, and two sets of MP2/cc-pVnZ n=(D,T) and n=(T,Q) extrapolations to converge at the CCSD(T)/cc-pV∞Z limit [15]. The Gaussian 09 [16] software package was used to perform the electronic structure calculations [17]. The results of the molecular orbital studies were used to interpret the experimental results presented here.

3. Results

3.1 Experimental Results

Typical pressure measurements from the ignition experiments of the different fuel mixtures are presented in Figure 2.2. The compression stroke continuously and smoothly increases the pressure in the test section from the start of the experiment until the nosecone seats, ending compression. There is then a slight decrease in pressure after the end of compression (EOC) due to heat transfer from the test gas volume to the test section walls which is then followed by a rapid increase in pressure during the ignition event. The EOC was set as time t= 0 for each experiment. The pressure data was processed through an 80-point span moving average smoothing algorithm before assigning the ignition delay time. The ignition delay time was determined from each experiment using the pressure time-history data and the corresponding dP/dt data which were calculated using a central differencing algorithm. As shown in Figure 2.2, the ignition delay time was defined as the time from the EOC to the time of the maximum of the pressure time derivative. For experiments where two stage ignition was observed, the time of the first stage of ignition was defined as the time from EOC to the time of the first local dP/dt maximum, and the time of the second stage of ignition was determined as the time from EOC to

the time of the second local dP/dt maximum. When reporting the overall ignition delay, the second maximum was used for conditions where two stage ignition was observed. Uncertainty in the ignition delay time measurements primarily results from the smoothing algorithm and the bounds were defined independently for each experiment by varying the smoothing algorithm span by ±25%. Additional uncertainty was defined for each experiment by considering the range for reasonable assignment of the dP/dt maxima. The resulting uncertainty for τ_{ign} was approximately ±5%.

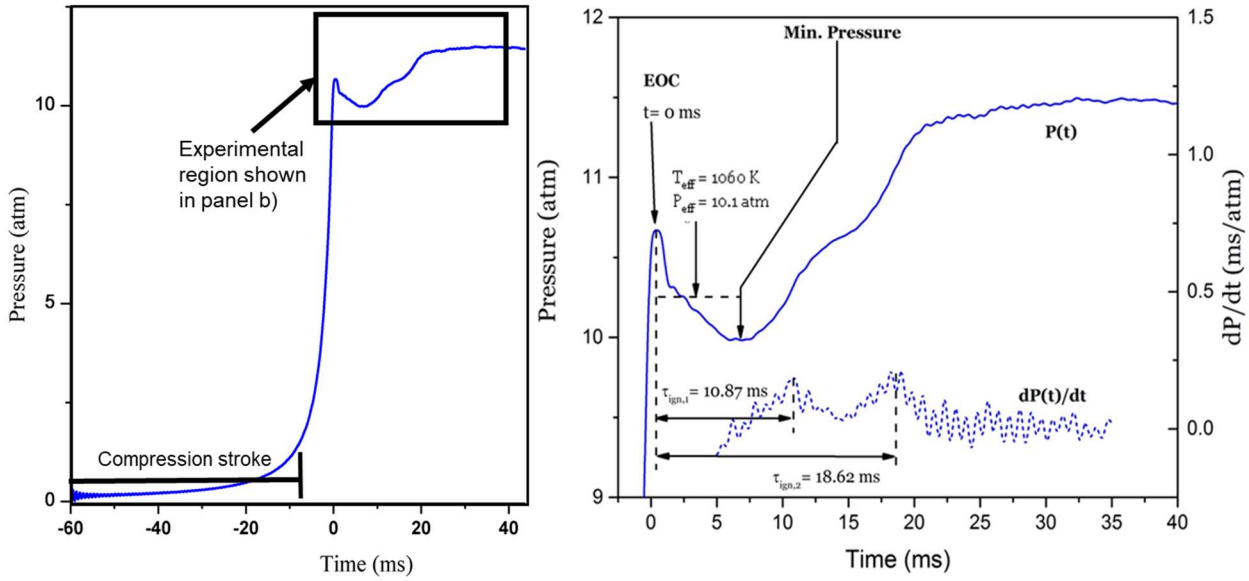

Figure 2.2: Typical results for pressure time history and pressure derivative for the experimental conditions of P = 10.1 atm, T = 1060 K, for a base mixture of H2 and CO with no siloxane. τign,1 and τign,2 are the first and second stage ignition delay time

For each experiment, a thermodynamic state was assigned using the following process. The pressure was measured directly and the temperature within the test section was calculated using isentropic compression relations and the properties of the test gas mixture. Donovan et al. [13] experimentally verified an isentropic compression process well represents the initial compression stroke of the core region of the gases in the test section of the RCF. The uncertainty in the

calculated temperature is ≤ 0.4% and is due to the uncertainty in the pressure measurement. In order to account for the small decrease in pressure and temperature between the EOC and the minimum pressure before ignition, P_{min}, an effective temperature and pressure state were assigned by taking the arithmetic mean of the pressure measured from EOC to P_{min} and then calculating the temperature assuming an isentropic expansion from the EOC state to the effective pressure. Assigning effective temperature and pressure in this manner has been applied in previous experiments using the UM-RCF for similar fuels [11], [18] and other ignition studies [12], [19]. The assignment of an effective thermodynamic state allows for incorporation of the heat transfer effects while maintaining clarity in reporting and was discussed in detail by Mansfield and Wooldridge [11].

High-speed imaging was used to confirm the homogeneity of the ignition at the test conditions studied. Figure 2.3 shows a typical image of the chemiluminescence resulting from ignition of a fuel mixture of H_2 and CO, specifically corresponding to the experimental results presented in Figure 2.2. The uniformity seen throughout the image illustrates that the data collected represent the behavior of the entire reactive core and not a local region or non-spatially uniform event. In other words, homogeneous or strong auto-ignition dominated the conditions studied.

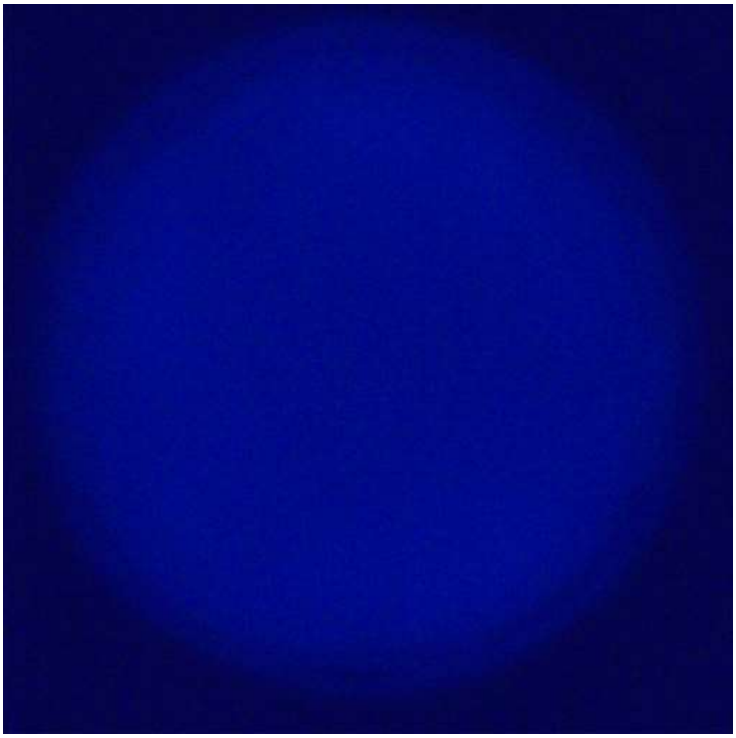

Figure 2.3: The image shows homogeneous chemiluminescence within the reactive core of the test section resulting from ignition of a mixture of H_2 and CO at P=10.1 atm, T=1060 K, φ=0.1.

The experiments in the study had pressures in the range of 8.7-10.25 atm with corresponding temperatures in the range of 1010-1070 K. A summary of the results for the auto-ignition delay times is presented in the Arrhenius diagram in Figure 2.4. A list of the results is also presented in the appendix in Table A1. The results show a dramatic increase in reactivity and thus decrease in ignition delay time due to the addition of HMDSO and TMSO in comparison with the baseline mixtures of H_2 and CO.

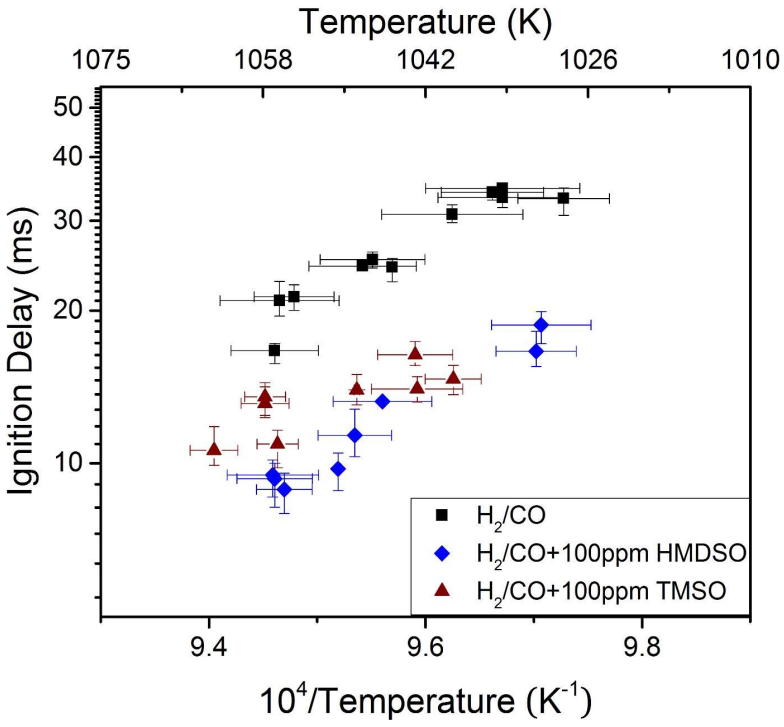

Figure 2.4: Experimental results for ignition delay times for P = 8.7-10.25 atm. The error bars represent the uncertainties in the ignition delay time measurements and the assigned temperatures. See text for details.

The addition of both HMDSO and TMSO promoted ignition by reducing the ignition delay time. The addition of HMDSO reduced the baseline H_2 and CO mixture ignition delay time by approximately 50%, while TMSO reduced the H_2 and CO mixture ignition delay time by approximately 37% when compared at similar state conditions. In addition to reducing ignition delay time, the 100 ppm of siloxanes also increased the pressure rise and pressure rise rate considerably, as seen in Figure 2.5, which presents pressure time histories and pressure time derivatives for three experiments at comparable state conditions with the different fuel mixtures.

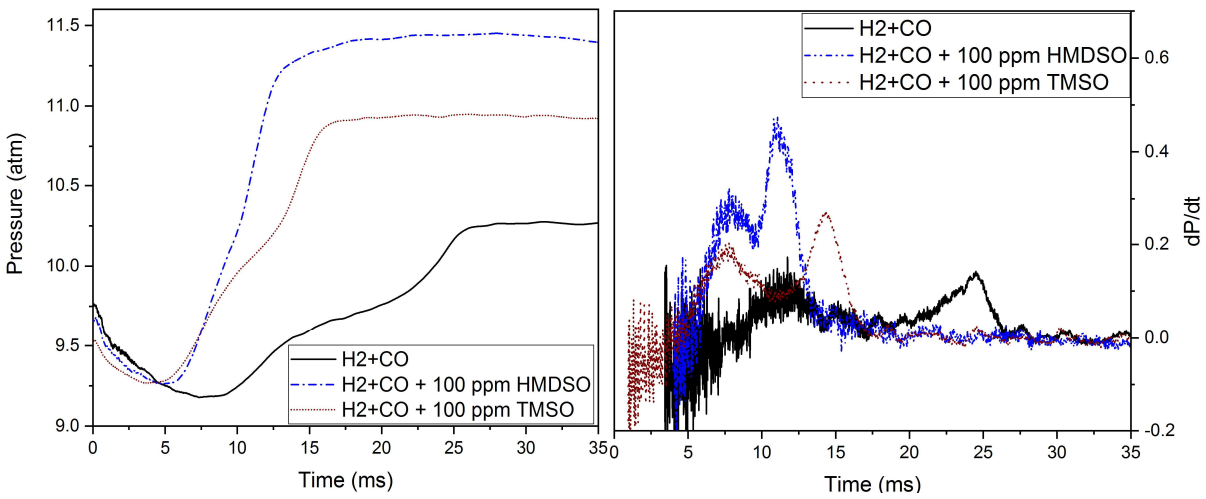

Figure 2.5: Pressure time histories and corresponding dP/dt data for experiments with comparable state conditions: H_2+CO with P = 9.4 atm and T=1045 K, H_2+CO+100 ppm HMDSO with P = 9.4 atm and T = 1050 K, and H2+CO+100 ppm TMSO with P = 9.4 atm and T = 1040 K.

3.2 Theoretical Calculation Results

Table 2.1 and Figure 2.6 below summarizes the energy results from the molecular orbital calculations [20].

Table 2.1: Stationary point energies for the thermal decomposition reactions of HMDSO.[a]

Saddle Point	CC//M06[b]
HMDSO → Trimethylsilanol + $Si{=}CH_2(CH_3)_2$ (TS)	75.67
HMDSO → Tetramethylsilane + $(CH_3)_2Si{=}O$ (TS)	81.98
Trimethylsilanol+ $Si{=}CH_2(CH_3)_2$	81.35
Tetramethylsilane + $(CH3)_2Si{=}O$	70.65
$CH_2(CH_3)_2SiOSi(CH_3)_3$ + H	100.29
$(CH_3)_3SiO$ + $(CH_3)_3Si$	139.09
CH_3 + $(CH_3)_2SiOSi(CH_3)_3$	93.08

[a] Values are in kcal/mol and include zero-point corrections at 0 K. These values are relative to the reactant, HMDSO. The rows incorporating reactions and marked by TS refer to barrier heights and the rows incorporating products refer to reaction exo- or endo-thermicities.

[b] Present CCSD(T)/cc-pV∞Z//M06-2X/cc-pvtz calculations.

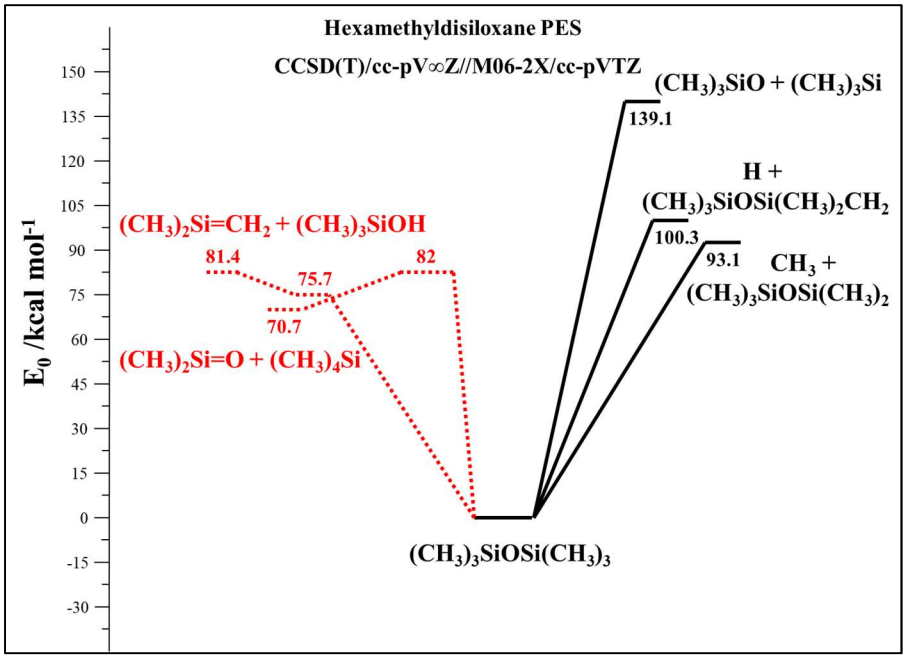

Figure 2.6: Potential energy surface for the decomposition of HMDSO [Provided by Dr. Raghu Sivaramakrishnan]

The energy values indicate two molecular channels are active and have energies below the lowest energetically accessible bond fission channel (CH_3 loss). However, the two molecular processes also have barriers above 75 kcal/mol effectively ruling out significant decomposition at temperatures relevant to the syngas autoignition studies discussed in this study. Interestingly, the saddle point for the lowest energy channel is lower than the energy of the separated products, an observation similar to that noted in disilane dissociation [21]. Consequently, a proper treatment of the kinetics of these processes should utilize the two-transition state theory approach detailed in [21].

The theoretical predictions indicate the first mechanism involving rapid dissociation of HMDSO cannot be active in promoting syngas ignition. Therefore, theoretical studies have also been initiated to probe the energetics of the $CH_2(CH_3)_2SiOSi(CH_3)_3 + O_2$ reaction. Preliminary results at the CCSD(T)/aug-cc-pvdz//M06-2X/cc-pvtz level of theory indicate barriers for two H-

atom transfers from RO_2 species to form two distinct QOOH species are below the R + O_2 entrance channel as illustrated by the potential energy surface shown in Figure 2.7.

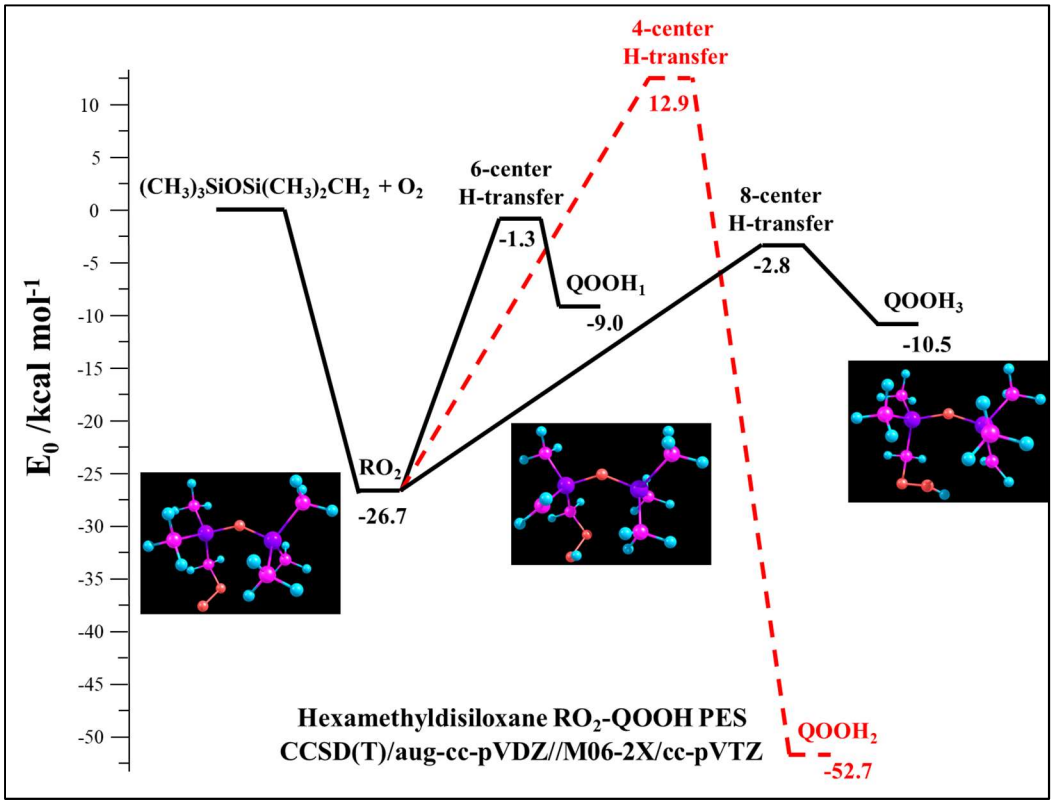

Figure 2.7: Potential energy surface for the subsequent RO_2 to QOOH propagations as outlined below. [Provided by Dr. Raghu Sivaramakrishnan]

The results indicate a potential competition between chain branching and chain propagating chemistry similar to the hydrocarbon reaction pathways that are attribute to negative temperature coefficient (NTC) behavior observed with some hydrocarborn fuels. Ongoing studies are in progress to calculate energetics for all the relevant channels from the R + O_2 and the corresponding QOOH + O_2 reactions of HMDSO. The energetically accessible channels are outlined in Figure 2.8 and Table 2.2.

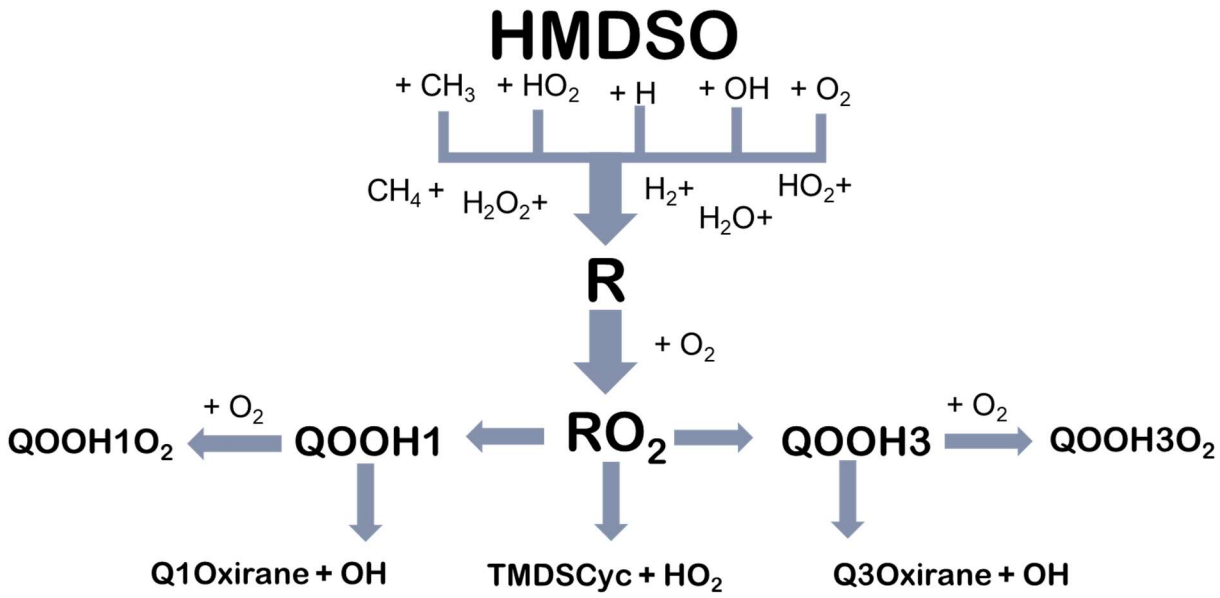

Figure 2.8: Hexamethyldisiloxane oxidation pathways. Here "R" represents the intermediate radical that is formed by any H abstraction process. Structures and formulas of the intermediate species are provided in Table 2.2.

Table 2.2: Formulas and structures for species of interest in the

	Formula	Structure
HMDSO	$(CH_3)_3SiOSi(CH_3)_3$	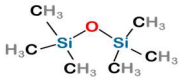
R	$CH_2(CH_3)_2SiOSi(CH_3)_3$	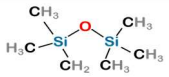
RO_2	$OOCH_2(CH_3)_2SiOSi(CH_3)_3$	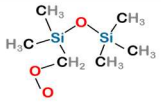
QOOH1	$HOO(CH_2)_2CH_3SiOSi(CH_3)_3$	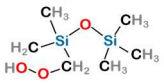
QOOH3	$HOOCH_2(CH_3)_2SiOSi(CH_3)_2CH_2$	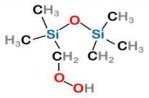
TMDSCyc	$CH_2(CH_3)_2SiOSi(CH_3)_2CH_2$	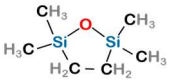
Q1Oxirane	$O(CH_2)_2CH_3SiOSi(CH_3)_3$	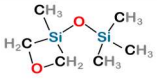
Q3Oxirane	$OCH_2(CH_3)_2SiOSi(CH_3)_2CH_2$	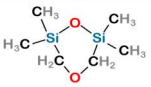
QOOH1O2	$H(O_2)_2(CH_2)_2CH_3SiOSi(CH_3)_3$	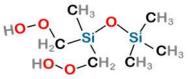
QOOH3O2	$HO_2CH_2(CH_3)_2SiOSi(CH_3)_2CH_2O_2$	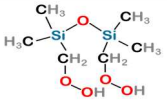

4. Discussion

For the mixture compositions and pressure and temperature range explored in this study, all auto-ignition experiments demonstrated two stage ignition behavior where two distinct dP/dt local maxima could be identified. Mansfield and Wooldridge [11] were the first to experimentally observe the distinct two stage ignition behavior of H_2 and CO mixtures.

Mansfield and Wooldridge used computational simulations to interrogate the H_2 and CO ignition behavior and attributed the two stages to differences in the characteristic reaction times (and the associated reaction chemistry) of H_2 and CO at the state and mixture conditions studied. Essentially, the hydrogen gas reacts more readily than the carbon monoxide creating two distinct stages of heat release and pressure rise. Furthermore, model simulations indicated the first stage of ignition was associated with formation of H_2O_2 and HO_2, while the second stage of ignition was associated with OH and O radical formation [22]. By using conditions that exhibit separate stages of ignition in the current work, the effects of TMSO and HMDSO on specific reaction pathways may be clearer.

Looking more closely at the pressure data in Figure 2.5, there is a noticeable difference between the behavior observed in the experiments with HMDSO, those with TMSO, and the baseline syngas fuel case. The dP/dt data show both the first and second stages of ignition are accelerated for the HMDSO and TMSO cases relative to the base fuel case. The rate of pressure rise of the mixtures with trace concentrations of HMDSO is higher than both the baseline syngas case and the mixture with trace concentrations of TMSO. Additionally, the HMDSO mixture ignites faster than the other mixtures. If NTC-type chemistry is not active for these mixtures, the increased energy release in the first stage (which leads to higher temperature) should accelerate the kinetics of the second stage. This is consistent with the experimental data presented in Figures 2.4 and 2.5, and the effects of acceleration are significant.

The impact on ignition delay time provides insights into the overall reaction rates of the different mixtures. The addition of 100 ppm of HMDSO had a more significant impact on reducing the ignition delay time, with over 10% more decrease in ignition delay time compared with the decrease caused by the addition of 100 ppm of TMSO. The complementary molecular

structures of HMDSO and TMSO provide points for comparison and differentiation. Both compounds contain organic functional groups with each HMDSO molecule containing six methyl groups and each TMSO molecule containing three methyl groups. The additional methyl content of HMDSO could account for the increased reactivity, but the impact of HMDSO on the ignition delay time of the base fuel is not double that of TMSO. This indicates the difference in the effects on ignition delay time is not proportional to number or concentration of methyl groups. TMSO contains a hydroxyl group in addition to the three methyl groups which could increase the reactivity beyond the methyl groups. The potential impact of the functional group concentrations on the elementary H_2 and CO ignition chemistry was explored through computational experiments which are discussed in detail in Chapter 4.

Another significant impact on the pressure time histories is the increased energy release illustrated by the increase in the final pressure after ignition. As seen in Figure 2.5, both HMDSO and TMSO increase the final pressure after ignition compared with the base H_2 and CO mixture. The addition of HMDSO shows a significant increase, with almost double the overall change in pressure (measuring from the minimum pressure after ignition to the maximum pressure) of the base fuel mixture and almost 1.5 times the pressure change resulting from the addition of TMSO. A larger energy contribution from the larger HMDSO molecule partially explains this behavior, but thermochemical data for the siloxanes is required to determine if the overall pressure increase is due to chemical equilibrium of the products or an additional outcome of changes in reaction pathways.

Due to the relatively low concentrations of siloxane added to the reactant mixtures, it is highly unlikely that the effects are entirely attributable only to the additional energy content from the trace species indicating that there are more complex interactions at play in the reaction

pathways. For example, since the main way for the compound to contribute energy to system is through breaking bonds, bond energy calculations were used to make coarse estimates of the energy content of the siloxanes. Since exact energies for these compounds are not available, these calculations were based upon using average bond dissociation energies for each specific bond in the molecule (for example, the average energy for a Si-O bond across multiple molecular configurations with values from [23]). This will not be as accurate as characteristic bond dissociation energies for each compound since the approach does not specifically account for the structures and interactions, and only provides a coarse estimate of the energy contribution. The results indicate a less than 3% increase in the total fuel energy with the addition of 0.25% of HMDSO and less than 2% increase with the addition of 0.25% of TMSO. Although the siloxanes may have relatively high energy densities, the low concentrations and air-dilute conditions result in minimal changes in the reactant mixture properties and energy. It is also valuable to note the P_{min} for the different mixtures was almost identical, indicating the HMDSO and TMSO did not affect the heat transfer and did not change the endo- or exo-thermicity before ignition compared with the H_2 and CO experiments - as would be expected due to the low concentrations. However, the significant increase in post ignition pressure may provide some insight into the thermal effects of the reactions activated by the addition of the HMDSO.

Further understanding of the reaction kinetics of the organic silicon compounds is needed before definitive conclusions can be drawn on what reaction pathways are impacted by the addition of the organic silicon species. Preliminary theoretical calculations provide some insight into what these pathways might be for HMDSO. While thermal decomposition routes are not accessible at the conditions of interest in this study, H abstraction is accessible and leads to exactly one radical due to the symmetry of the molecule. This indicates the increased reactivity

observed in these experiments is initiated by interactions with radicals resulting from the initial reactions of the base fuel. As noted previously, both the first and second stages of ignition are sensitive to the formation of HO_2, H_2O_2, OH and O radicals which could facilitate the initial H abstraction reaction. These routes have not been explored in prior HMDSO oxidation studies by Feroughi et al.[9] and Chrystie et al. [10] as their focus treated the HMDSO reaction pathways as independent from the combustion reactions of the base fuel. Based upon the calculations presented here, the two systems should not be handled independently and the interactions between the base fuel and HMDSO must be included.

The RO_2 to QOOH pathways that have been identified lead to at least two chain propagating pathways which each eject an OH radical while there is also a direct HO_2 ejection route from the RO_2 species serving as a third propagation route. For the experiments with trace concentrations of HMDSO, the pressure time histories show acceleration of both stages of ignition which could be supported by these propagation channels. The possible abstraction reactions, with the exception of HMDSO + OH = R + H_2O, show the production of the HMDSO radical plus either another radical or reactive species. This would provide a route for additional reactions beyond the chain propagation of the radical involved in the abstraction producing one radical through the RO_2 pathways and thus contribute to the increase in reactivity observed. However, it should be noted that this work is still on-going, and additional reaction pathways are still being considered. While the cyclic and oxirane species appear to be relatively stable, there still might be subsequent reactions resulting from the production of these species as well as further species production following the $QOOHO_2$ reaction pathways. The branching fractions and reaction rates are still unknown, but attempts to simulate the effects of the three identified propagation reactions are outlined in Chapter 4. Further understanding of the thermochemistry and reaction

kinetics of organic silicon compounds is necessary before these effects can be fully defined, but analysis of these initial reaction steps helps focus future work.

5. Conclusions

The data presented here provide new quantitative results on siloxane combustion of two important species: trimethylsilanol (TMSO) and hexamethyldisiloxane (HMDSO). Ignition experiments showed a dramatic increase in H_2 and CO reactivity due to the addition of the siloxanes HMDSO and TMSO. Significant increase in rate of pressure rise and final pressure were observed with the addition of the siloxane compounds. Thermophysical data and reaction chemistry are necessary to further understand the impact of siloxanes on combustion and ignition behaviors and to identify the reaction pathways affected by this important class of compounds.

6. Citations

[1] B. C. Murray, C. S. Galik, and T. Vegh, Biogas in the United States: estimating future production and learning from international experiences, *Mitig. Adapt. Strateg. Glob. Chang.* 22 (2017) 485–501.

[2] M. Schweigkofler and R. Niessner, Determination of siloxanes and VOC in landfill gas and sewage gas by canister sampling and GC-MS/AES analysis, *Environ. Sci. Technol*. 33 (1999) 3680–3685.

[3] S. Gersen, P. Visser, M. van Essen, M. Brown, A. Lewis, and H. Levinsky, Impact of silica deposition on the performance of gas-fired domestic appliances caused by the combustion of siloxanes in the fuel, *Renew. Energy* 132 (2019) 575–586.

[4] A. A. Turkin *et al.*, Deposition of SiO2nanoparticles in heat exchanger during combustion of biogas, *Appl. Energy* 113 (2014) 1141–1148.

[5] R. Dewil, L. Appels, and J. Baeyens, Energy use of biogas hampered by the presence of siloxanes, *Energy Convers. Manag.* 47 (2006) 1711–1722.

[6] M. Ajhar, M. Travesset, S. Yüce, and T. Melin, Siloxane removal from landfill and digester gas - A technology overview, *Bioresour. Technol*. 101 (2010) 2913–2923.

[7] S. Rasi, J. Lehtinen, and J. Rintala, Determination of organic silicon compounds in biogas from wastewater treatments plants, landfills, and co-digestion plants, *Renew. Energy* 35

(2010) 2666–2673.

[8] A. B. Mansfield and M. S. Wooldridge, The effect of impurities on syngas combustion, *Combust. Flame* 162 (2015) 2286–2295.

[9] O. M. Feroughi, L. Deng, S. Kluge, T. Dreier, H. Wiggers, I. Wlokas, and C. Schlulz, Experimental and numerical study of a HMDSO-seeded premixed laminar low-pressure flame for SiO2 nanoparticle synthesis, *Proc. Combust*. Inst. 36 (2017) 1045–1053.

[10] R. S. M. Chrystie, H. Janbazi, T. Dreier, H. Wiggers, I. Wlokas, and C. Schulz, Comparative study of flame-based SiO 2 nanoparticle synthesis from TMS and HMDSO: SiO-LIF concentration measurement and detailed simulation, *Proc. Combust*. Inst. 37 (2019) 1221–1229.

[11] A. B. Mansfield and M. S. Wooldridge, High-pressure low-temperature ignition behavior of syngas mixtures, *Combust. Flame* 161 (2014) 2242–2251..

[12] X. He, M.T. Donovan, B.T. Zigler, T.R. Palmer, S.M. Walton, M.S. Wooldridge, and A. Atreya, An experimental and modeling study of iso-octane ignition delay times under homogeneous charge compression ignition conditions, *Combust. Flame* 142 (2005) 266–275.

[13] M. T. Donovan, X. He, B. T. Zigler, T. R. Palmer, M. S. Wooldridge, and A. Atreya, Demonstration of a free-piston rapid compression facility for the study of high temperature combustion phenomena, *Combust. Flame* 137 (2004) 351–365.

[14] J. M. L. Martin, *Chem. Phys. Lett*. 259, (1996) 669-678.

[15] J. A. Miller, S. J. Klippenstein, *J. Phys. Chem. A* 107, (2003) 2680-2692.

[16] Gaussian 09, Revision A.02, Frisch, M. J.; Trucks, G. W.; Schlegel, H. B.; Scuseria, G. E.; Robb, M. A.; Cheeseman, J. R.; Scalmani, G.; Barone, V.; Mennucci, B.; Petersson, G. A. et al., Gaussian, Inc., Wallingford CT, 2009.

[17] Personal communication, Dr. Raghu Sivaramakrishnan (2019)

[18] S. M. Walton, X. He, B. T. Zigler, and M. S. Wooldridge, An experimental investigation of the ignition properties of hydrogen and carbon monoxide mixtures for syngas turbine applications, *Proc. Combust. Inst.* 31 (2007) 3147–3154.

[19] H. Di, X. He, P. Zharg, Z. Wang, M.S. Wooldridge, C.K. Law, C. Wang, S. Shuai, and J. Wang, Effects of buffer gas composition on low temperature ignition of iso-octane and n-heptane, *Combust. Flame* 161 (2014) 2531–2538.

[20] R.A. Schwind, R. Sivaramakrishnan, M.S. Wooldridge, Understanding siloxane combustion chemistry: computation and experimental studies of hexamethyldislioxane, *11th U.S. National Combustion Meeting*, Pasadena, CA. March 2019.

[21] E.W. Kaiser, T.J. Wallington, M. D. Hurley, J. Platz, H. J. Curran, W. J. Pitz, and C. K.

Westbrook, *J. Phys. Chem.* A 104, (2000) 8194-8206,

[22] A. B. Mansfield and M. S. Wooldridge, High-pressure low-temperature ignition behavior of syngas mixtures, *Combust. Flame* 161 (2014) 2242–2251.

[23] S.S. Zumdahl and S.A. Zumdahl, *Chemistry*, 5th ed, Houghton Mifflin College Division, 1990.

Chapter 3: Shocktube Pyrolysis of Organic Silicon Species

1. Introduction

While previous experiments have illustrated that the addition of silicon based impurities has notable impact on the auto-ignition behavior of the syngas systems, the reason for the impact is not fully understood. Based on this motivation, the project scope shifted to identify and quantify the thermal decomposition reaction pathways for key siloxane species. The aim was to use this research in order to better understand the gas phase thermochemistry of this novel class of compounds and predict potential reaction pathways for the oxidation kinetics. While interest in the reaction kinetics of siloxanes has been growing, a majority of studies have focused on the global production of the desired end product. Up until recently little research has been devoted to understanding the fundamental reaction kinetics of these species, especially in the gaseous phase. Combustion of these compounds has been studied in the context of the production of silicon based products, but most studies have focused on capturing the production of nano-particulate SiO_2 or tracking SiO production.

In this study, three different siloxane species which have been identified as concerns in biogas applications were studied: trimethylsilanol (TMSO), hexamethyldisiloxane (HMDSO), and hexamethylcyclotrisiloxane (HMCTSO). While there are no known pyrolysis studies for TMSO, HMDSO and HMCTSO pyrolysis has been studied. Cherneshev et al studied low temperature pyrolysis of HMDSO as a source of silanones in a hollow quartz reactor at 890-990

K and 1 atm with a 30 second residence time [1]. Figure 3.1 shows the reaction schemes for the thermal decomposition of HMDSO proposed by Chernyshev et al.

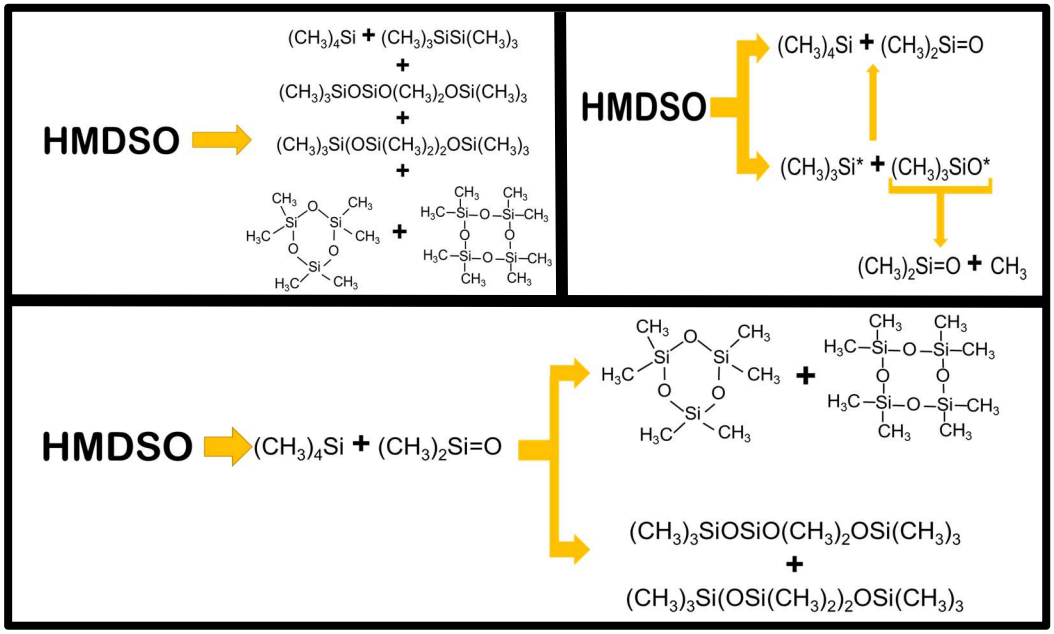

Figure 3.1: HMDSO thermal decomposition pathways proposed by Cherneshev based upon observations in their hollow quartz reactor study at 890-990 K and 1 atm with ~30 second dwell time [1].

Almond et al. looked at the low pressure pyrolysis of cyclic siloxanes [2] including HMCTSO at 1000 K. CH_3, CH_4, C_2H_2, C_2H_4, C_2H_6 and SiO were identified as significant pyrolysis products. These hollow quartz reactor studies occurred at much longer timescales than those relevant to combustion systems. In order to better analyze the thermal decomposition behavior of HMDSO, TMSO, and HMCTSO at combustion relevant timescales, shocktube pyrolysis experiments were carried out at Argonne National Laboratory (ANL). Access to the unique facilities at ANL, which are described in the methods section of this text, allowed for the collection of some first-of-their- kind experimental kinetic data for these compounds.

2. Methods

2.1 Shocktube Facilities

2.1.1 Diaphragmless Shocktube

Detailed descriptions and characterization of the ANL diaphragmless shocktube (DFST) can be found in Tranter and Giri [3] and Randazzo et al. [4]. A brief description is provided here. The ANL DFST consists of three primary parts: the driver section, the driven section and the fast actuating pneumatic valve which separates the two sections. The driver section is a stainless steel tube measuring 58 cm in length with a 22 cm inner diameter and the driver section houses the pneumatic valve. The fast-actuating pneumatic valve replaces the metal diaphragm found in a traditional shocktube. It seals the driver section from the driven section with an aluminum plate with a circumferential o-ring mounted on a stainless steel rod which is connected to a set of stainless steel bellows. The driven section is a stainless steel tube with a 6.35 cm inner diameter and has two lengths depending upon which diagnostic is being used, laser schlieren (LS) densitometry or time-of-flight mass spectrometry (TOF-MS). The effective length of the tube is changed by opening or closing a gate valve located ~670 cm from the driven section. Further description of the two configurations can be found in sections 2.2 (LS) and 2.3.1 (TOF-MS). Piezoelectric pressure transducers (Dynasen CA1136) are used to mark the passing of the shockwave. The pressure transducer spacing is a known constant which allows the time interval between the triggering of each transducer and the one preceding it to be used for calculating the shock velocity, which is then used to calculate the state conditions. Both diagnostics are sufficiently downstream of the shock initiation to allow the shockwave to become fully formed before reaching the observation locations. Mixtures are created in a dedicated glass mixing vessel using partial pressures. Liquid fuels are degassed using liquid nitrogen multiple times to

ensure the removal of any air or impurities before being added to the mixture. Figure 3.2 shows the DFST setup at ANL.

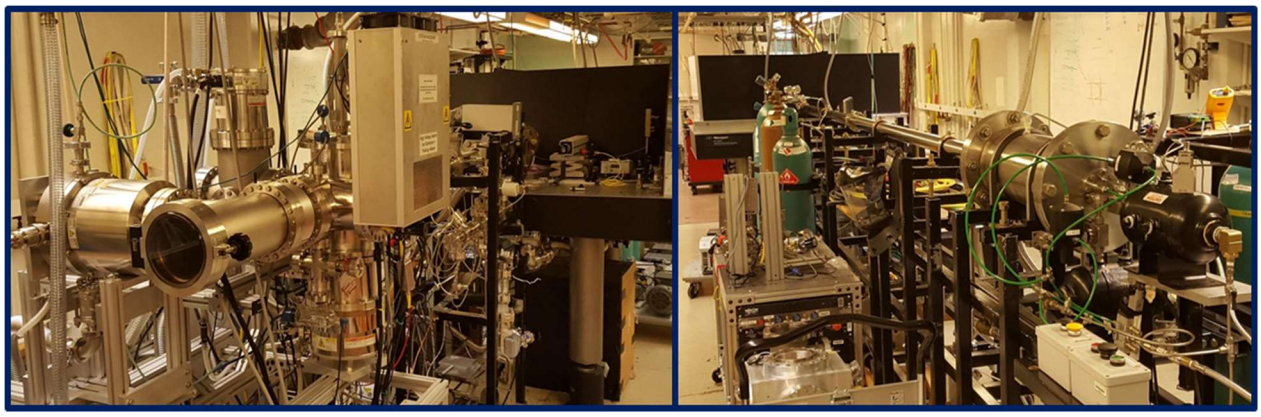

Figure 3.2: DFST setup at Argonne National Laboratory. [Provided by Dr. Robert Tranter]

Prior to starting experiments, the driver and driven section are evacuated. The chamber behind the bellows is pressurized to seal the driver section from the driven section and the driver section is filled with helium while the driven section is filled with the prepared gas mixture. The fill pressures of each section, P_4 for the driver and P_1 for the driven, are chosen to target the desired state conditions. Once the pressures are set, the fast acting pneumatic valve is actuated, releasing helium into the driven section. A uniform shockwave is formed which produces the desired thermodynamic state conditions by shockwave compression of the test gas in the driven section. The use of the fast-acting pneumatic valve to initiate the shockwave, as opposed to the traditional bursting of a diaphragm, allows for highly repeatable shock conditions and reduces the time between experiments.

2.1.2 High Repetition Rate Shocktube

A detailed description and characterization of the ANL high repetition rate shocktube (HRRST) can be found in Tranter and Lynch [5]. A brief description is provided here. Similar to a traditional shocktube, the HRRST consists of a driver and driven section, but the two sections

are separated by a solenoid-actuated driver valve and the apparatus is only ~69 cm long with an internal diameter of the driven section of only 0.635 cm. The shocktube is designed to be modular such that multiple configurations can be utilized depending upon the desired diagnostics. To accomplish this, the driven section is constructed of multiple segments as opposed to one continuous, single bore tube. To ensure precise alignment of the bore, the sections are connected with a boss and socket arrangement. The HRRST is designed to operate automatically at up to 4 Hz over periods of several hours. The solenoid valve is cycled by triggering the power supply through a pulse generator (SRS DG-645). In order to ensure proper evacuation of the HRRST between each shock, five pneumatic vent valves are located along the HRRST body. These valves are timed relative to the opening and closing of the solenoid valve to ensure proper evacuation of the gas between each shock without interfering with the shock behavior during the data collection period. This is controlled through external LabVIEW software and can be adjusted as necessary for various timing conditions. The velocity of the incident shock wave is calculated based upon the time intervals from the shockwave passing and triggering the piezoelectric pressure transducers (Dynasen CA1136) which are mounted in each of the pneumatic valve bodies and spacer sections. Figure 3.3 shows the HRRST bench top setup.

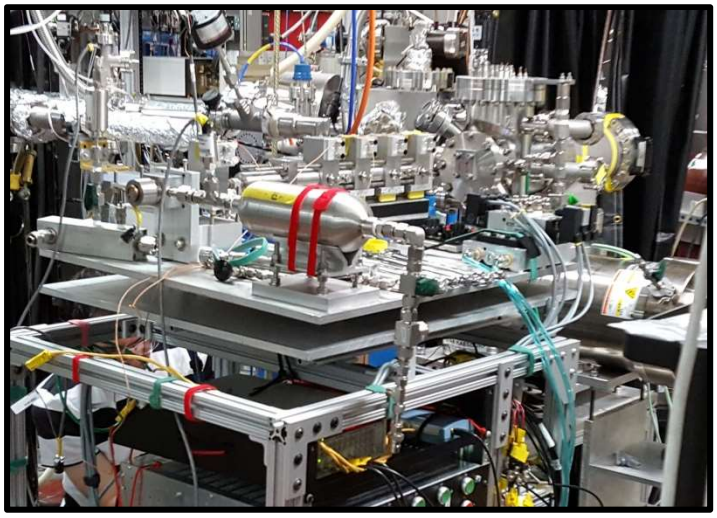

Figure 3.3: HRRST bench top facility in position at the Advanced Light Source at Lawrence Berkeley National Laboratory

Mixtures are made in an external mixing rig with a holding tank which is automated to provide a continuous gas flow. The current configuration allows for three possible gas flows. Each flow line contains a controller and a solenoid valve, as well as a by-pass line to avoid the flow controller and the solenoid valve if necessary. All three lines come together just after the solenoid valves and go through a back pressure regulator before either flowing to a vent or directly into the holding tank. The holding tank is directly connected to the fill reservoir on the HRRST and the pressure is controlled via an inline vacuum regulator. Pneumatic valves control whether the flow is exhausted to atmosphere or into the tank. The mixture composition is controlled by the relative flow rates of each channel. Figure 3.4 shows a flow schematic of the mixing facility.

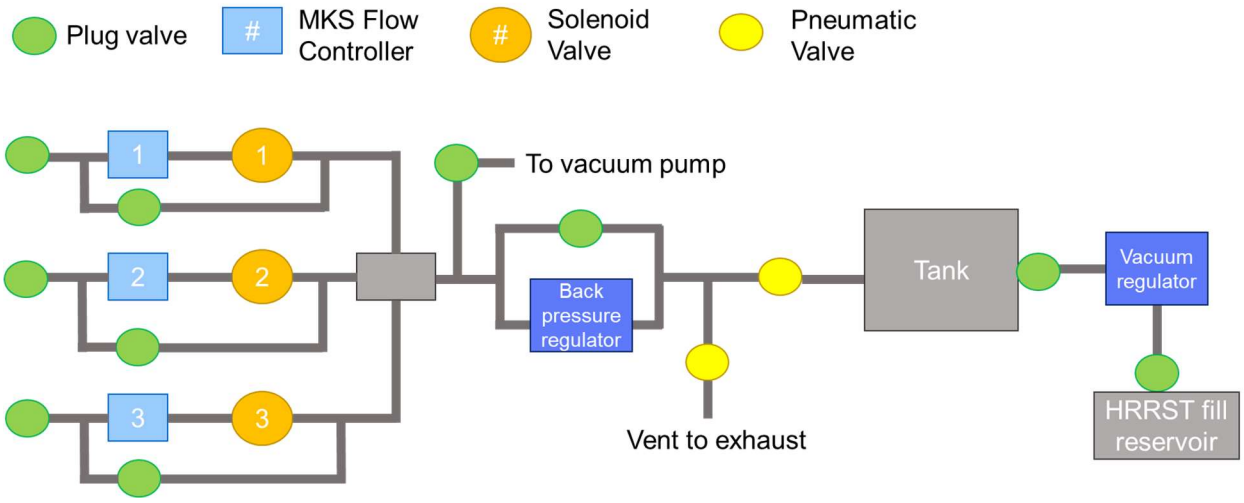

Figure 3.4: Flow schematic for the external mixing setup for the HRRST.

The entire system can be manually actuated but generally operates under automatic control using a LabVIEW program. When a new mixture is needed, the tank is evacuated and flushed twice with the main bath gas. The settings are then adjusted to provide the desired mixture composition. A dwell period is set for the system to vent to atmosphere to allow the flow rates and thus composition to stabilize. After this period is complete, the flow is routed into the mixing tank. Once the tank reaches the high pressure set-point, the pneumatic valve to the tank is shut, pausing the mixture process. During operation, the pressure of the tank is measured and if the pressure drops below the minimum set point, the system begins to fill until it reaches the maximum pressure again. This allows for a continuous and consistent gas supply throughout the course of experiments. The set points and flow rates are set such that the system can maintain adequate back-pressure for a consistent P1 through the course of operation. A pneumatic valve controls flow of the mixture from the fill reservoir into the shocktube. The timing of the opening and closing of the fill valve is controlled along with the exhaust valve timing to ensure continuous and consistent operation through repetitive cycles. In addition to the high repetition rate, the HRRST also provides the capability to conduct experiments at higher pressures than can

be achieved in the DFST. Thus, the HRRST bridges the gap between the low pressure pyrolysis experiments of the DFST to pressures found in combustion applications.

2.2 Laser Schlieren

Laser schlieren densitometry (LS) is an optical technique that offers a combination of resolution and sensitivity ideal for fast chemical and physical processes. Shocktube pyrolysis reactions occur on short time scales (<2 ms), so they require diagnostics with response times faster than 1 ms. LS uses a narrow laser beam to measure density changes by correlating the beam deflection with the local density gradient. Keifer heavily validated this technique for application to shocktube kinetic studies [6]. A brief description of the operating principles for this technique and its setup at ANL with the DFST are provided here. In order to perform this measurement, the DFST has two parallel optically transparent quartz windows located ~550 cm from the driver section. The long distance from the driver section ensures the shockwave is fully developed prior to passing the observation point. A continuous wave laser (633-637 at 6-8mW) is aligned across the diameter of the shocktube (perpendicular to the shocktube axis) and a series of mirrors are used to center the beam on a quadrant split photodiode which allows for measurement of beam deflection during the course of an experiment. In order to determine the state conditions at the observation point, six piezoelectric pressure transducers (Dynasen CA1136) measure the velocity of the incident shock. The transducers are spaced 12 cm apart and centered on the quartz windows as shown in the experimental schematic presented in Figure 3.5. The incident shock velocities, along with the fill pressure, P_1, and temperature, T_1, are used to calculate the post-shock pressure, P_2, and temperature, T_2, in the driven section.

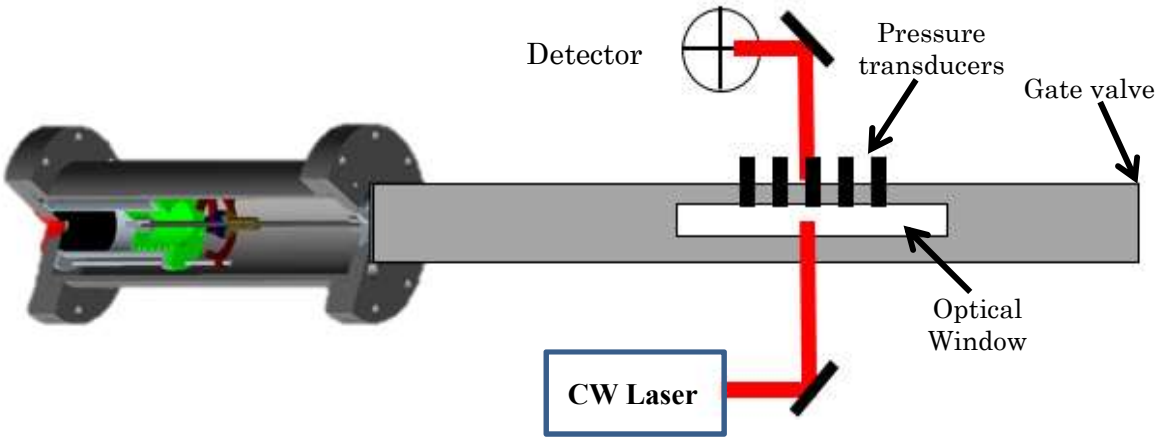

Figure 3.5: Schematic of DFST setup for LS experiments (not to scale).

During the shock tube experiments, the angular deflection of the laser beam, Θ, and the voltage response of the photodiode, V, are linearly proportional for small deflections. The beam deflection is calibrated to the voltage response of the photodiode by recording the photodiode response as the beam is deflected by a mirror rotating at a known angular velocity. This defines the voltage sensitivity to a change in angular deflection of the laser, $dV/d\Theta$. The deflection proportionality is given by Equation 3.1, where G_s is the detector gain and $V(t)$ is the time-dependent voltage response of the detector.

$$\theta \propto \frac{V(t)}{G_s}\left(\frac{dV}{d\theta}\right)^{-1} \tag{3.1}$$

This angular deflection is then correlated to the density gradient, $d\rho/dx$, by Equation 3.2 where W is the width of the shocktube, and K_L is the molar refractivity of the mixture.

$$\frac{d\rho}{dx} \propto \frac{\theta}{WK_L} \tag{3.2}$$

The change in density observed after the incident shockwave passes through the test gas mixture is caused by the reactions which are initiated by shock compression heating. The density gradient is proportional to the rate of reaction, r_i, and the heat of reaction, ΔH_i, for reaction i. Since these are dynamic systems, the changes in the number of moles, ΔN_i, for the corresponding reaction i

must also be accounted for with the specific heat, $C_{p,}$ and the system temperature, T. This relationship, based upon the methodology of Keifer [6], is given by Equation 3.3.

$$\frac{d\rho}{dx} \propto \sum_i r_i\left(\Delta H_i - C_p T \Delta N_i\right) \tag{3.3}$$

Using this relationship, the measured density gradient can be correlated with reaction progress. As the density changes are dependent upon thermodynamic changes originating from the reaction kinetics, this technique is not sensitive to thermally neutral reactions. Ideally, the change in density is attributable to one elementary reaction. If multiple endo- or exothermic reactions are active, it can complicate interpretation of the density gradient changes.

The mixture compositions and test conditions used in the current work are shown in Table 3.1. A more detailed description of the experimental setup and conditions for each experiment is provided in Table B.1 of the appendices.

Table 3.1 Experimental mixture compositions and state conditions for the DFST LS pyrolysis experiments

Fuel Species	Nominal Pressure (torr)	Temperature Range (K)	Krypton (mole fraction)	Fuel (mole fraction)
HMDSO	60	1400-1920	0.980	0.020
	120	1360-1830	0.980	0.020
	30	1520-2070	0.990	0.010
	60	1520-2030	0.990	0.010
	120	1430-2060	0.990	0.010
	30	1660-2020	0.995	0.005
	60	1560-2010	0.995	0.005
	120	1520-2010	0.995	0.005
	60	1725-2020	0.999	0.001
	120	1630-1980	0.999	0.001
	240	1580-1960	0.999	0.001
TMSO	30	1530-2150	0.980	0.020
	60	1520-2030	0.980	0.020
	120	1590-1970	0.980	0.020
	30	1715-2210	0.990	0.010
	60	1585-2150	0.990	0.010
	120	1550-2090	0.990	0.010
	30	1780-2170	0.995	0.005
	60	1680-2200	0.995	0.005
	120	1550-2050	0.995	0.005
HMCTSO	30	1600-2025	0.980	0.020
	65	1415-2020	0.980	0.020
	120	1410-1960	0.980	0.020

All three liquid fuels were obtained from Sigma Aldrich with purities of ≥97.5% for the TMSO (CAS Number 1066-40-6), ≥98.5% for the HMDSO (CAS Number 107-46-0) and ≥98% for the HMCTSO (CAS Number 541-05-9). The bath gas was ultra-high purity krypton (99.995%) obtained from Airgas. The driver gas was ultra-high purity helium (99.999%) also from Airgas.

2.3 Time-of-Flight Mass Spectrometry

In order to accurately model the decomposition behavior, it is important to know what species are relevant in the thermal decomposition process. Since the siloxanes are relatively unstudied in the gaseous phase, little is known about about the composition or quantity of the

intermediate species. Time-of-flight mass spectrometry (TOF-MS) allows for the collection of time resolved speciation data during pyrolysis with time resolution not possible via other techniques. In this configuration, the endwall of the shocktube is replaced by a nozzle and directly coupled to a Kaesdorf time-of-flight mass spectrometer (TOF-MS). A skimmer is placed between the nozzle and the ion source to further limit the gas flow into the mass spectrometer chamber and to create a molecular beam that can be aligned in the ion source for maximum signal. The Kaesdorf TOF-MS is designed for use with continuous (e.g., electron ionization, continuous wave (CW) photoionization) and pulsed (e.g., pulsed laser) ionization sources. In this work, two CW sources were used, electron impact at ANL and photoionization at the Advanced Light Source (ALS) at Lawrence Berkeley National Laboratory (LBNL). Ions were created by interaction of the ionization source with species in the molecular beam. Ions were extracted into the mass spectrometer in well-defined packets by pulsing the voltages applied to the repeller and extractor plates. The signal used to trigger the voltage pulse also defines the start signal used to determine the flight times and hence masses of the ions. In all the experiments, the voltage pulse was applied for 1 μs at a frequency of 100 kHz, yielding a time resolution for probing the molecular beam of 10 μs. The amount of time from when the extractor plates are first pulsed and the ion reaches the detector is correlated with the mass of the ion, which can then be used to identify the species.

When analyzing the resulting mass spectra, it is important to be able to identify the mass peaks which are associated with the ionization of the parent molecule and separate those from the mass peaks associated with the products of decomposition. While ^{28}Si is the most abundant silicon atom, the isotopes ^{29}Si and ^{30}Si are also stable and occur naturally in non-trivial amounts. This leads to a strong three peak signature for most silicon compounds. Figures 3.6-3.8 show the

mass spectra resulting from electron impact ionization as identified by NIST [7] for each of the molecules in this study: HMDSO (Figure 3.6), TMSO (Figure 3.7), and HMCTSO (Figure 3.8). Note the cluster of three strong signals at m/z = 147, 148, and 149 associated with the ionization of HMDSO in Figure 3.6.

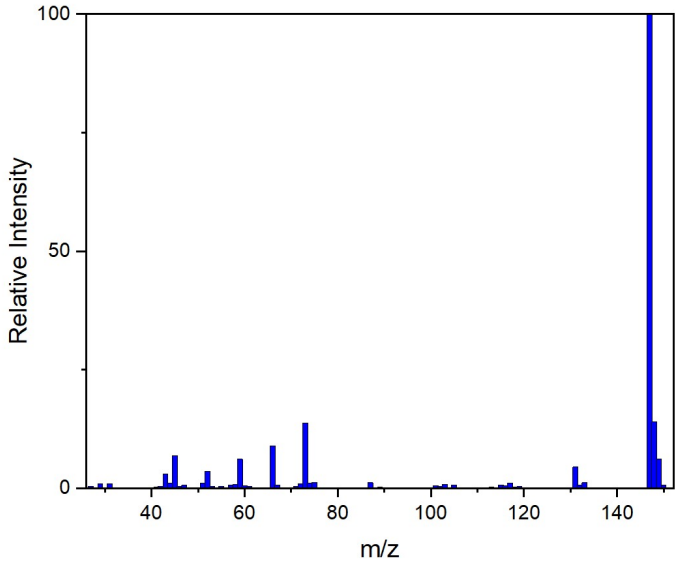

Figure 3.6: Electron impact mass spectra for HMDSO based upon the relative intensities listed by NIST [7]

As seen in Figure 3.6, in addition to the strong cluster of signals at 147, 148, and 149, HMDSO also has minor peaks around m/z = 73 and 132 due fragmentation during ionization. The peak at 73 is a common minor peak for organic silicon species as it correlates with the trimethylsilyl radical which is a non-trivial fragmentation product. Although not shown in Figure 3.6, mass peaks also appear around 162 in some experiments and are associated with the ionization of the unfragmentend parent molecule.

Figure 3.7 shows that TMSO has a primary signal at m/z = 75 with two minor features at 76 and 77 associated with the ^{29}Si and ^{30}Si isotopes. The most prominent minor features for TMSO occur at m/z = 45 and 47, and a minor peak can be seen around m/z = 90, which is the result of the unfragmented parent. Although not shown on Figure 3. 7, the primary feature for TMSO is

at m/z = 207 with two minor trailing features at 208 and 209 associated with the ^{29}Si and ^{30}Si occurrences. Also not shown in the figure, minor peaks may appear around 222 due to the unfragmented parent.

The primary and minor features of the mass spectra for HMCTSO are shown in Figure 3.8. Some of the features overlap with the minor peaks of TMSO and HMDSO. The strongest signals are at ~m/z = 210.

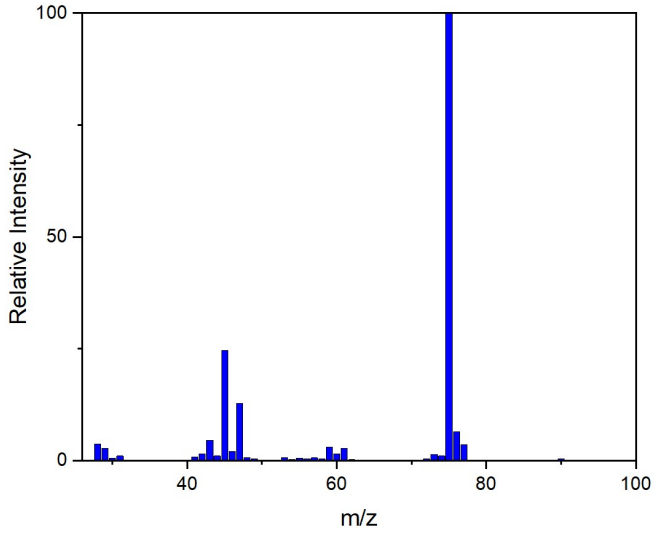

Figure 3.7: Electron impact mass spectra for TMSO based upon relative intensities as reported by NIST [7]

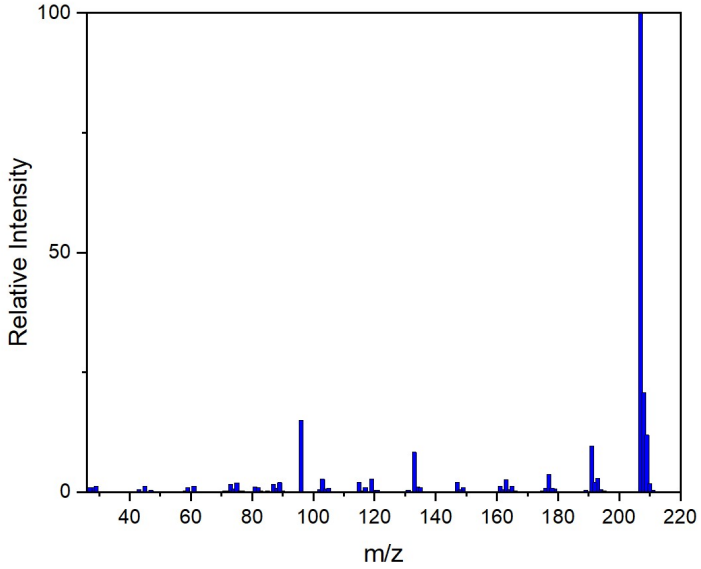

Figure 3.8: Electron impact mass spectra for HMCTSO based upon relative intensities as reported by NIST [7]

In this study ionization is performed through two methods, electron impact (EI) or photoionization (PI). In the DFST, EI is used to generate ions for analysis by TOF-MS. However, this causes significant fragmentation of the molecules making assignment of mass spectral features to discrete species difficult. Hence, it can be challenging to determine exactly which species are formed during pyrolysis of siloxanes using EI TOF-MS. EI also does not allow for the differentiation between isomers or between compounds of similar molecular masses. Alternatively, photoionization reduces fragmentation making it easier to differentiate parent masses from minor fragments in the observed mass spectra.

2.3.1 DFST TOF-MS Experiments

As mentioned in the description of the DFST, the gate valve defines the end of the driven section for the LS experiments. When the gate valve is opened, it allows the shockwave to travel to the end of the shocktube where the nozzle for the TOF-MS system is located. For measuring the state conditions at the nozzle, three pressure transducers are spaced 76.56 mm apart with the last transducer located 25 mm before the sampling nozzle. The close proximity of the transducers to the sampling location allows for consideration of attenuation or acceleration of the shockwave downstream from the LS section. The operating principles for the pyrolysis experiments are the same as for the DFST with LS diagnostic, except the reactions are probed behind the reflected shock instead of the incident shock. (So the state conditions are T_5 and P_5 instead of T_2 and P_2.) Figure 3.9 shows the DFST configuration for TOF-MS experiments.

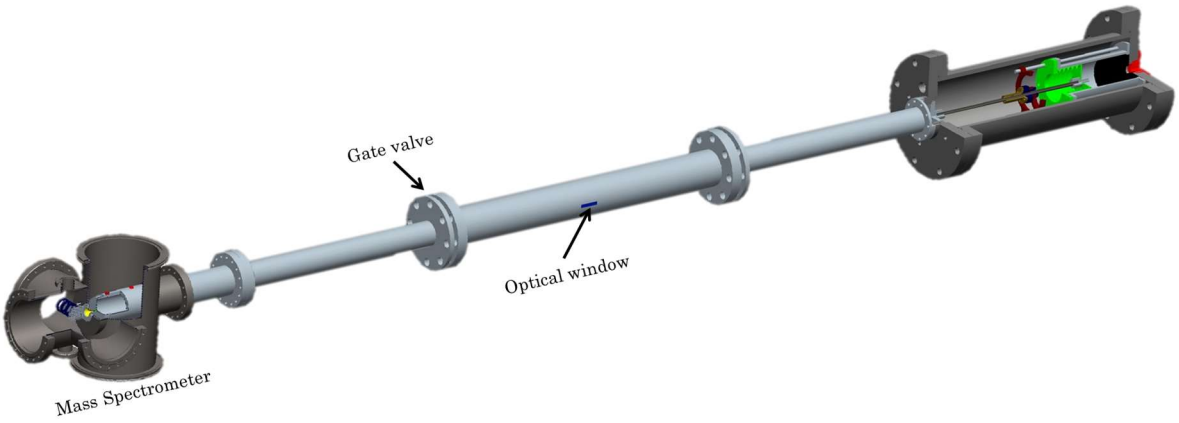

Figure 3.9: DFST configuration for TOF-MS experiments. The gate valve is placed in the open position to allow gas flow from the driven section to the mass spectrometer.

Table 3.2 shows the mixture compositions and range of state conditions explored in this study. A more detailed description of the experimental setup and conditions for each experiment is provided in Table B.2 of Appendix B.

Table 3.2 Experimental mixture compositions and state conditions for DFST TOF-MS pyrolysis experiments

Fuel Species	Nominal Pressure (torr)	Temperature Range (K)	Argon (mole fraction)	Neon (mole fraction)	Fuel (mole fraction)
HMDSO	185	1590-1980	0.020	0.975	0.005
TMSO	155	1350-1430	0.020	0.975	0.005
HMCTSO	220	1780	0.020	0.975	0.005

As with the LS experiments, the three liquid fuels were obtained from Sigma Aldrich with purities of ≥97.5% for the TMSO (CAS Number 1066-40-6), ≥98.5% for the HMDSO (CAS Number 107-46-0) and ≥98% for the HMCTSO (CAS Number 541-05-9). The argon (99.999%) and neon (99.999%) were obtained from Airgas as was the driver gas, helium (99.999%). Neon was used as the bath gas in these experiments due to its relatively high ionization energy. While neon will ionize at the ionization energies used in these studies, the relative strength of the signals are weaker than for other inert gases and allow other species to be detected in the vicinity

of the characteristic neon peaks (which are nominally located at m/z = 20 and 22). Stronger signals can saturate the detector obfuscating signals from species at similar m/z values. The detailed spectrometer settings for each experiment are provided in Table B.3a of the Appendix and Table B.3b shows the masses used for calibration.

2.3.2 HRRST TOF-MS with Photoionization Experiments

The HRRST TOF-MS system can be modified to use photons for ionization via ultraviolet light. In order to acquire high fidelity photoionization data, the HRRST mass spectrometer is directly coupled to the Chemical Dynamics Beamline (Beamline 9.2.1) at the ALS at LBNL. The ALS provides highly-tunable, high-vacuum ultraviolet (HVUV) emission which allows differentiation between fragments, isomers, and same mass species. This is accomplished by scanning a range of ionization energies and providing photoionization data in addition to the basic m/z spectra. In order to reduce the incidence of higher harmonic light reaching the ion source, an argon gas filter is located upstream of the end station which the HRRST occupies. This filter should absorb any higher harmonics that are above the ionization energy of argon (15.56 eV). However, experiments with the gas filter on and off, demonstrated that significant high harmonic light was escaping the gas filter, causing photo-fragmentation. The higher harmonics were attenuated through the gas filter, but enough would still pass through to affect the ionization curves. A magnesium fluoride (MgF_2) window is located upstream of the end station, but downstream of the gas filter, to provide an additional filter for blocking higher harmonic light that might still be transmitted. Since the ionization energy of MgF_2 is around 10.8 eV, the window filters any light at higher energies. While the gas filter was continuously used throughout the experiments described in this study, the MgF_2 window was used intermittently. The use of the MgF_2 window was limited for a variety of reasons. First, the windows limited the

achievable ionization energies to below 10.8 eV and attenuated the signal above 10.5 eV. Additionally, window positioning would become limiting after long use, as the window would burn, further limiting signal transmission. This required constant repositioning of the window in order to find regions of high transmission.

For the HRRST TOPF-MS experiments, argon was used as the bath gas due to its ionization energy. Argon was bubbled through the liquid siloxane using the argon flow to provide a targeted concentration (specifically by controlling the Ar pressure relative to the vapor pressure of the siloxane). Figure 3.10 shows the configuration and flow of the bubbler system. The siloxane percentage in the outlet gas is calculated by Equation 3.4.

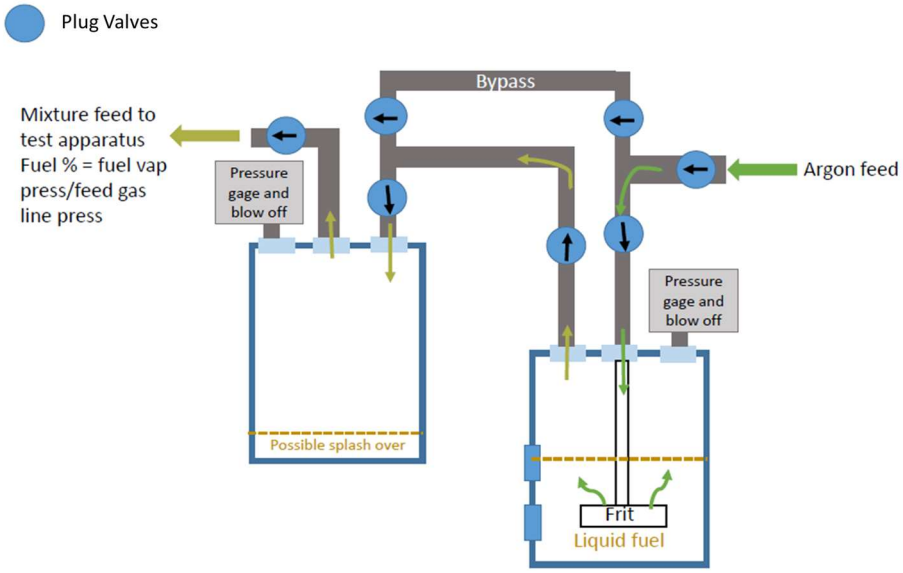

Figure 3.10: Flow schematic for the bubbler system as setup for a liquid fuel being diluted with argon.

$$Bubbler\ Outlet\ Fuel\ \% = 100 \times \frac{Vapor\ pressure\ of\ the\ fuel}{Pressure\ of\ bath\ gas\ inlet\ line} \tag{3.4}$$

This mixture was then further diluted with argon introduced through a second flow controller. The siloxane percentage of the final mixture is calculated by Equation 3.5

$$Fuel\ \%\ in\ Mix = Bubbler\ Outlet\ Fuel\ \% \times \frac{Bubbler\ Flow\ Rate}{Total\ Flow\ Rate} \tag{3.5}$$

where the total flow rate is the summation of all the contributing flow rates. For these experiments two flows were used: the flow through of the bubbler and the secondary argon dilution flow.

A variety of pressures and temperatures were explored across a range of ionization energies. The experimental conditions are listed in Table 3.3. Each set is defined by the experimental date and "battalion" number, where each battalion includes a series of experimental data at the same mixture and state conditions. The state conditions are listed for the battalion groupings, generally the only difference from battalion to battalion at the same state conditions is the ionization energy. The number of shocks averaged for each battalion is also listed. A more thorough description of each experimental set is provide in Table B.4 of the appendix. Spectrometer settings are detailed in Table B.5a and the beamline settings are detailed in Table B.5b.

Table 3.3: Experimental conditions and mixture compositions for TOF-MS pyrolysis experiments conducted with the HRRST at the Advanced Light Source

Fuel	Percentage in Ar (%)	Battalions	Temp (K)	Press (atm)	Ionization Energy (eV)	MgF_2	# Shocks Averaged	Repetition Rate
HMDSO	0.6	16-33	1580	12.2	12-7.75	No	100	1 Hz
HMDSO	0.6	36-45	1580	12.2	10.5-7.75	Yes	100	1 Hz
HMDSO	0.6	51-68	1600	6.2	12-7.75	No	100	I Hz
HMDSO	0.6	69-79	1600	6.2	10.75-7.75	Yes	100	1 Hz
HMDSO	0.6	83-96	1715	15.8	12-8.75	No	100	1 Hz
TMSO	0.6	61-78	1380	9.7	12-7.75	No	100	1 Hz
TMSO	0.6	79-88	1380	9.7	10.75-7.75	Yes	100	1 Hz
TMSO	0.6	8-28	1500	6.1	13-8	No	100	1 Hz
TMSO	0.6	29-35	1500	6.1	10.75-8	Yes	100	1 Hz
TMSO	0.6	94-111	1580	12.0	12-7.75	No	100	1 Hz
TMSO	0.6	119-127	1580	12.0	10.75-7.75	Yes	100	1 Hz
TMSO	0.6	132-147	1650	7.2	12-8.5	No	100	1 Hz
HMCTSO	unknown	-	-	-	-	Yes	200	1 Hz

All siloxanes were obtained from Sigma Aldrich with purities of ≥97.5% for the TMSO (CAS Number 1066-40-6), ≥98.5% for the HMDSO (CAS Number 107-46-0) and ≥98% for the

HMCTSO (CAS Number 541-05-9). The argon (99.999%) was obtained from Airgas. Helium (99.999%) was used as the driver gas and also obtained from Airgas.

Using the crystalline HMCTSO presented a unique challenge through the course of the experiments at the Advanced Light Source. The bubbler system and mixing facility were configured to provide 0.1% concentration, but shortly into the operation, the MS signal from the parent mass decreased significantly. Operation was halted to check for nozzle blockage due to particle build-up, but the nozzle was f clear enough to allow adequate flow into the mass spectrometer. Slight adjustments to the beamline settings did not improve the signal. Upon teardown of the bubbler after the experiments were completed, it was found that some of the crystals had become trapped in the outlet port leading to restricted gas flow. The bubbler is evacuated to the vapor pressure of the compound to remove air and impurities trapped in the bubbler. After the bubbler has been evacuated, such that only the liquid source reactant remains, it is pressurized with argon - approximately 40 psi for these experiments. The introduction of high pressure gas caused likely entrained the solid crystals which then became lodged in the outlet port. Unfortunately, this was discovered after the time allotted for the experiments had concluded, but a solution for future experiments with this and other solid crystalline fuels was developed. The outlet port can be modified with a mesh or wire filter to protect the opening such that particles cannot become trapped in the orifice.

3. Results

3.1 Laser Schlieren Results

The signal from the photodiode is translated into a density gradient, $d\rho/dx$., using the methods outlined above. Figure 3.11 shows a typical unprocessed data from the photodiode sensor from a 2% HMDSO experiment and the corresponding density gradient.

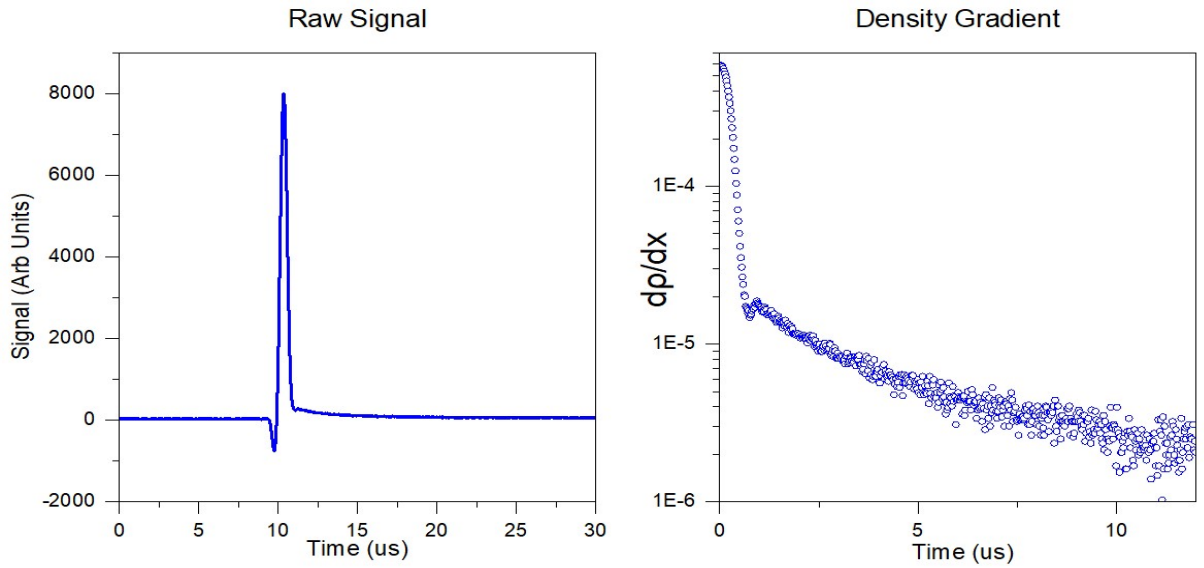

(a) (b)

Figure 3.11: Raw LS signal (a) and corresponding density gradient (b) for a 2% HMDSO in Kr experiment at 60 Torr (0.25 atm) and 1620 K.

3.1.1 Laser Schlieren Results for HMDSO

As outlined in Table 3.1, experiments spanned the pressure and temperature space at various concentrations for HMDSO in order to provide a robust set of experiments for developing and validating a thermal decomposition mechanism. Representative density gradients from the experiments are shown in Figures 3.12 – 3.14. The characteristics of the gradients provide valuable insight into the thermodynamic characteristics of the pyrolysis reactions. For each nominal pressure, three results are shown: 1. results from a temperature near the lower end of the detectable decomposition limits; 2. results where the reaction kinetics are starting to be convolved with the passing shockwave; and 3. an intermediate condition. The lowest detectable limit is defined as a condition where $d\rho/dx$ is approximately zero. The upper limit is defined as a condition where the beam steering of the laser due to the shockwave interferes with the endothermic reaction kinetics of the siloxane pyrolysis.

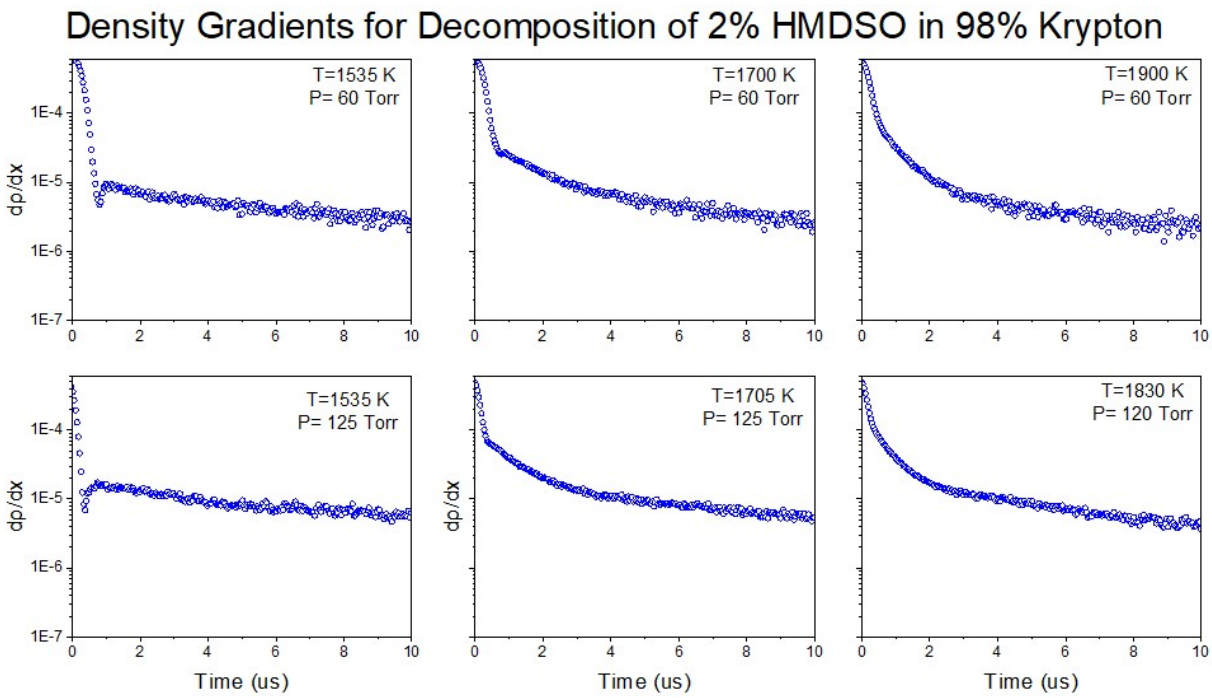

Figure 3.12: Density gradients for 2% HMDSO in Kr for multiple temperatures and pressures. See the text for additional details.

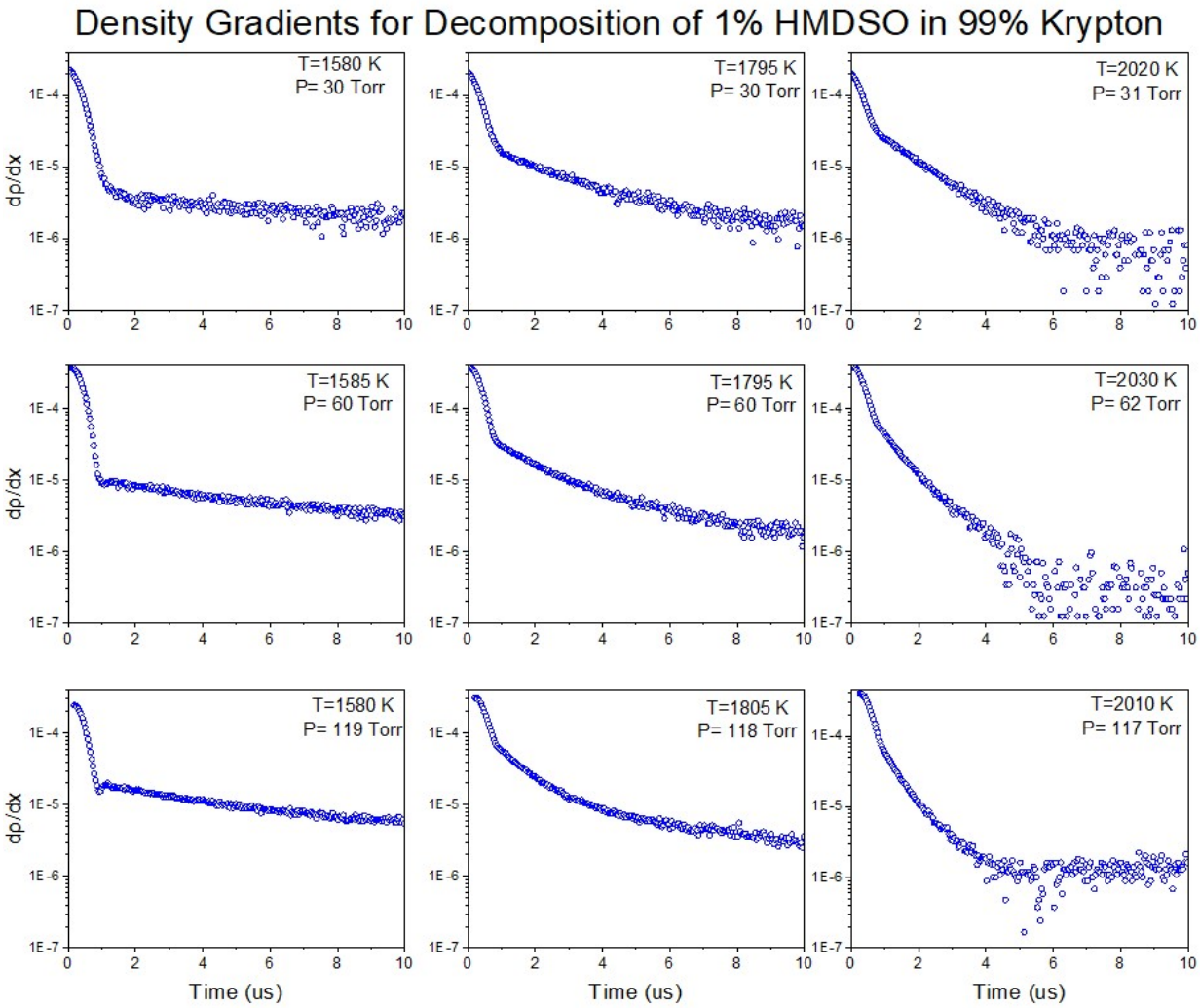

Figure 3.13: Density gradients for 1% HMDSO in Krypton across multiple temperatures and pressures. See text for additional details.

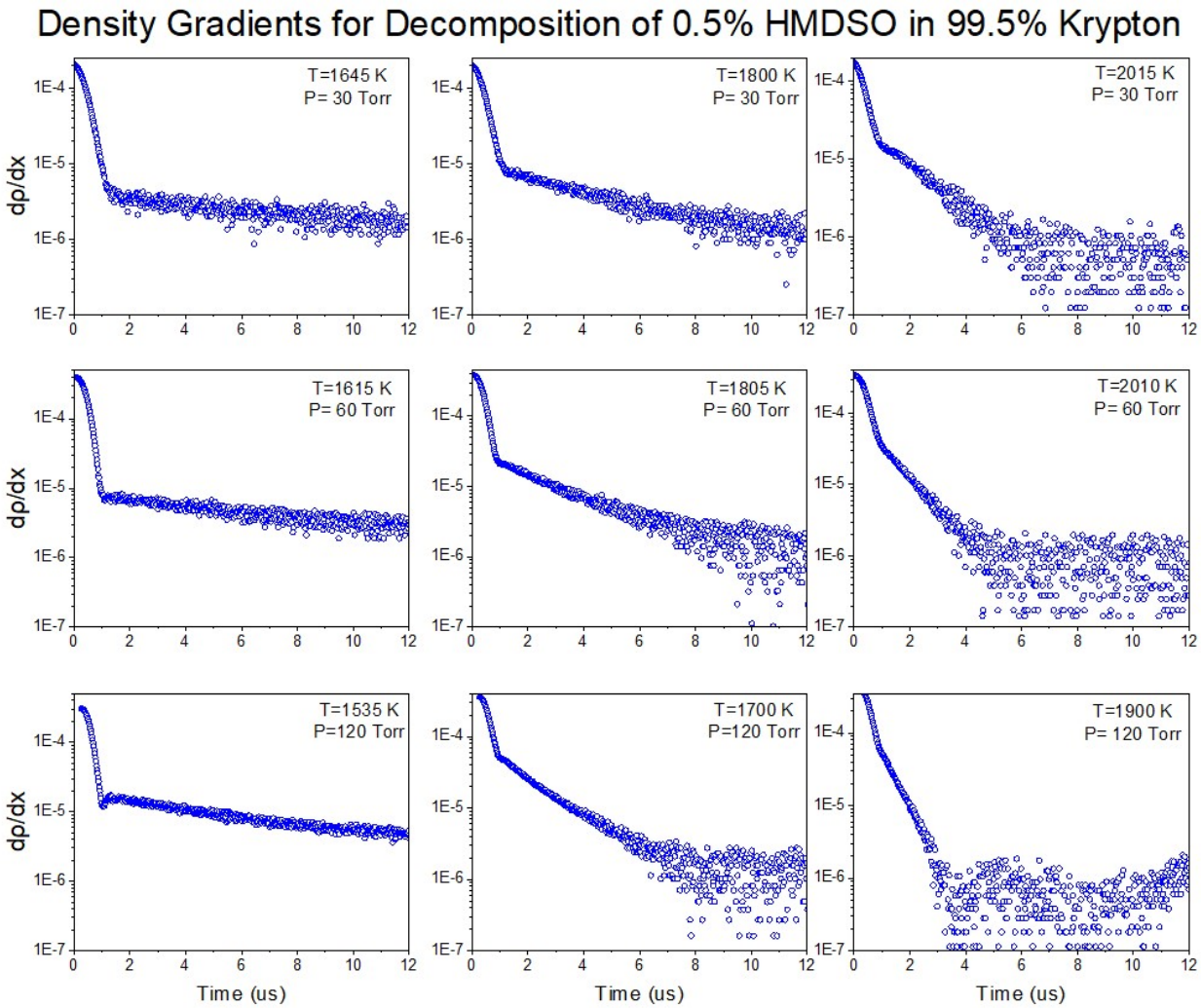

Figure 3.14: Density gradients for 0.5% HMDSO in Krypton across multiple temperatures and pressures. See text for details.

3.1.2 Laser Schlieren Results for TMSO

Representative density gradients from the TMSO experiments are shown in Figures 3.15 – 3.17.

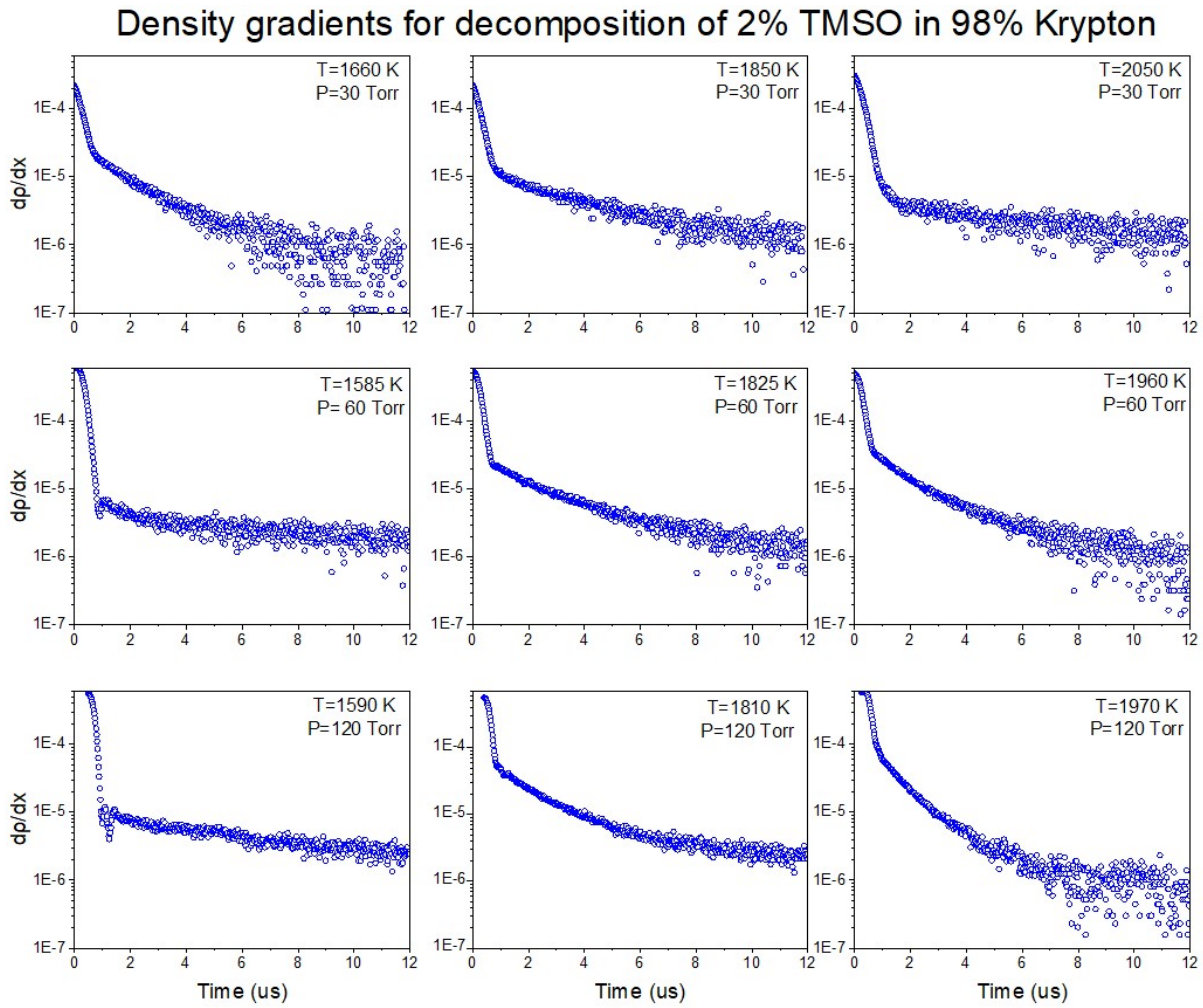

Figure 3.15: Density gradients for 2% TMSO in Krypton across multiple temperatures and pressures. See text in section 3.1.1 for details.

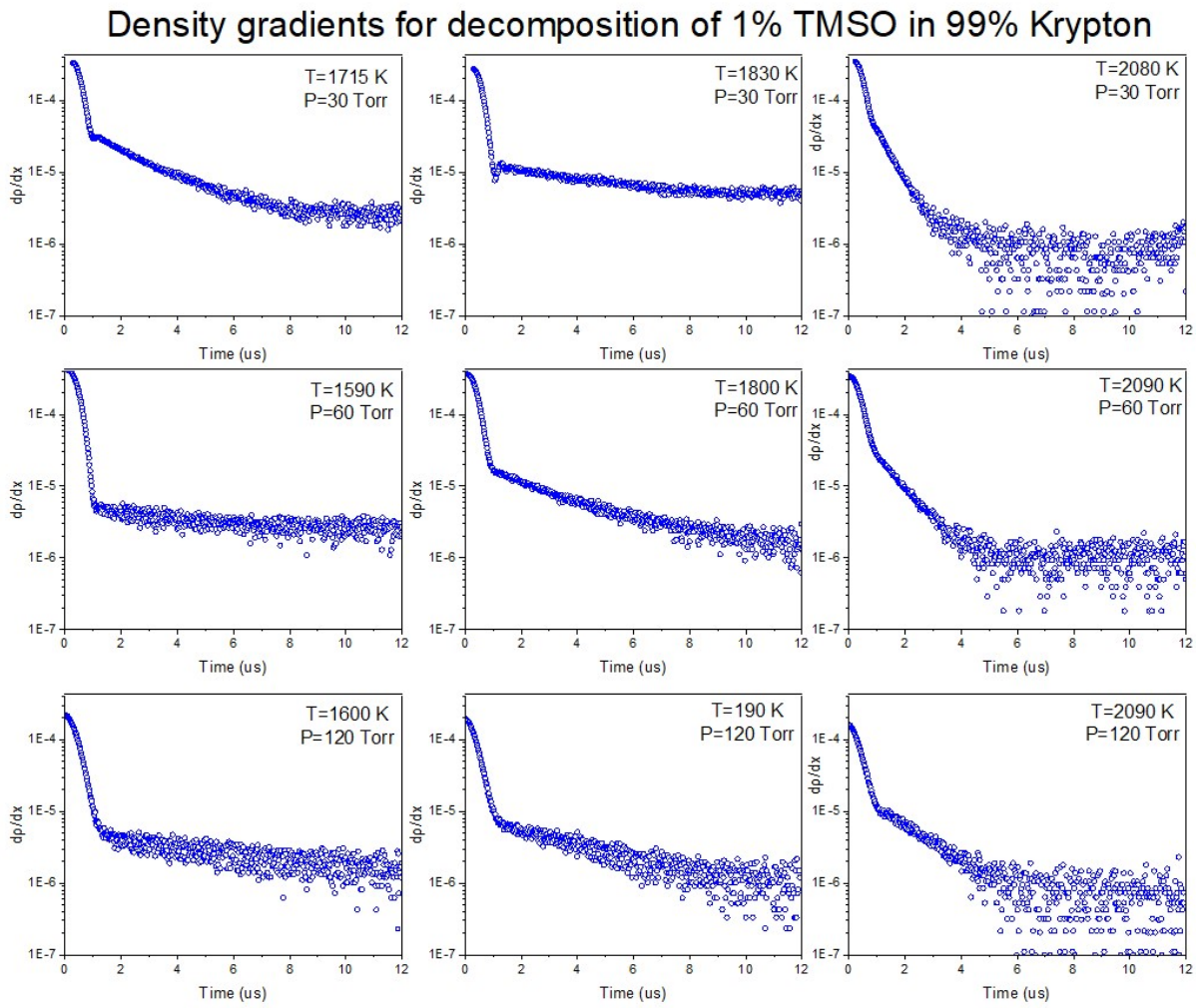

Figure 3.16: Density gradients for 1% TMSO in Krypton across multiple temperatures and pressures. See text in section 3.1.1 for details.

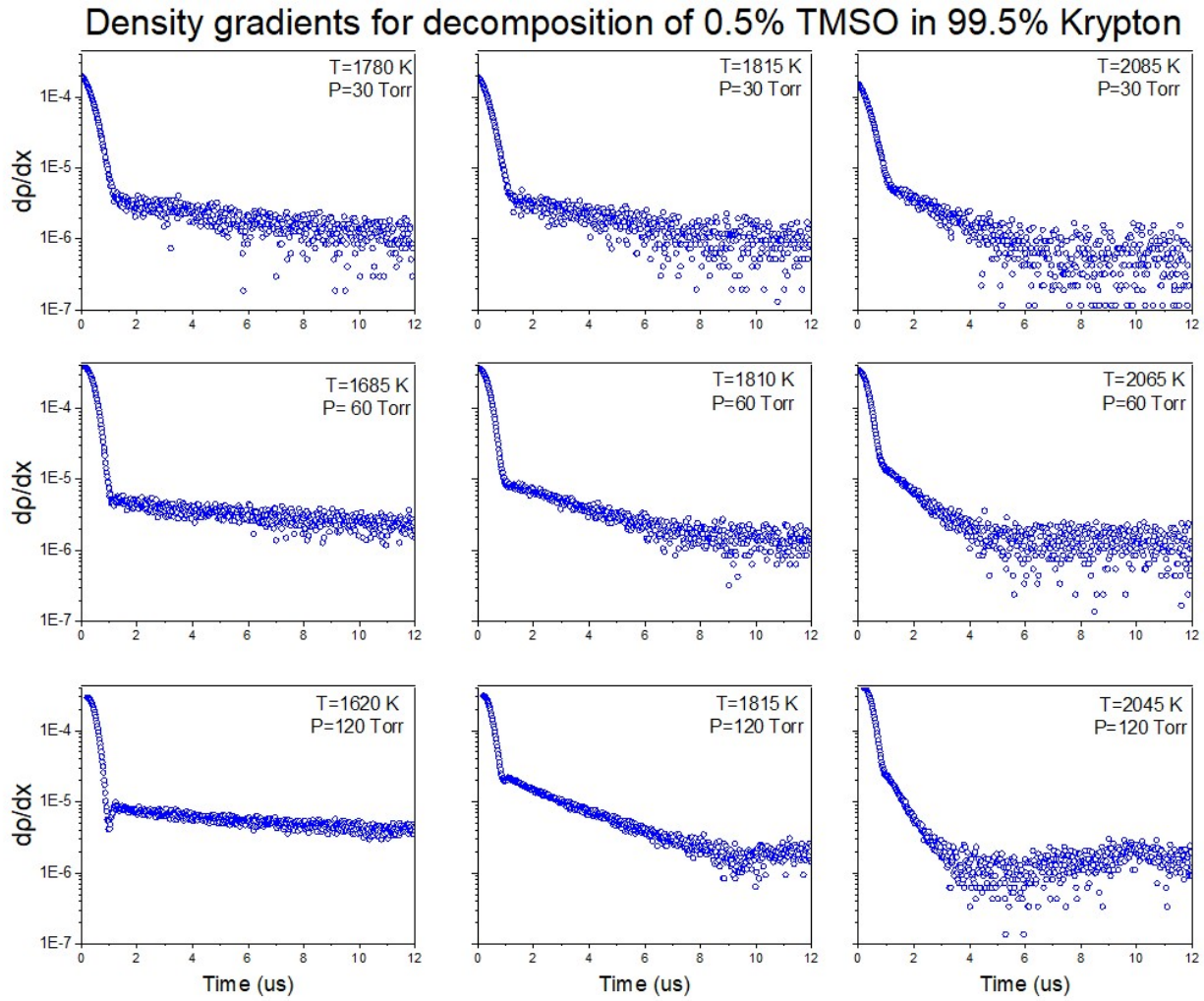

Figure 3.17: Density gradients for 0.5% TMSO in Krypton across multiple temperatures and pressures. See text in section 3.1.1 for details.

3.1.3 Laser Schlieren Results for HMCTSO

Representative density gradients from the HMCTSO experiments are shown in Figure 3.18.

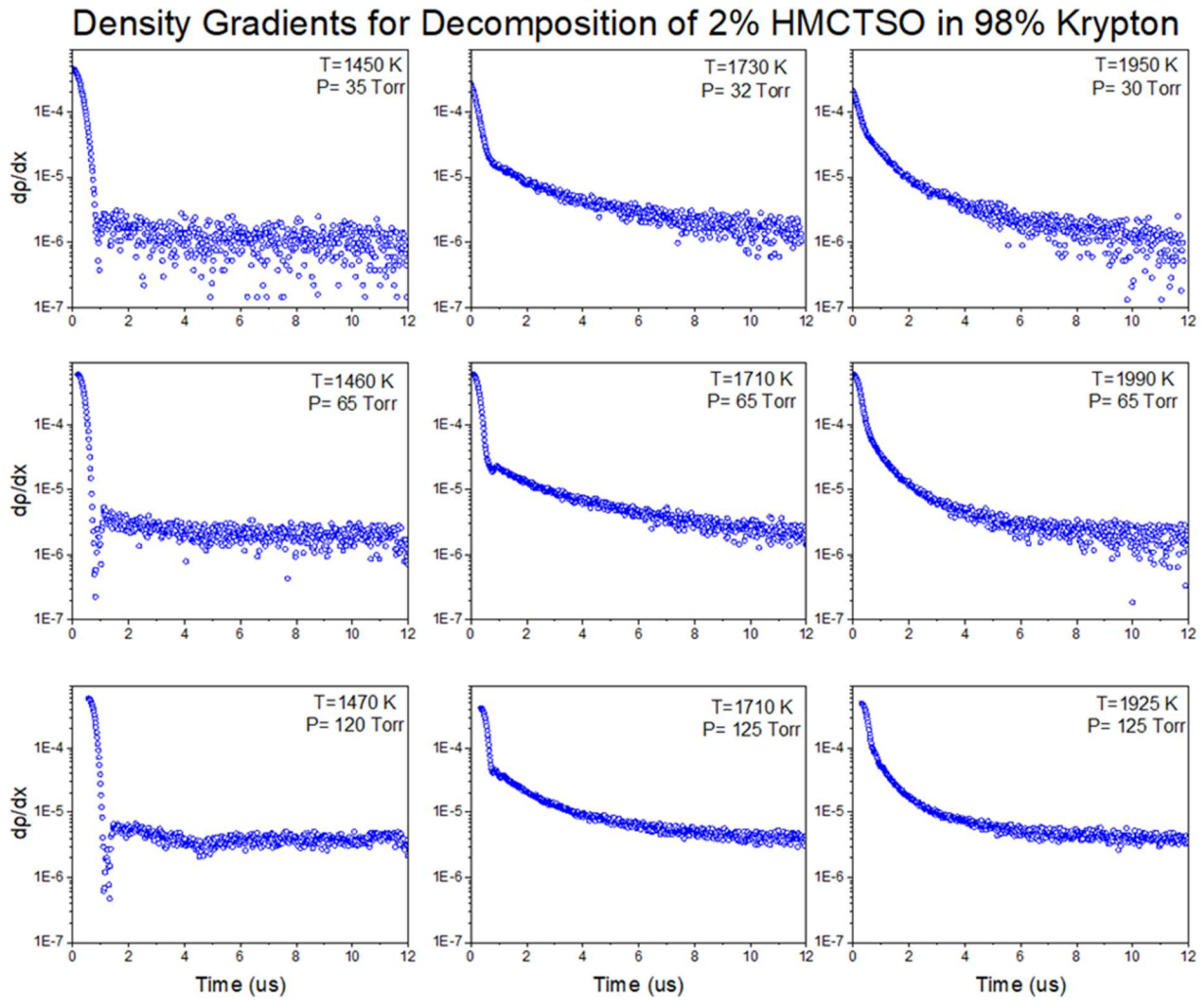

Figure 3.18: Density gradients for 2% HMCTSO in Krypton across multiple temperatures and pressures. See text in section 3.1.1 for details.

3.2 DFST TOF-MS Results

3.2.1 HMDSO TOF-MS Results (DFST)

As outlined in Table 3.2, a relatively small temperature and pressure space was explored in the DFST TOF-MS experiments for HMDSO. The experiments were designed to exploit the high repeatability of the DFST operation such that multiple shocks could be averaged. The averaging improves the signal-to-noise of the TOF-MS spectra. The following analysis focuses on ten repeated experiments at approximately 1610 K and 185 Torr. The resulting mass spectra from

the experiments were arithmetically averaged and the resulting averaged mass spectra at four reaction times (Pre-shock, 500 μs, 1250 μs, and 1850 μs) are presented in Figures 3.19 and 3.20.

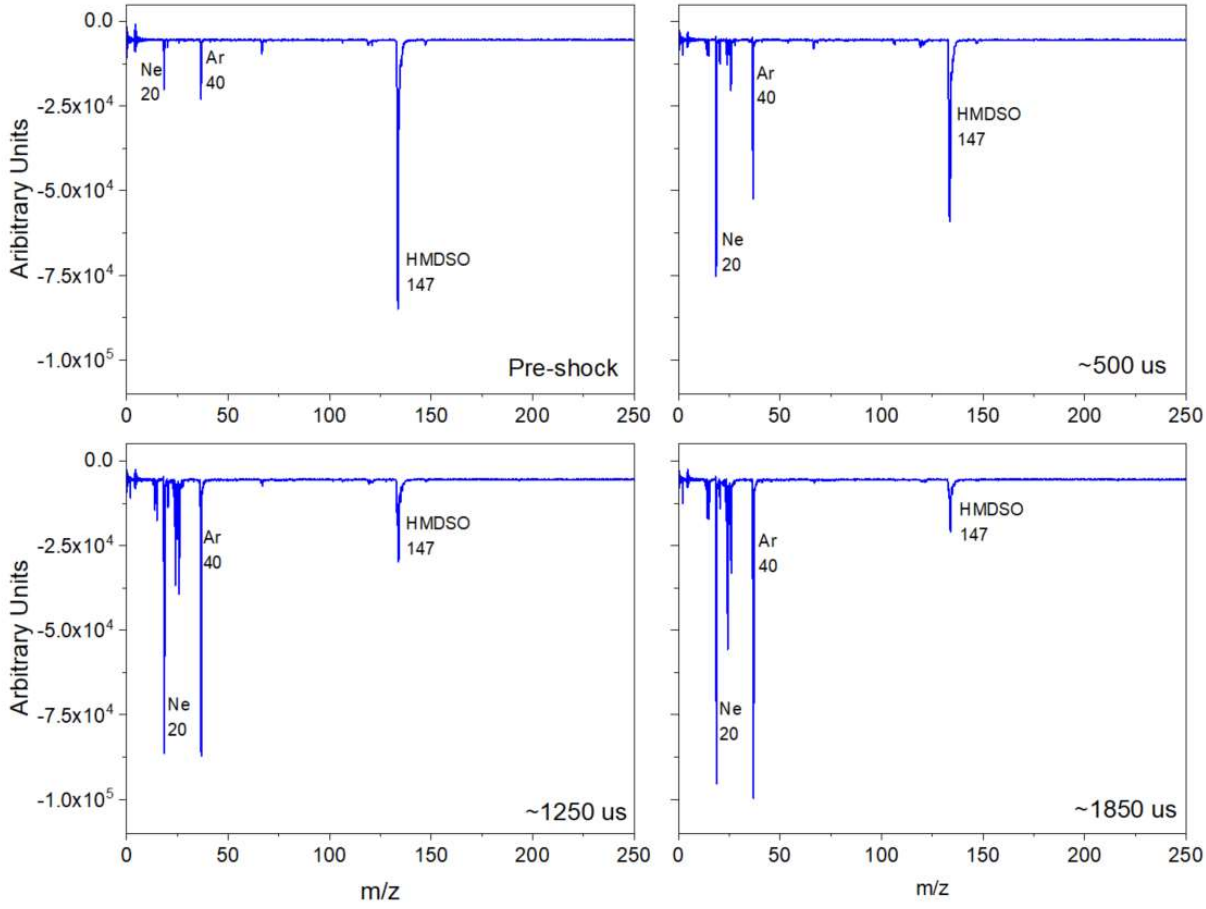

Figure 3.19: Mass spectra averaged from 10 experiments of 0.5% HMDSO, 2% Ar, and 97.5% Ne at 1610 K and 185 Torr. Four representative reaction times are shown: Pre-shock, 50 μs post-shock, 125 μs post-shock, 185 μs post-shock. m/z is the mass/charge except for the case of electron impact, the charge is approximately 1, so the ratio directly measures mass.

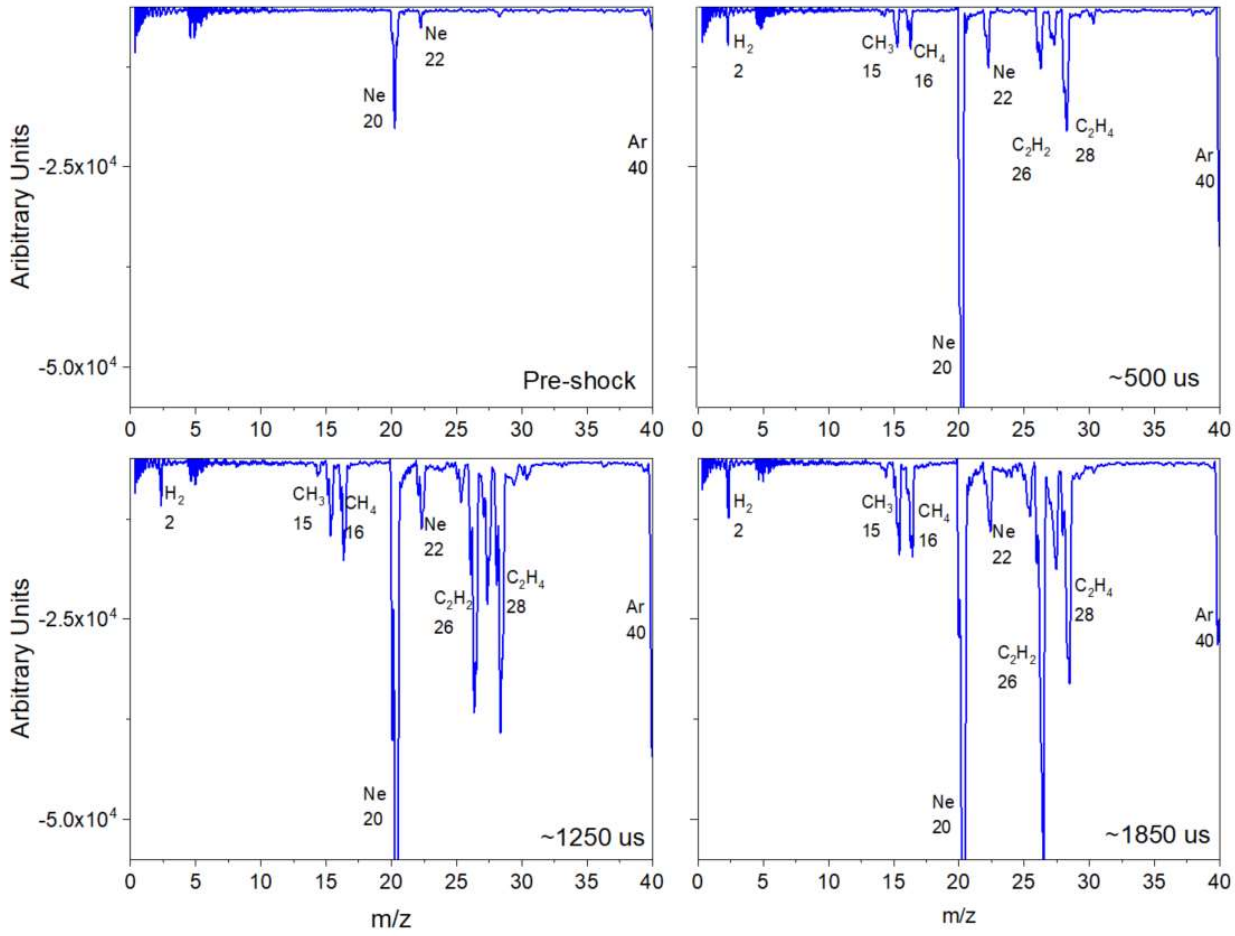

Figure 3.20: Mass spectra from Figure 3.19 highlighting the m/z = 0-40 range.

The main decomposition products identified are hydrogen (m/z = 2), methane (m/z = 16, 15), acetylene (m/z = 26, 25, 27), and ethylene (m/z = 28, 27, 26). Hydrogen first appears around 200 μs, methane around 350 μs, acetylene around 330 μs, and ethylene around 200 μs. A full list of the observed mass peaks and the time of their initial appearance is provided in Table B.6a of the Appendix.

3.2.2 TMSO TOF-MS Results (DFST)

Similar to the HMDSO experiments, a relatively small temperature and pressure space was explored in the DFST TOF-MS experiments for TMSO. Again, these experiments were designed to exploit the high repeatability of the DFST operation such that multiple shocks could be

averaged. The analysis focuses on ten repeated experiments at approximately 1410 K and 155 Torr. The resulting mass spectra from the experiments were arithmetically averaged and the resulting averaged mass spectra at four reaction times (Pre-shock, 50 μs, 125 μs, and 185 μs) are presented in Figures 3.21 and 3.22.

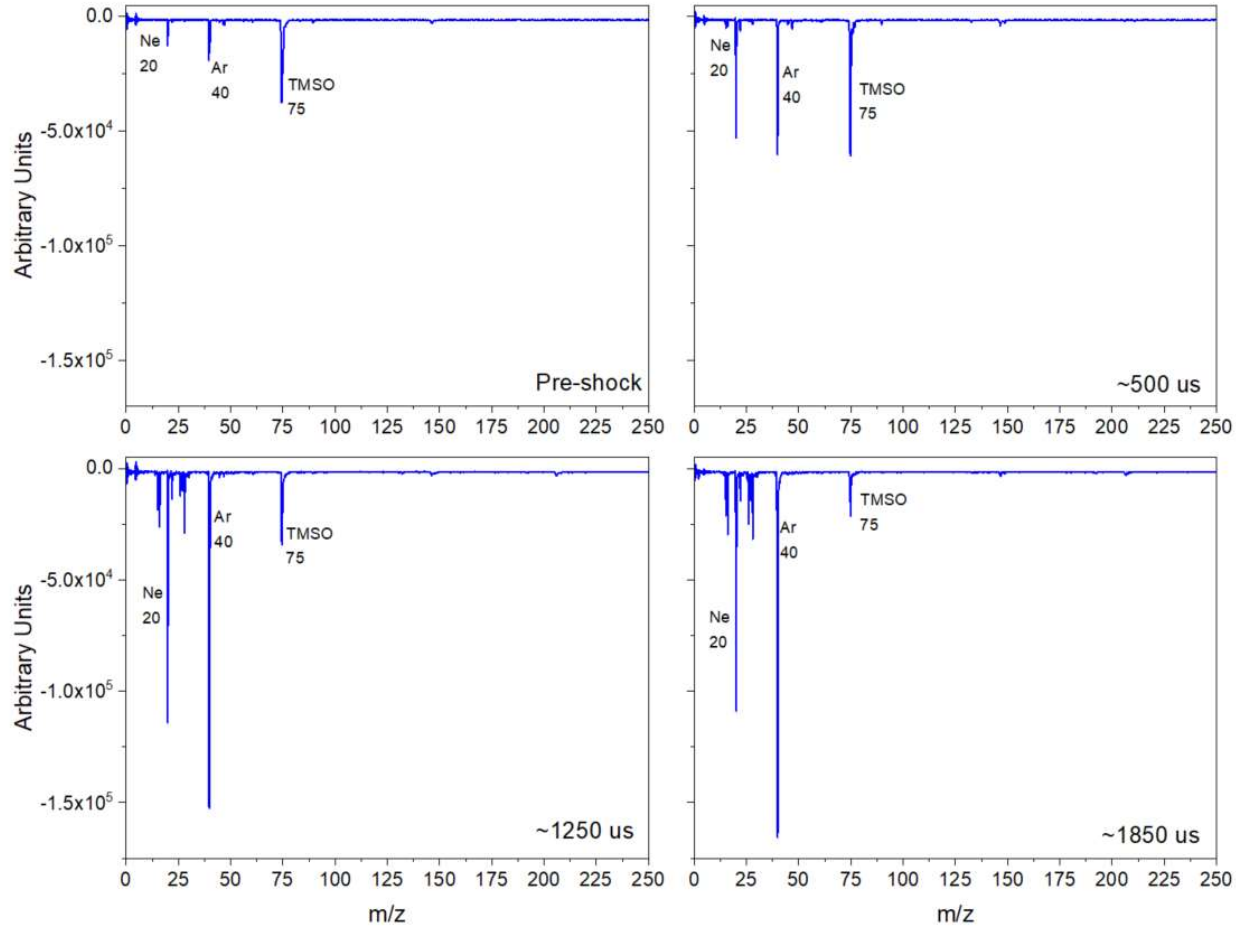

Figure 3.21: Mass spectra averaged from 10 experiments of 0.5% TMSO, 2% Ar, and 97.5% Ne at 1410 K and 155 Torr. Four representative reaction times are shown: Pre-shock, 500 μs post-shock, 1250 μs post-shock, 1850 μs post-shock. m/z is the mass/charge except for the case of electron impact, the charge is approximately 1, so the ratio directly measures mass

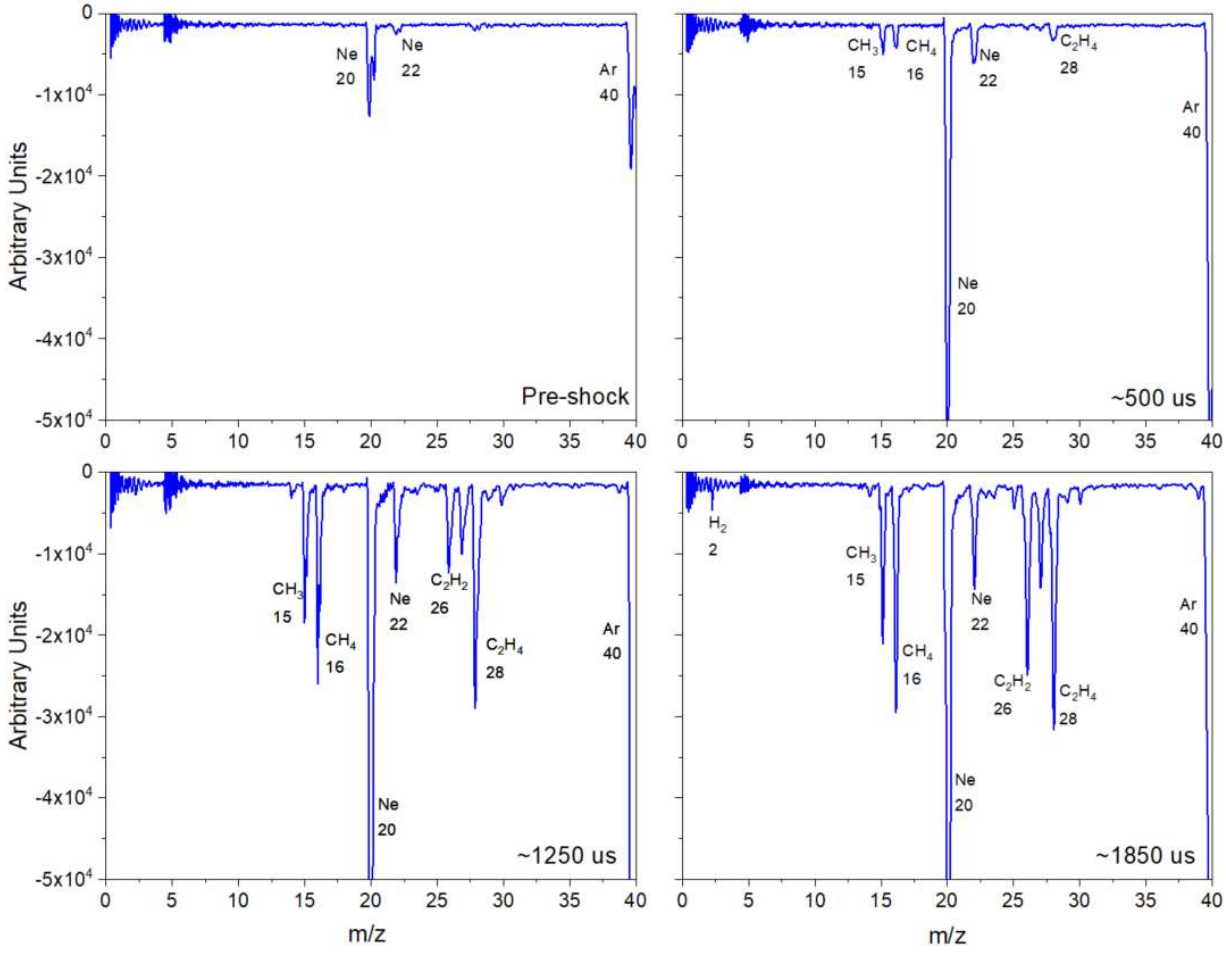

Figure 3.22: Mass spectra from Figure 3.21 highlighting the m/z = 0-40 range

The main decomposition products identified are hydrogen (m/z = 2), methane (m/z = 16, 15), acetylene (m/z = 26, 25, 27), and ethylene (m/z = 28, 27, 26). Hydrogen first appears around 650 μs, methane around 400 μs, acetylene around 400 μs, and ethylene around 250 μs. There is also a slight peak around m/z = 207 beginning around 500 μs which appears to correlate with the main peak of hexamethylcyclotrisiloxane. A full list of the observed mass peaks and the time of their initial appearance is provided in Table B.6b of the Appendix.

3.3 HRRST TOF-MS Results

In the ALS experiments, the same temperature and pressure conditions were explored using multiple ionization energies. For each condition and ionization energy, the same shock conditions were repeated 100 times at a frequency of 1 Hz, and the resulting mass spectra were arithmetically averaged improve the signal-to-noise and increase the resolution of small features. The resulting data create a three dimensional space in which the mass spectra can be analyzed as a function of reaction time and ionization energies.

3.3.1 HMDSO TOF-MS Results (HRRST)

Representative results for the thermal decomposition of HMDSO in the HRRST experiments are presented here. In depth analysis is provided for two complimentary experimental sets from the comprehensive sets explored in this overall study. Figure 3.23 shows representative mass spectra in the reaction time domain at four distinct times for 0.6% HMDSO in argon at 1580 K and 12.2 atm. The figures take into account all battalions, i.e. include spectra for all EI ranges at the same state conditions. Figure 3.24 shows representative mass spectra results the ionization energy domain at 12 eV for the same experiments. The resulting mass spectra is derived from all reaction times in each of the battalions.

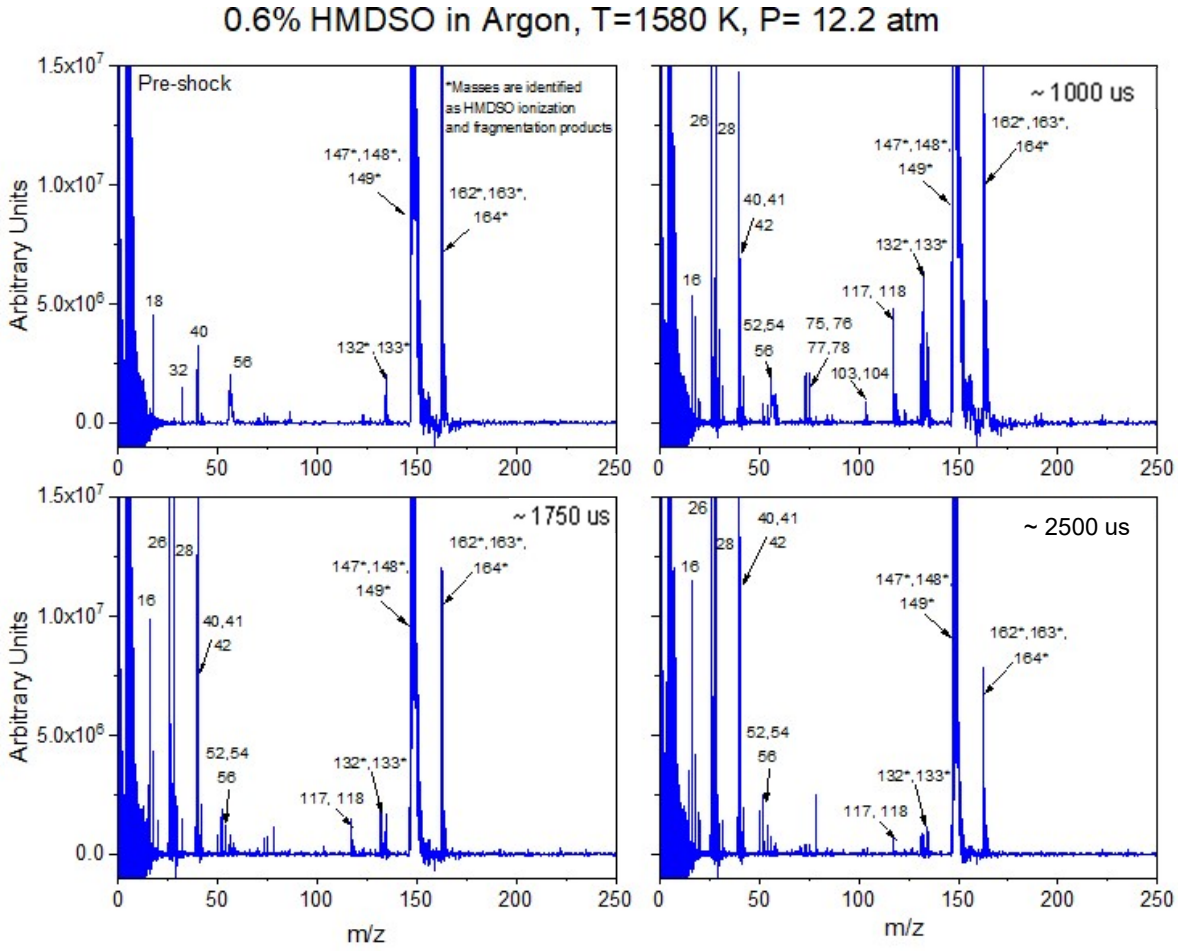

Figure 3.23: Average mass spectra representing ionization energies of EI = 12 to 7.75 eV from 1800 experiments of 0.6 % HMDSO in 99.4% Ar at 1580 K and 9300 Torr (12.2 atm). Four representative reaction times are shown: Pre-shock, 100 μs post-shock, 175 μs post-shock, 250 μs post-shock.

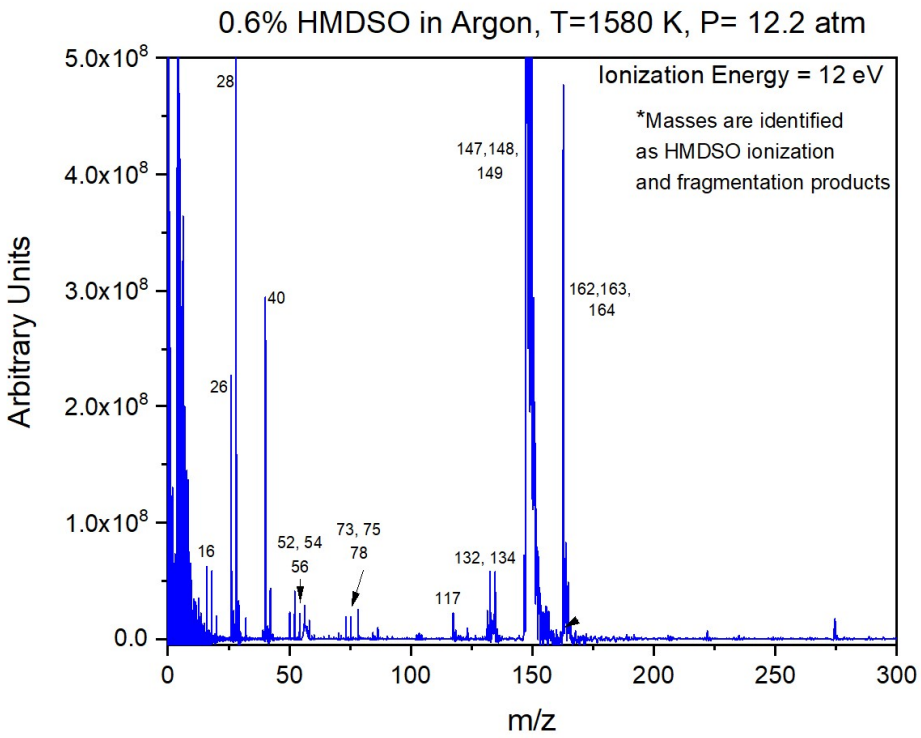

Figure 3.24: Average mass spectra from Figure 3.25 forEI = 12 eV from 100 experiments and all reaction times with 300 spectra per shockwave experiment for a total of 30000 mass spectra.

There are three mass species in the pre-shock data that cannot be attributed to the fragmentation of HMDSO: m/z = 18, 32, and 40. The features at m/z = 18 and 32 are attributed to trace amounts of air present in the vacuum chamber with 18 being water and 32 being O_2. The feature at m/z = 40 is most likely argon. As seen with the DFST experiments, there are significant concentrations of smaller organic species, but limited indications of higher mass species. A full list of the observed mass peaks with the time of their initial appearance and energies is provided in Table B.7b of the Appendix. The mass peak observed around m/z = 274 was observed in all mass spectra at the same relative peak height in all the HMDSO experiments, and it is attributed to noise in the system.

Further experiments were carried out at the same temperature and pressure conditions, but with the MgF_2 window in place. The use of the MgF_2 window limits the transmission of higher harmonic light so any higher harmonic light transmitted through the gas filter is then absorbed by

the MgF_2 window, increasing confidence in the observed ionization energy determinations. However, the MgF_2 window reduces the signal strength of the transmitted light and limits spectra to observations for EI values below 10.8 eV. Figure 3.25 shows the resulting mass spectra.

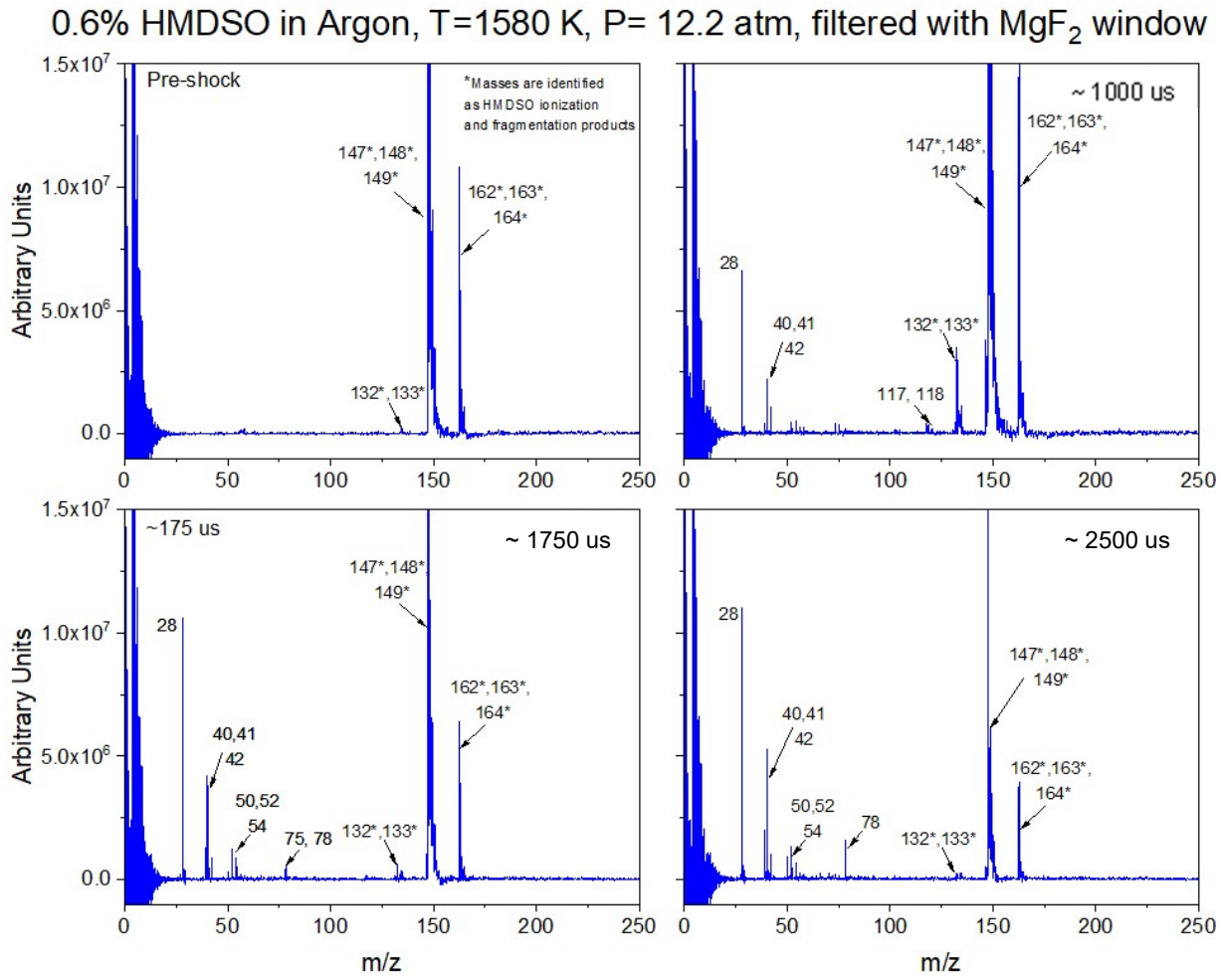

Figure 3.25: Average mass spectra representing ionization energies of EI = 10.75 to 7.75 eV from 1000 experiments of 0.6 % HMDSO in 99.4% Ar at 1580 K and 9300 Torr (12.2 atm). Four representative reaction times are shown: Pre-shock, 100 μs post-shock, 175 μs post-shock, 250 μs post-shock.

The MgF_2 window filters the mass peaks associated with the presence of low concentrations of air in the vacuum chamber and the signature from the inert bath gas so the m/z = 18, 32, and 40 peaks seen in the Pre-shock region of the experiments (see Figure 3.24). Again, as seen with the DFST experiments, there are significant concentrations of smaller organic species, but no

higher mass species. A full list of observed features and the times of their initial appearance is provided in Table B.7b of the Appendix.

3.3.2 TMSO TOF-MS Results (HRRST)

Representative results for the thermal decomposition of TMSO in the HRRST experiments are presented here. In depth analysis is provided for two complimentary experimental sets which are also complimentary to the HMDSO experimental sets described in Section 3.3.1. Figure 3.26 shows representative results at four distinct times for 0.6% TMSO in Ar at 1580 K and 12.0 atm. The mass spectra are derived from all the ionization energies explored in the experiments. Figure 3.27 shows representative data from EI = 12 eV for the same experimental results presented in Figure 3.26.

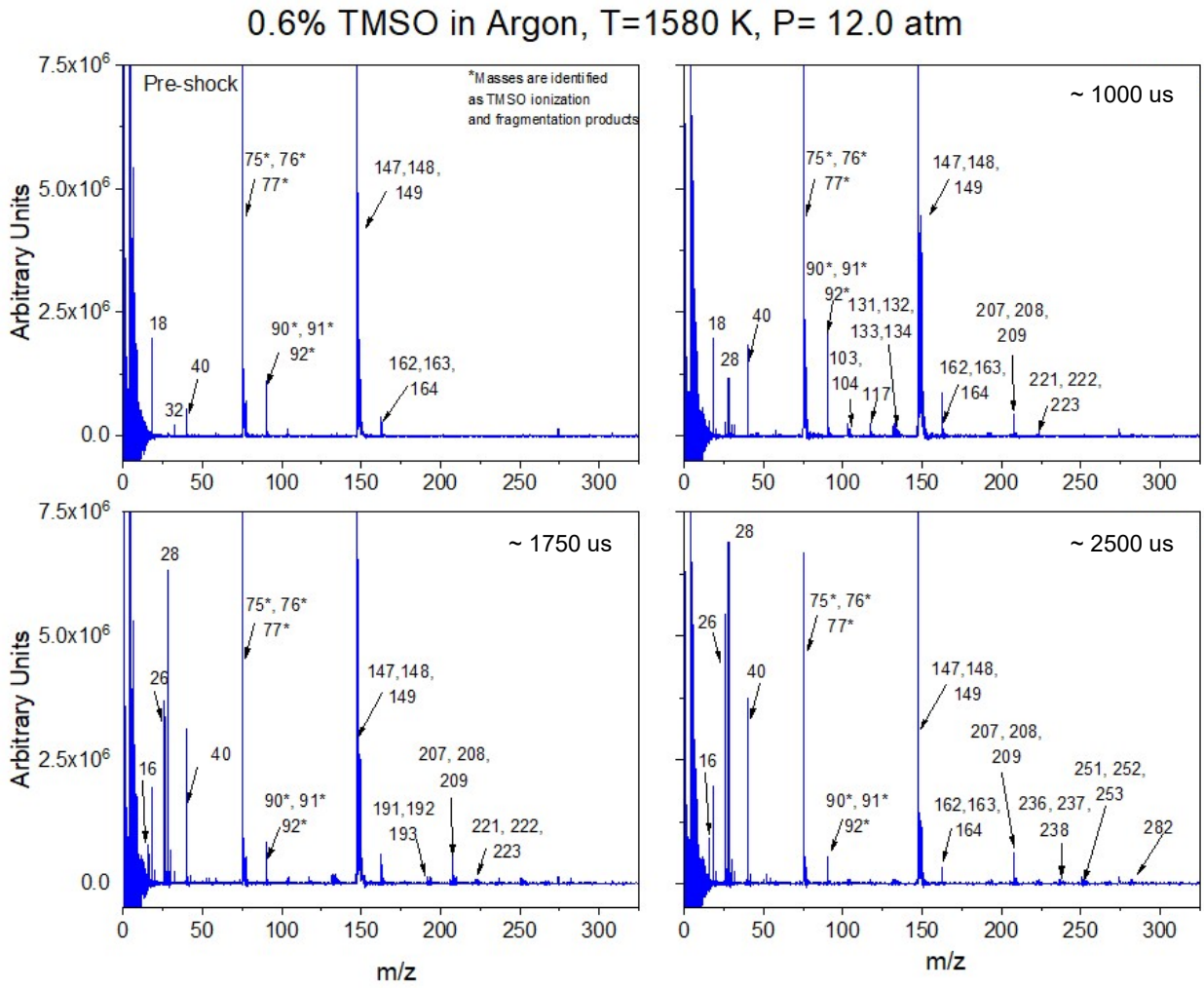

Figure 3.26: Average mass spectra representing ionization energies of EI = 12 to 7.75 eV from 1800 experiments of 0.6 % TMSO in 99.4% Ar at 1580 K and 9100 Torr (12.0 atm). Four representative reaction times are shown: Pre-shock, 100 μs post-shock, 175 μs post-shock, 250 μs post-shock.

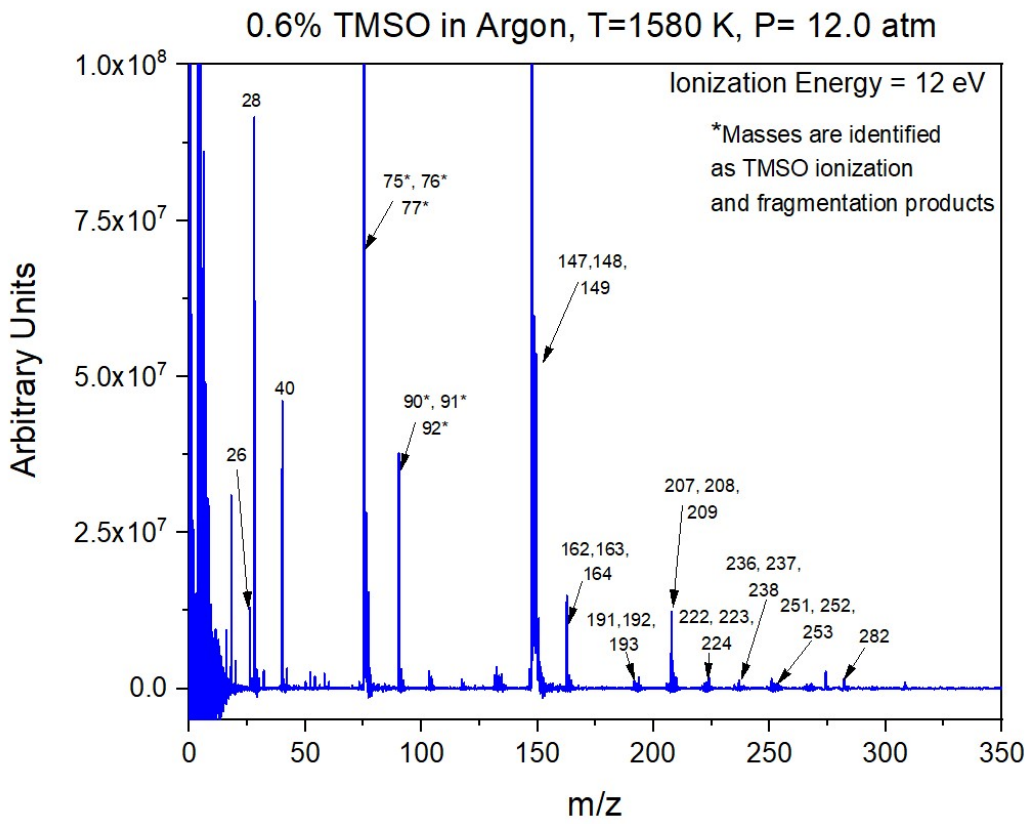

Figure 3.27: Mass spectra for 12 eV averaged across 100 shocks and all reaction times (300 spectra per shock) for a total sum average across 30000 mass spectra for the same experiments shown in Figure 3.26.

There are multiple features that cannot be attributed to the fragmentation of TMSO in the pre-shock region: m/z = 18, 32, 40, 147, 148, 149, 162, 163, and 164. The m/z = 18 and 32 peaks can again be attributed to water and O_2 due to small amounts of air in the vacuum chamber. The mass m/z = 40 is most likely argon. The clusters beginning at m/z = 147 and 162 are attributed to low levels of HMDSO present in the TMSO sample. Through analysis of two separate samples of TMSO obtained from Sigma Aldrich, the presence of trace amounts of HMDSO in the source TMSO was confirmed. Cross contamination between experiments is not the cause of the observations. As the highest available purity is guaranteed to 97.5%, a small amount of contamination is expected. While this assures a relatively small concentration of any species in addition to TMSO, the HMDSO still appears as a significant feature in the mass spectra due to

the strength of the signal generated by the ionized species. The strong signal relative to other peaks in the system does not indicate relatively high concentrations of HMDSO, just that HMDSO is strongly ionized. The mass peak around m/z = 274 was again observed in all mass spectra at the same peak height, and is therefore attributed to noise in the system.

As seen in the DFST results, there are significant smaller organic species present in the HRRST mass spectra results. However, there are also notable higher mass peaks observed beyond the mass of TMSO. Of particular note are the higher mass peak clusters around m/z = 191, 207, 222, 236, 251, 266, and 282 which are mostly absent from the DFST experiments. A full list of thee observed mass peaks with the time of their initial appearance and energies is provided in Table B.4 in the Appendix.

Further experiments were carried out at the same temperature and pressure conditions, but with the MgF_2 window in place. Figure 3.28 shows the resulting mass spectra.

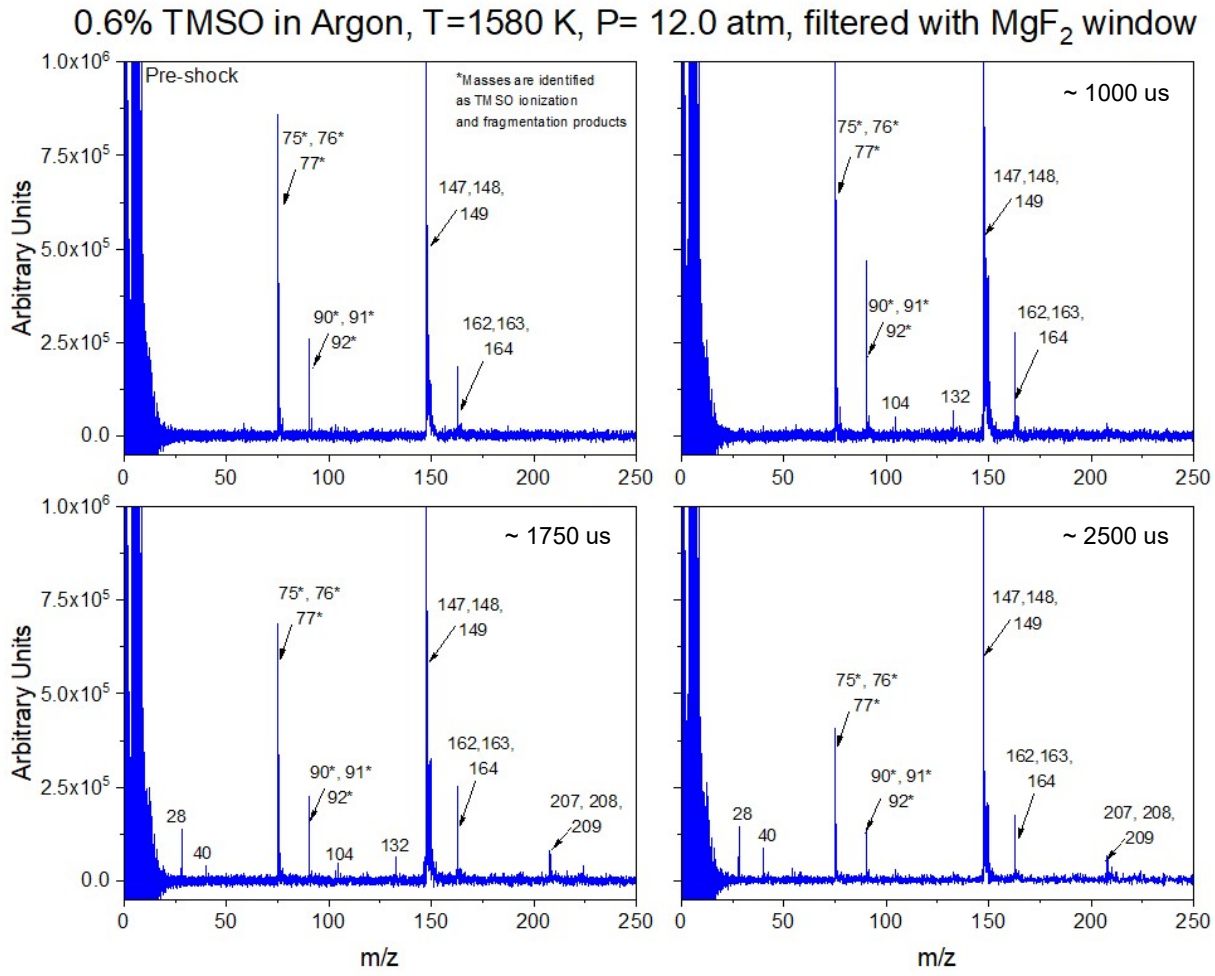

Figure 3.28: Average mass spectra representing ionization energies of EI = 10.75 to 7.75 eV from 1000 experiments of 0.6 % TMSO in 99.4% Ar at 1580 K and 9100 Torr (12.0 atm). Four representative reaction times are shown: Pre-shock, 100 μs post-shock, 175 μs post-shock, 250 μs post-shock

4. Discussion

4.1 Laser Schlieren Observations

Laser schlieren is a technique which is highly suited for determining elementary reaction rates and proposing reactant pathways. However, little is known about the thermochemical properties and reaction pathways for siloxanes and there are limited correlations that can be drawn between these compounds and those which have been studied previously. Potential decomposition pathways for HMDSO were identified through the calculations described in Chapter 2, but these are incomplete and do not capture the full behavior observed in the

experimental studies. Further analysis is necessary before the LS signals can be modeled with a reaction mechanism, but the behavior observed in these experiments is still helpful in understanding the reaction behaviors of these compounds.

For each species and condition, the density gradients are positive. This indicates that endothermic reactions dominate the system response. This is not to say that there are only endothermic reactions in these systems, but that the overall response of the system is endothermic. This further supports the idea that radical recombination is not a key driver for these reaction systems, as radical-radical reactions tend to be strongly exothermic and the system response would exhibit negative density gradients if these reactions were dominant.

Motivations for the thermal decomposition study initially grew from the desire to develop a better understanding of the oxidation kinetics and fuel interaction behaviors of the siloxanes. However, the decomposition experiments have shown that, on the time scales relevant to this study, the siloxanes do not begin to decompose until significantly above the temperatures explored in the syngas auto-ignition study. Also of note from the auto-ignition study is the strong increase in energy release related to the addition of the siloxane species (i.e., the higher rates of pressure rise). If strongly endothermic thermal decomposition reactions were active, the increase in energy release would not be as significant as the 20% increase in post-ignition pressure measured in the auto-ignition experiments.

The proposed initial thermal decomposition reactions are shown in Figures 3.29 (HMDSO) and 3.30 (TMSO). At this time, attempts to model the LS profiles using these reaction schemes do not capture the experimental behavior, indicating that further reactions are involved.

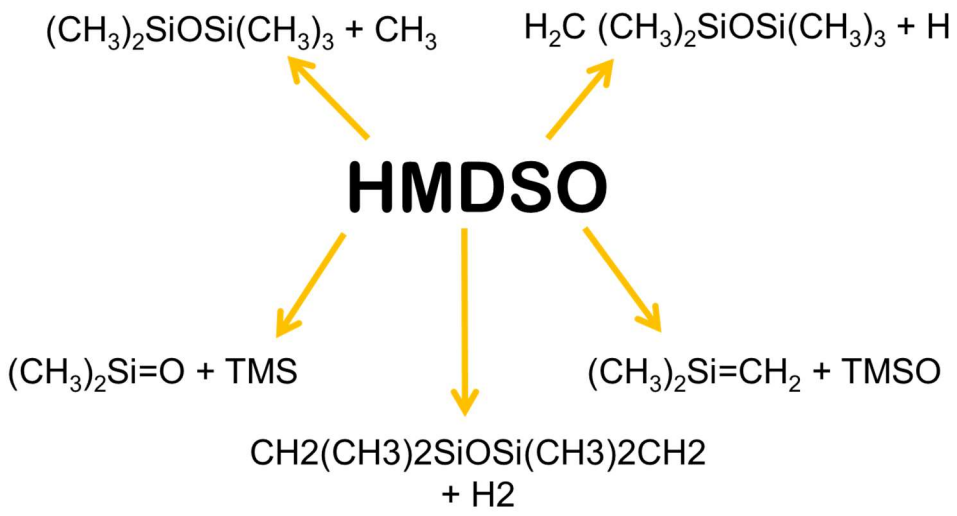

Figure 3.29: Proposed reaction pathways for thermal decomposition of HMDSO. The radical producing channels identified have relatively high energy barriers and as such are only relevant at high temperatures.

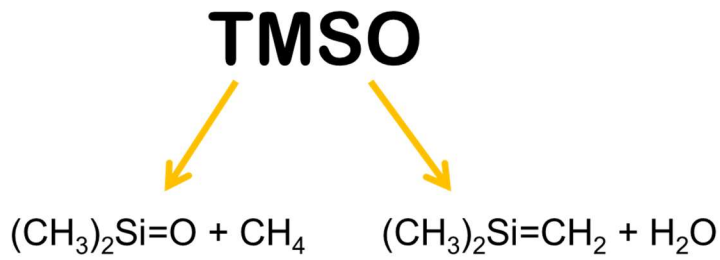

Figure 3.30 Proposed reaction pathways for thermal decomposition of TMSO.

4.2 Pyrolysis Products Identified through TOF-MS

While the ALS provides highly tunable ionization energy, the electron impact setups at ANL allow for the observation of relevant hydrocarbon species which are not observed with the lower ionization energy experiments conducted at the ALS. The filtering of higher ionization energy species is helpful for blocking signals from the inert bath gas which may reveal additional species. However, this also filters some relevant species which have higher ionization energies, such as hydrogen. From the DFST-TOF MS experiments, the production of acetylene and hydrogen are apparent, but both of these compounds have higher ionization energies than are accessible in the configuration currently preferred at the ALS with the argon gas filter in place. Conversely, more species overall appear in the mass spectra collected from the experiments

conducted at the ALS. Some of the differences in observed species may be attributed to the different conditions explored by the two experimental devices. Additionally significantly more shocks were averaged using the HRRST which allowed smaller mass peaks to become more apparent even with the weaker signal per-shock resulting from the ALS. Further insights into the species identification based upon the resulting mass peaks is possible through analyzing the appearance energies of the various peaks and changes in the peak clusters as the ionization energy is varied, which is discussed in the next section.

4.2.1 HMDSO Pyrolysis Products Identified through TOF-MS

Resulting mass spectra from both types of shocktube experiments highlight that the proposed decomposition models (both those proposed here and those proposed in literature) do not include all relevant species and reactions. However, part of this discrepancy may be due to a strong influence from secondary reactions. The initial reaction steps presented in Figure 3.29 for HMDSO show the two main pathways result in the production of highly reactive species, dimethylsilanone ($O=Si(CH_3)_2$) and 2-silasbutene ($H_2C=Si(CH_3)_2$). While currently neither of these species has been identified in the mass spectra collected for HMDSO, some of the organic species identified in these experiments are associated with the decomposition of both species, specifically CH_4, C_2H_2 and C_2H_4 [2,8] indicating their potential production. Due to their highly reactive nature, these species many not have long enough residence times to be detectable by the TOF-MS. While the organic fragments do not definitively confirm the two reaction pathways, the early appearance of H_2 in the HMDSO mass spectra supports the validity of the other direct molecular pathway identified, namely the productions of $CH_2(CH_3)_2SiOSi(CH_3)_2CH_2 + H_2$.

While there are few silicon-containing species easily identified in the mass spectra from the HMDSO experiments, there was notable accumulation of particles on the endwall nozzle of both

shocktubes after conducting experiments with each of the silicon compounds. Figure 3.31 shows the endwall nozzle after hundreds of repeated shocks with HMDSO.

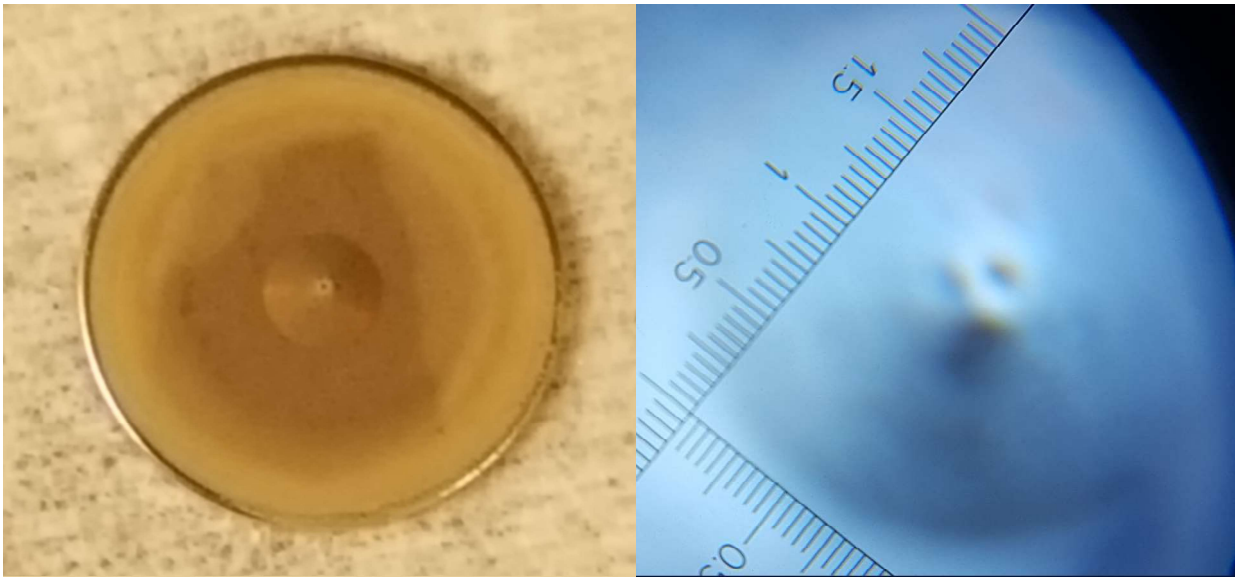

Figure 3.31: Images of the post-experiment endwall nozzle with material accumulation attributed to silicon species The left image highlights the sandy-colored nature of the deposition across the endwall while the right image is a microscopic view of the nozzle in the endwall showing the silicon-based particles blocking the opening and restricting gas flow. [Provided by Dr. Robert Tranter].

While it is known that these compounds will produce silica (SiO_2), the silicon to oxygen ratio of 2 to 1 in the siloxanes studied makes it impossible for all silicon atoms to be fully oxidized to SiO_2, SiO, or any Si_nO_n polymer chain.

One difficulty with identifying the relevant reaction compounds in the mass spectra is the challenge of differentiating between the mass peaks due to ionization fragments and mass peaks due to the unfragmented mass of an intermediate species. Understanding the common ionization patterns for these compounds makes it somewhat easier to identify the species which have strong mass peaks at masses lower than their atomic mass due to the propensity for fragmentation upon ionization. For many organic species, especially those relevant to common fuel chemistries, ionization energies are known for various fragmentations, but siloxanes have not been as well studied, making identification of intermediate species based upon ionization energy curves

impossible at this time. However, by analyzing the known fragmentation patterns common to siloxanes and comparison with known mass spectra for some silicon species, some species may be identified. In the case of the linear siloxanes, the strongest mass peak for most species appears to result from the ejection of a methyl group upon ionization. Additionally, a lower strength mass peak may appear at the molecular mass of the structure, and there is frequently a strong minor peak around 73 due to the presence of the trimethylsilyl fragment. When these three features are observed simultaneously, the peaks can be attributed to the siloxanes.

The strong signal from the HMDSO ionization poses some additional challenges when trying to identify intermediates. The strong HMDSO signal can saturate the detector making identification of slightly higher masses difficult, and the strong peaks may mask the presence of smaller concentrations of intermediate species. While the main peak for HMDSO is at m/z = 147 with a cluster of smaller peaks following (due to isotopes involved in the chemical structure), there is a notable peak around m/z = 146. Any additional peaks associated with a mass in that cluster, as would be expected for a silicon containing mass, would be obscured by the strong HMDSO peak in this m/s region.

Similar to the common pattern observed in fragmentation of the linear siloxanes/methyl loss during ionization, there may also be a cluster around m/z = 131 for HMDSO which is also along the known fragments from HMDSO ionization as shown in the main At higher m/z values, if the m/z = 146 feature is actually an ionization fragment from the HMDSO losing a methyl group, it would correlate with a parent mass of m/z = 161. If this were the true mass of a decomposition product, the reaction would be HMDSO = $(CH_3)_3SiOSi(CH_3)_2CH_2$ + H. While this is a proposed thermal decomposition pathway, the energy barrier identified in Chapter 2 (and illustrated in the

PES reproduced here in Figure 3.32) indicates this would not be an active channel at these conditions. Further, there are no clear signs of a mass peak at an m/z of 161.

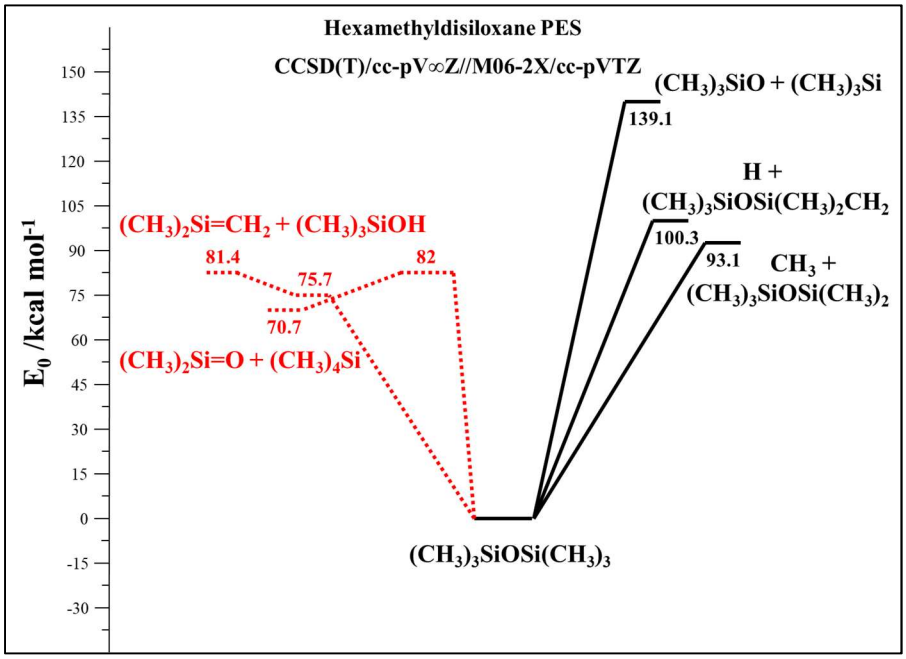

Figure 3.32: For discussion purposes, this is a reproduction of Figure 2.6. Potential energy surface for the decomposition of HMDSO [Provided by Dr. Raghu Sivaramakrishnan].

There is an m/z =15 peak identified in the DFST experiments which could be due to the presence of methyl radicals or as fragmentation product from the ionization of a larger species. As noted in the LS results, organic radical chemistry does not appear to be active in these systems. This does not rule out some production and consumption of methyl radicals, so this alone does not indicate that the mass peak is purely associated as a fragmentation product. However, some insight can be gleaned from the ALS results due to the variable ionization energies used. In Figure 3.23, there is an identifiable peak at m/z = 15.03, but that same peak is not present in Figure 3.25 which is the same experimental set, but with a smaller ionization energy range due to the use of the MgF_2 window. The methyl radical has a known ionization energy around 9.8 eV [7], so if this were the species producing the mass peak at m/z = 15 it should appear in both spectra. Further, as seen in the PES in Figure 3.32, the loss of a methyl

radical from HMDSO is not a favorable pathway at these conditions due to the high barrier height. Methane has major peaks at m/z = 15 and 16 with an ionization energy around 12.6 eV [7], which is above the ionization energy explored in this study, but due to the presence of water and argon mass peaks in the pre-shock region, it appears that some higher harmonic light is being transmitted potentially allowing these slightly higher ionization energy species to appear. This is a known phenomenon when working with the HVUV and is one of the reasons for conducting the MgF_2 experiments in addition to the experiments which only use the argon gas filter. For the reasons outlined here, both the m/z = 15 and 16 mass peaks identified in the DFST and HRRST experiments are most likely due to the presence of methane.

Based upon the analysis of the m/z = 146 peak behavior and the m/z = 15, 16 mass cluster, there is evidence of another direct molecular decomposition pathway for HMDSO which has not been previously identified in the proposed mechanisms: HMDSO = $C_5H_{14}Si_2O$ + CH_4. This can be the result of 1) a methyl group reacting with a hydrogen atom from the same side of the HMDSO to release methane and the product species $(CH_2)CH_3SiOSi(CH_3)_3$, which is a siloxane consisting of one trimethylsilyl group and a silicon atom with one methyl group and one methylene group or 2) the methyl and hydrogen can come from opposite sides of the HMDSO structure to produce the methane resulting in a tetramethyl cyclic species with a methylene bridge between the two silicon species opposite the Si-O-Si bond. Figure 3.33 shows these two possible species. Analysis of the thermochemistry and reaction energetics for these species can help validate these proposed reaction pathways. Based upon current understanding, the configuration containing the methylene bridge (compound 2 in Figure 3.33) appears more stable.

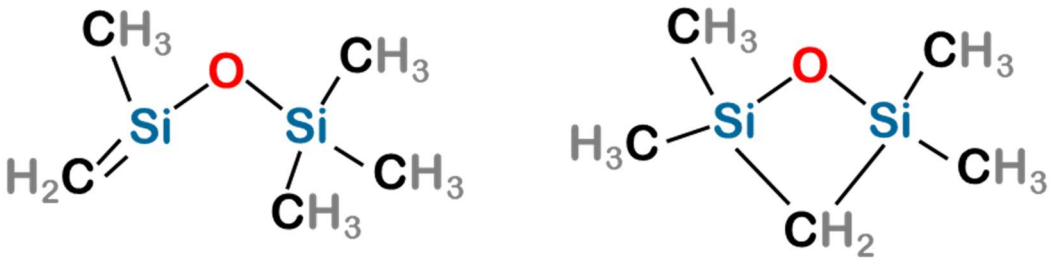

(1) (2)

Figure 3.33: Possible siloxane species resulting from a methane ejection from HMDSO. Compound 1 results from the methyl group bonding with a hydrogen from another methyl group on the same side of the HMDSO. Compound 2 results from the methyl group bonding with a hydrogen from the opposite side of the HMDSO.

While some literature predicts significant growth to larger siloxanes [1], the data presented here support the production of smaller organic compounds as highlighted by Almond et al. [8] for similar linear structures. However, notably absent from the mass spectra are any signs of ethane. Based upon the significant concentrations of methyl groups and the weakest bond in each structure being the Si-C bond, ethane ejection has been predicted in most prior studies. As there are still significant concentrations of silicon unaccounted for and notable deposits within the shocktube, it is apparent that a robust reaction model should include condensed phase chemistry. Towards that goal, a thorough understanding of the initial gas-phase kinetics is necessary.

4.2.2 TMSO Pyrolysis Products Identified through TOF-MS

Though barely identifiable in the DFST TOF-MS experiments, the ALS experiments show trace concentrations of HMDSO within the unreacted TMSO. The presence of HMDSO was identified in all experiments, but the spectra are most clearly visible in the ALS data. The HMDSO is attributed as an impurity in the TMSO from Sigma Aldrich. However, due to the low concentrations in the TMSO, which is further diluted due to the low fuel percentage in the experimental mixture, decomposition of HMDSO is not believed to be contributing to the species identified in the post shock spectra. The lack of interference is further supported by the fact that the pure HMDSO experiments have stronger signals in the smaller organic species range and

almost no discernable higher m/z features, whereas the TMSO experiments show some influence from organic species and spectra correlating with higher m/z species.

While the HMDSO does not appear to contribute to the TMSO spectra via significant chemical reaction, the HMDSO does obfuscate potential species in the region of the mass spectra around the primary mass peaks of HMDSO. Through careful comparison of the cluster of peaks in the m/z = 147-158 range with the pre-shock mass spectra collected for HMDSO in the same m/z range, it is apparent that there is another feature resulting from the decomposition of TMSO. The most notable behavior observed in this region is the growth of the m/z = 149 peak relative to the m/z = 147 and 148 peaks as reaction progresses. Figure 3.34 shows the region of interest for TMSO mass spectra as presented in Figure 3.26 and Figure 3.35 shows the same region for HMDSO mass spectra as presented in Figure 3.23.

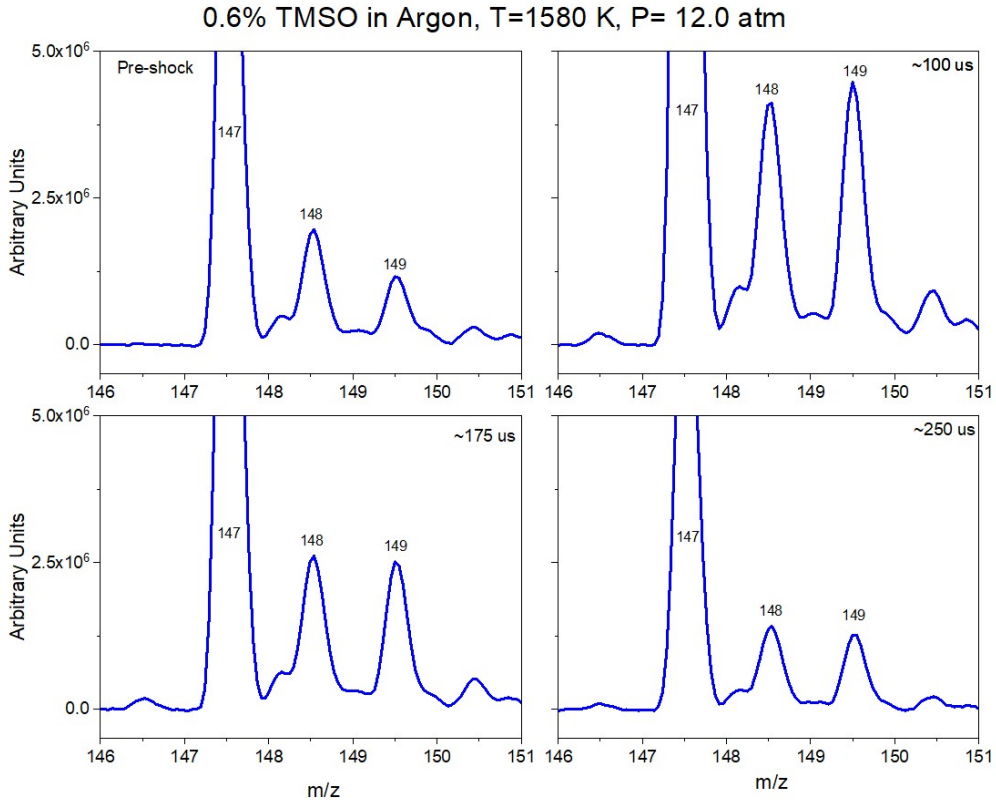

Figure 3.34 m/z range of 146-151 for the mass spectra presented in Figure 3.27 for the thermal decomposition of TMSO at 1580 K and 12 atm.

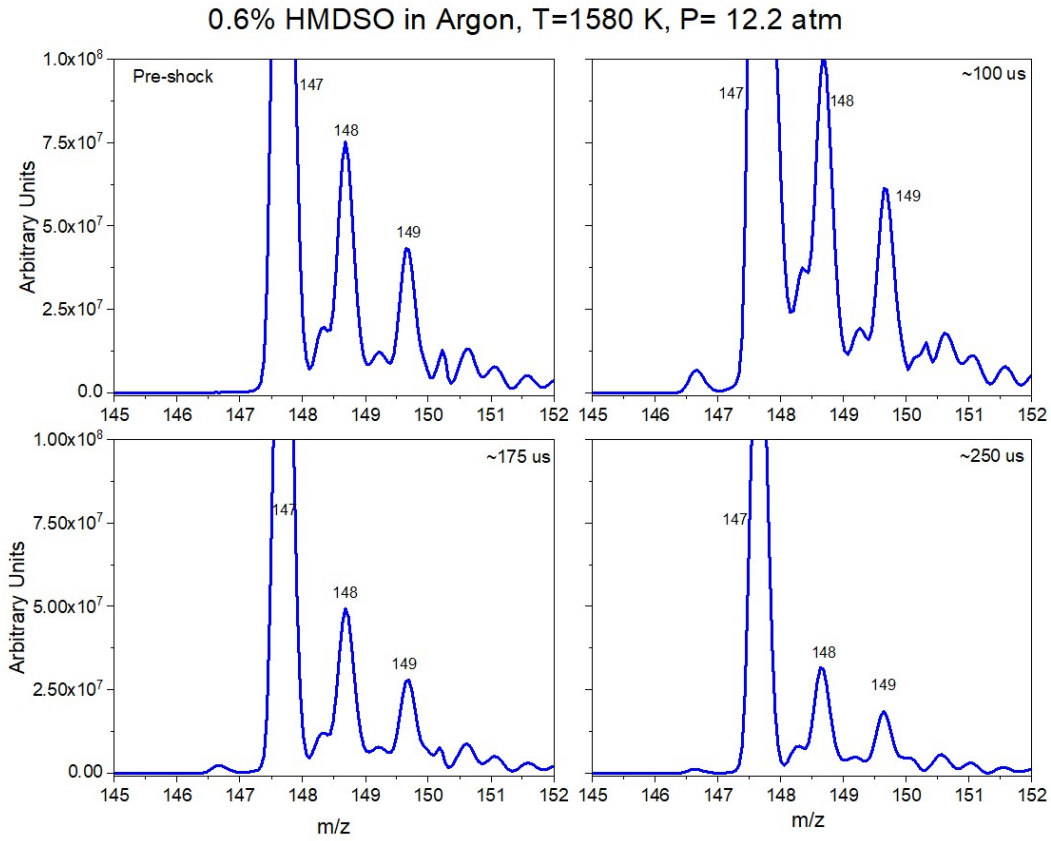

Figure 3.35 m/z range of 146-151 for the mass spectra presented in Figure 3.29 for the thermal decomposition of HMDSO at 1580K and 12.2 atm.

In the HMDSO experiments, the relative peak heights remain constant with m/z == 148 consistently having a significantly higher peak height than m/z = 149. However, the TMSO experiments show m/z = 149 increasing in intensity at a different rate as compared with m/z = 148 and even increasing beyond the m/z = 148 feature. This indicates another species is contributing to the mass m/z = 149 peak. Additionally, the lack of growth of the m/z = 148 peak indicates that dimethylcyclicsiloxane (D2 as labeled by Almond et al. $(CH_3)_4Si_2O_2$) is not being produced. While some studies predict this species as an intermediate, it is not a species that has been readily identified in any known systems. Further, prior work investigating chlorosiloxanes found that the production of the analogous cholorinated compound, $Cl_4Si_2O_2$, is not a favorable pathway and would be a highly exothermic insertion between two highly reactive

dimethylsilanones [9]. Similar to HMDSO, TMSO decomposition yields methane, ethylene, acetylene and hydrogen which are also identified as possible decomposition products of dimethylsilanone. However, these species appear to be present in lower concentrations and appear at later times. In the HMDSO case, hydrogen is one of the first species to appear whereas it first appears at a relatively later time for TMSO. This late appearance could indicate the hydrogen is actually the result of secondary chemistry in the case of TMSO, whereas it appears to be a primary product for HMDSO.

Unlike HMDSO, TMSO shows signs of thermal decomposition producing higher mass silicon species. There are multiple distinct clusters of three mass peaks at higher masses indicative of silicon containing species. Multiple insertions to larger ring structures appear to be more favorable and are supported by the observed mass spectra. Due to the structure of TMSO, it is more readily able to perform insertions than HMDSO. Silicon highly favors single oxygen bonds and with the HMDSO having the Si-O-Si central structure, it is less likely to break one of the Si-O bonds in favor of allowing an insertion. However, replacing the symmetric trimethylsilyl group with an H atom as in TMSO results in a weaker bond, which is accessible for insertion into a larger Si-O based structure. The direct route to dimethylsilanone also contributes a highly reactive species, which would find insertion into a larger Si-O-Si species favorable. Unlike carbon, which has highly stable doubled bonded structures, double bonded silicon structures are highly reactive except in the case of SiO_2. A mass peak with nominal mass m/z = 207 was identified in both the EI and PI experiments. With additional mass peaks also being identified around a nominal mass of m/z = 222, this is a strong indication that HMCTSO is produced with m/z = 207 being the main fragmentation ion and m/z = 222 representing the unfragmented parent. This is further supported by the noted growth of the m/z = 149 peak as

HMCTSO is identified as having a minor peak at this m/z value, as seen in Figure 3.8. It is also noted that there is a small peak at nominal mass m/z = 221 which would not correlate with HMCTSO. There is also a mass peak near a nominal mass of m/z = 236 with subsequent smaller trailing peaks, which could be the unfragemented parent to a daughter ion at m/z = 221. This species could be octamethyltrisiloxane. The insertion behavior of trimethylsilanol,s as well as the propensity for insertion of some of its predicted intermediate species, support the attribution of these features to HMCTSO and octamethyltrisiloxane.

Products from the pathways proposed for modeling the LS experiments do appear in the mass spectra collected in either the DFST or the HRRST experiments. The appearance of the m/z = 15 and 16 features indicate the presence of methane. As with the mass m/z = 15 peak identified in the HMDSO HRRST experiments, the mass m/z = 15 peak in the TMSO experiments is present only in the spectra acquired using the gas filter – notably not in the spectra acquired using the MgF_2 window. The coproduct identified for methane, dimethylsilanone (TMSO = CH_4 + $(CH_3)_2$=O), is not directly identified at this time, but some decomposition products of dimethylsilanone (C_2H_2, C_2H_4), as identified by Almond et al. [2,8], are present, as are those associated with the decomposition of 2-silasbutene which is a product in the second pathway (TMSO = H_2O + $(CH_3)_2Si=CH_2$). Further, while water is present in both the pre and post shock regions due to trace concentrations of air in the vacuum chamber, the peak appears to grow as reaction time progresses indicating possible water production through this pathway.

4.3 Towards Model Validation and Development

The TOF-MS experiments support the existence of the pathways identified in the initial models for the LS signals, but are unable to completely validate the observations from the LS experiments, and the pathways do not account for all species identified in the TOF-MS

experiments. Since a majority of the previous siloxane thermal decomposition data has focused on lower temperatures and longer reaction times, there is limited ability to extrapolate from prior studies to the state conditions studied in this work. These data are the first of their kind to develop higher temperature thermochemistry for siloxanes. However, there are still gaps in identifying intermediate species and end products. While the ionization energy determinations provide unique insights for determining the source of various mass peaks, there are not enough reference data on the ionization energetics for the siloxane species to apply the reference data as determinants at this time.

5. Conclusions

This study presented unique experimental measurements of the thermal decomposition of three organic silicon species: hexamethyldisiloxane, trimethylsilanol and hexamethylcyclotrisiloxane. While these results support the theoretical calculations presented in Chapter 2 showing that thermal decomposition is not accessible in low temperature combustion applications, the data are relevant to oxidation mechanism development, as they provide a foundation for validating thermochemical parameters of species of interest in oxidation studies. Furthermore, the results are the first on this class of compounds at conditions and time scales relevant to combustion. The LS results for TMSO and HMDSO provide the opportunity to investigate and validate existing thermochemical data in addition to providing valuable insights into the thermicity of the limiting reactions. The TOF-MS spectra provide the first speciation data for these compounds at high temperature conditions and highlight the appearance of compounds which had not been previously identified as key intermediates and pyrolysis products. While HMDSO has been predicted to produce larger linear and cyclic siloxanes, the major products identified in this study were smaller organics such as methane, ethylene, and

acetylene as well as hydrogen. No prior pyrolysis studies are known for TMSO, but this compound did display growth to larger siloxanes in addition to producing small organic species that has been predicted for other siloxane species. Focusing on the smaller organics, there is no identifiable production of ethane which is predicted by prior studies. These unique results are vital to further develop and validate kinetic models and thermochemistry. While this study focused on the gas phase kinetics, it is clear that condensed phase kinetics will be relevant to fully understanding the behavior of siloxane compounds.

6. Citations

[1] Chernyshev, E. A., Krasnova, T. L., Sergeev, A. P., Abramova, E. S. (1997) "Siloxanes as sources of silanones," Russian Chem. Bull. 46:1586-1589.

[2] Almond, M. J., Becerra, R., Bowes, S.J., Cannady, J.P, Ogeden, J.S., Walsh, R. A mechanistic study of cyclic siloxane pyrolyses at low pressures, *Phys. Chem. Chem. Phys.* 10 (2008) 6856-6861.

[3] Tranter, R.S., Giri, B.R. A diaphragmless shocktube for high temperature kinetic studies *Rev. Sci. Instrum*. 79 (2008).

[4] Randazzo, J.B., Tranter, R.S. Note: An improved driver section for a diaphragmless shock tube. *Rev. Sci. Instrum.* 86(1) (2015).

[5] Tranter, R.S., Lynch, P.T., A miniature high repetition rate shock tube. *Rev Sci Instrum*. 84 (2013).

[6] Kiefer, J.H. The Laser Schlieren Technique in Shock Tube Kinetics, *Shock Waves in Chemistry* (1981) 219-277.

[7] *NIST Chemistry WebBook, NIST Standard Reference Database Number 69*, Eds. P.J. Linstrom and W.G. Mallard.

[8] Almond, M. J., Becerra, R., Bowes, S.J., Cannady, J.P, Ogeden, J.S., Young, N.A., Walsh, R., A mechanistic study of the low pressure pyrolysis of linear siloxanes, *Phys. Chem. Chem. Phys.* 11 (2009) 9259–9267.

[9] Kiefer, J.H, Sivaramakrishnan, R. *On the chemistry of fumed silica.* Chemical Engineering Departmental Seminar, University of Illinois at Chicago. 2007. Shared via personal communication with Dr. Robert Tranter and Dr. Raghu Sivaramakrishnan.

Chapter 4: Development of an Oxidation Mechanism for Siloxanes

Portions of this chapter appear in the paper Schwind, R.A. and Wooldridge, M.S, "Effects of Organic Silicon Compounds on Syngas Auto-ignition Behavior" *Combustion and Flame*, in press 2019, as well as the conference paper Schwind, R.A., Sivaramakrishnan, R., Wooldridge, M.S., Understanding siloxane combustion chemistry: computation and experimental studies of hexamethyldislioxane, *11th U.S. National Combustion Meeting*, Pasadena, CA. March 2019.

1. Introduction

Research into the reaction kinetics of siloxanes has been increasing due to their use as precursors for synthesizing silica products such as nano-particles and surface coatings [1]. However, there is still very little information available on the combustion of siloxanes. To date most studies involving the combustion of silicon-based species have focused on compounds and conditions relevant to chemical vapor deposition of silicon films and accelerants like silane (SiH_4). A detailed mechanism for SiH_4 combustion focusing on the $SiH_3 + O_2$ reaction by Miller et al. [2] noted the need to revisit existing silicon thermochemistry. Feroughi et al. [3] subsequently used portions of the detailed reaction mechanism from Miller et al. [2] in their study of the synthesis of silicon dioxide nanoparticles in a hydrogen/oxygen laminar premixed flame seeded with small amounts of HMDSO. A global reaction for HMDSO + OH was proposed, but the lack of detailed reaction kinetics were identified as a source of uncertainty and possible discrepancy between the model predictions and the experimental observations. Chernyshev et al. [4] studied low temperature pyrolysis of HMDSO as a source of silanones and provided possible reaction schemes for the thermal decomposition of HMDSO. The proposed reaction schemes included products consisting of both smaller silicon compounds and larger chain siloxanes. Few studies have explored the oxidation behavior of trimethylsilanol and there

are no known reaction kinetic studies for this compound. Mansfield and Wooldridge [5] first analyzed the impact of trimethylsilanol on syngas auto-ignition behavior. While possible reaction pathway effects were proposed, a detailed kinetic explanation was not found.

2. Methods

2.1 Simulations of Organic Radical Decompositions of HMDSO and TMSO

The experimental study discussed in Chapter 2 was complemented with computational simulations of the auto-ignition behavior of H_2 and CO mixtures in order to investigate the reaction chemistry being affected by the siloxane compounds. The simulations were conducted using the constant volume adiabatic zero-dimensional homogeneous reactor model in the ANSYS CHEMKIN software suite [6] with the Li et al. 2007 [7] chemical kinetic mechanism. The use of the Li et al. mechanism to simulate ignition delay time experiments of syngas mixtures using ANSYS CHEMKIN was previously demonstrated by Mansfield and Wooldridge [5]. Using the same approach, auto-ignition delay time predictions were calculated at 9.5 atm for four representative temperatures (1000 K, 1020 K, 1040 K, 1060) and four mixtures. The four simulation mixtures were chosen based on the test gas mixture compositions used in the experimental study and the silicon species structures. Since a comprehensive reaction mechanism is not currently available for siloxane and silanol species, the mixtures were made to determine what the impact would be from an instantaneous decomposition of the siloxane molecules to some of their basic fragments. Based on previous studies by Chernyshev et al. [4] and Almond et al. [8], larger linear siloxanes produce smaller silicon species, thus requiring the loss of some of the organic groups from the parent molecule. Additionally, the low pressure pyrolysis study of linear siloxanes by Almond et al. [8] showed the production of various hydrocarbons including CH_3 for siloxanes with similar structures to the HMDSO used in this

study. Therefore, the computational mixtures were: 1. a baseline mixture and 2. three additional mixtures with different radical species included in addition to the baseline species. A list of the compositions of the different mixtures is provided in Table 4.1.

Table 4.1. Mixtures considered in computational study for simulating instantaneous decomposition of 100 ppm siloxane species to organic radicals. All values are mole fractions.

Case	H_2	CO	Ar	N_2	O_2	CH_3	OH	H
1	0.012	0.028	0.035	0.723	0.202	--	--	--
2	0.012	0.028	0.035	0.722	0.202	--	--	0.0006
3	0.012	0.028	0.035	0.722	0.202	0.0006	--	--
4	0.012	0.028	0.035	0.723	0.202	0.0003	0.0001	

With simulation Case 1 representing of the baseline syngas experiments, Cases 2-4 represent the syngas mixture plus the organic constituents from the addition of 100 ppm of HMDSO or TMSO. Cases 2 and 3 are mixtures of the radicals from the decomposition of HMDSO where Case 2 represents the instantaneous ejection of one hydrogen from each methyl group of the siloxane, and Case 3 represents the instantaneous ejection of the six methyl groups of the siloxane. Case 4 represents the decomposition of trimethylsilanol to the three methyl groups and the one hydroxyl group for each TMSO molecule.

2.2 Simulations of an Organic Analogue for HMDSO

Based upon the strong ignition promoting behavior observed in the RCF ignition studies [9], it was initially hypothesized that decomposition of the HMDSO into radical species was accelerating ignition. However, as shown through the potential energy surface analysis, the decomposition pathways of HMDSO to radical species have high energy barriers, making these pathways inaccessible at the conditions explored in the auto-ignition studies. For this reason, simulating these effects through decomposition to the basic organic radicals is not a proper analog. Although the direct molecular channels which produce highly reactive compounds have lower energy barriers than the bond fission channels, these are still inaccessible at the conditions

of the auto-ignition experiments. Additionally, the thermal decomposition experiments presented in Chapter 3 show that neither HMDSO nor TMSO pyrolyze until temperatures above 1300 K. This indicates HMDSO and TMSO consumption in the ignition experiments is started through different mechanisms than direct decomposition.

In order to explore the interactions of the initial radicals from the ignition of the H_2/CO base fuel with HMDSO, computational experiments were seeded with a well-studied organic molecule with similar structure, dimethyl ether. Larger analogues for the hexamethyldisiloxane structure were considered in order to match the energy content, but the direct structural analogue, ditertbutyl ether, has no known mechanism, and both methyl-tertbutyl ether and ethyl-tertbutyl ether have direct decomposition channels which are accessible at the experimental conditions, so they are not considered good surrogates.

A computational study of the auto-ignition behavior of representative H_2 and CO mixtures in a constant volume chamber was performed. The simulations were conducted using the constant volume adiabatic zero-dimensional homogeneous-reactor model in the ANSYS CHEMKIN software suite [6] with the Lawrence Livermore mechanism for dimethyl ether [10]. The mechanism contained 81 species and 377 gas phase reactions. Auto-ignition delay time predictions were calculated at 10 atm for three representative temperatures (1020 K, 1035 K, and 1050 K) and two mixture compositions. The mixture compositions were chosen to be complimentary to the HMDSO/syngas auto-ignition studies. The two mixture compositions used for the simulations were pure H_2 and CO (with H_2:CO of 1:2.34) with fuel-to-oxidizer equivalence ratio of $\varphi = 0.1$ and air-dilute with N_2 (Case 5) and H_2 and CO mixture with fuel-to-oxidizer equivalence ratio of $\varphi = 0.1$ and air-dilute with N_2 plus 100 ppm DME (Case 6).

2.3 Propagation Products from HMDSO

As the calculations described in Chapter 2 illustrate, there are at least three chain propagating pathways accessible at the conditions of interest. Two of these paths produce a hydroxyl radical with a silicon oxirane species and one path produces a HO_2 radical and a cyclic species, as shown in the reaction pathways below in Figure 4.1

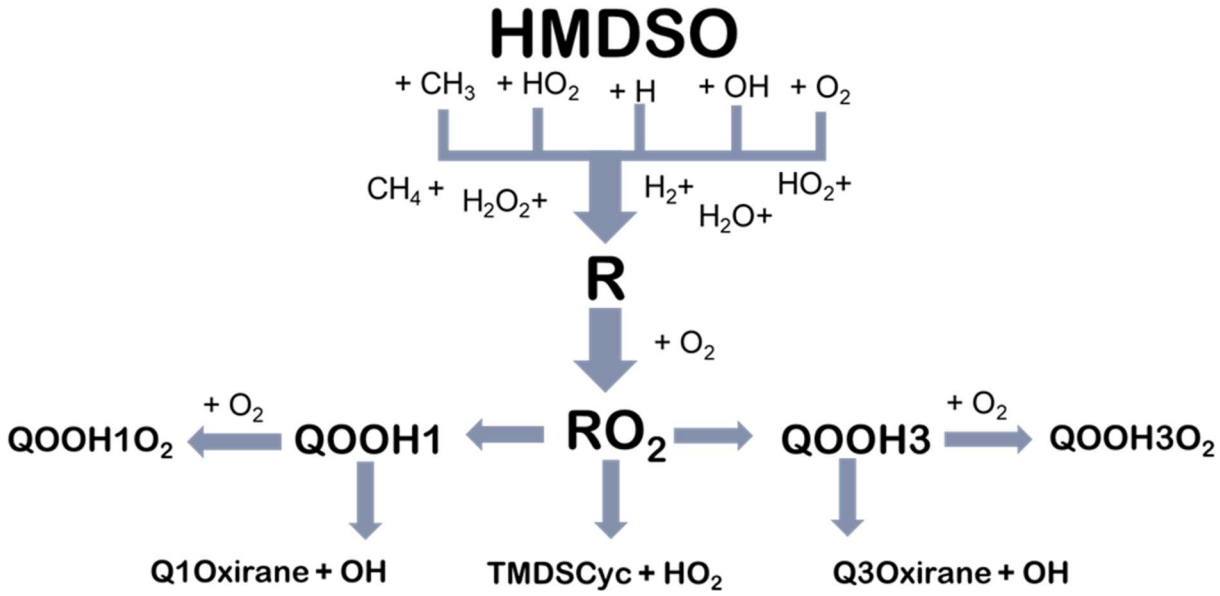

Figure 4.1: Hexamethyldisiloxane oxidation pathways (reproduced Figure 2.8).

Calculations are still on-going to fully define the reactions of HMDSO, but these initial pathways show possible routes to the increased reactivity observed in the auto-ignition experiments presented in Chapter 2. In order to explore these effects, mixtures representing the possible propagation routes from these three known channels were simulated using the same approach applied to represent the instantaneous decomposition of siloxanes to radicals. The simulations were also conducted using the constant volume adiabatic zero-dimensional homogeneous reactor model in the ANSYS CHEMKIN software suite [6] with the Li et al. 2007 [7] chemical kinetic mechanism. Auto-ignition delay time predictions were calculated at 9.5 atm for four representative temperatures (1000 K, 1020 K, 1040 K, 1060 K) and seven mixtures. The

seven mixtures were chosen based on the test gas mixture compositions used in the experimental study and the radicals generated through the three propagating channels identified by the energy surface calculations.

Table 4.2. Mixtures considered in the computational study for simulating HMDSO propagation pathways. All values are mole fractions and are based on an initial 100 ppm of HMDSO in the syngas base mixture.

Case	H_2	CO	Ar	N_2	O_2	HO_2	OH
1	0.012	0.028	0.035	0.723	0.202	--	--
7	0.012	0.028	0.035	0.722	0.202	--	0.0001
8	0.012	0.028	0.035	0.722	0.202	0.00002	0.00008
9	0.012	0.028	0.035	0.722	0.202	0.00003	0.00007
10	0.012	0.028	0.035	0.722	0.202	0.00005	0.00005
11	0.012	0.028	0.035	0.722	0.202	0.00008	0.00002
12	0.012	0.028	0.035	0.723	0.202	0.0001	--

Based upon the theoretical calculations, each HMDSO molecule can only follow one pathway and result in the production of a radical, either OH (via two different pathways) or HO_2. These proposed reaction pathways serve as the basis for Cases 7-12 where the initial 100 ppm concentration of HMDSO is split between OH and HO_2 radicals in various ratios representing a range of branching fractions.

3. Results

3.1 Radical Decomposition

Reactant mixtures for use in simulations were determined based upon the structure and concentration of the trace silicon compounds in the experimental mixtures and a syngas reaction mechanism [7] containing 21 species and 93 gas phase reactions was used to represent the H_2 and CO ignition chemistry. Predicted ignition delay times using initial mixtures of H_2, CO and the potential radicals from the siloxane compounds, omitting any silicon species, were evaluated at the temperatures and conditions of the experimental study. The weakest bond in the HMDSO structure is the carbon-silicon bond, followed by the carbon-hydrogen bond, and the strongest bond is the silicon-oxygen bond [11]. Looking solely at thermal decomposition based upon bond

energies, the most likely decomposition step for the HMDSO or the TMSO would be methyl loss. Based on this assumption, 600 ppm of CH_3 was used to represent instantaneous decomposition of 100 ppm of HMDSO to release all methyl groups. Similarly, 300 ppm of CH_3 and 100 ppm of OH was to represent instantaneous decomposition of 100 ppm of TMSO to release the methyl and hydroxyl groups. The release of H atoms represents an unlikely scenario of siloxane decomposition, but it was also considered in the computational study. Since this path was considered improbable, only 600 ppm of H was evaluated and not the total amount of H atoms available in either siloxane compound.

In order to understand if the changes in auto-ignition behavior could be attributed to the addition of these radicals, the pressure time history and ignition delay time for the four representative mixtures were studied using the CHEMKIN zero-dimensional homogeneous reactor model with constant volume and adiabatic constraints [6]. The overall ignition delay times in the simulations were defined as the time from the start of the simulation to the time of the second pressure inflection point or the second dP/dt maximum. Figure 4.2 shows the predicted ignition delay times for each condition, and Figure 4.3 shows the pressure time histories for the different mixtures at 1040 K. As expected, including radicals in the initial mixtures decreases the ignition delay time for each case which supports the hypothesis that rapid decomposition of the silicon compounds to form radicals can be the cause of the accelerated ignition. However, siloxanes as a rapid source of radicals is not sufficient to explain all the observed trends. The greatest impact was from the addition of 600 ppm H (which reduced the ignition delay time by approximately 50%), followed by the mixture with 300 ppm of CH_3 and 100 ppm of OH representing TMSO (which reduced ignition delay time by approximately 45%), and the 600 ppm CH_3 addition had the smallest impact representing HMDSO (with a decrease of

30%). However, the physical experiments, showed TMSO to have a comparable or slightly lower impact on ignition delay time compared with HMDSO. The computational study representing the more probable HMDSO decomposition fragments (Case 2, with 600 ppm CH_3) yielded a longer ignition delay when compared with the results of the study representing the TMSO fragments (Case 4, with 300 ppm CH_3 & 100 ppm OH). Additionally, none of the simulations showed a significant increase in dP/dt relative to the syngas base case as was observed with the HMDSO physical experiments.

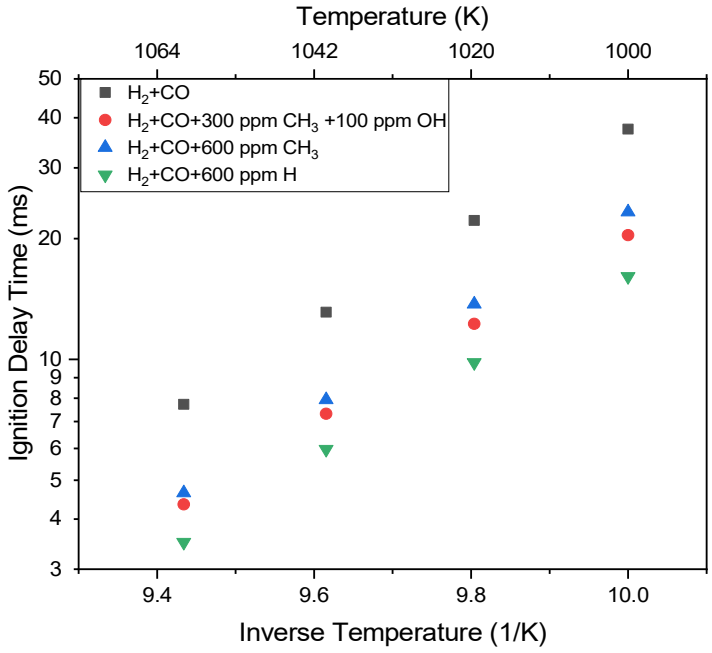

Figure 4.2: Effects of different initial mixture compositions on predicted ignition delay times for CO and H_2 at 9.5 atm.

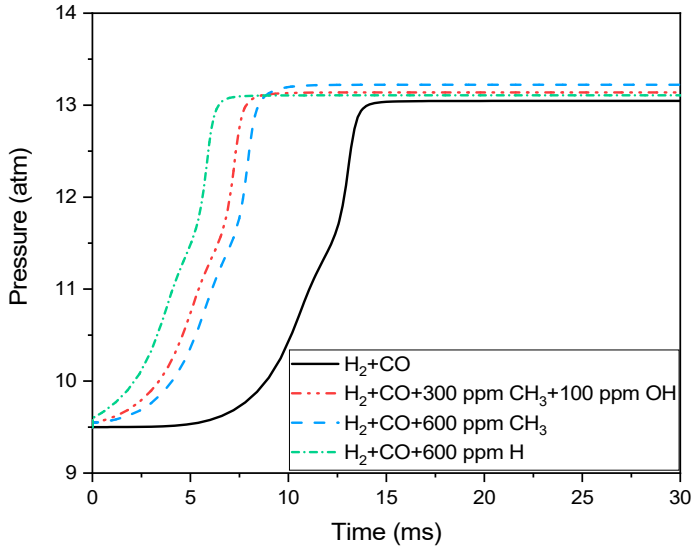

Figure 4.3: Effects of different initial mixture compositions on simulations of CO and H_2 ignition for an initial temperature of 1040 K.

3.2 Organic Analogues

Since the decomposition of HMDSO into radical species was found to be energetically inaccessible at the conditions relevant for the complimentary auto-ignition study, the computational experiments were designed in an effort to capture the potential chemistry involving R+O_2 reactions through the use of DME as a simple organic analog for the HMDSO. Figure 4.4 shows the predicted ignition delay time as a function of inverse temperature for the reference syngas mixture and the syngas mixture with 100 ppm DME.

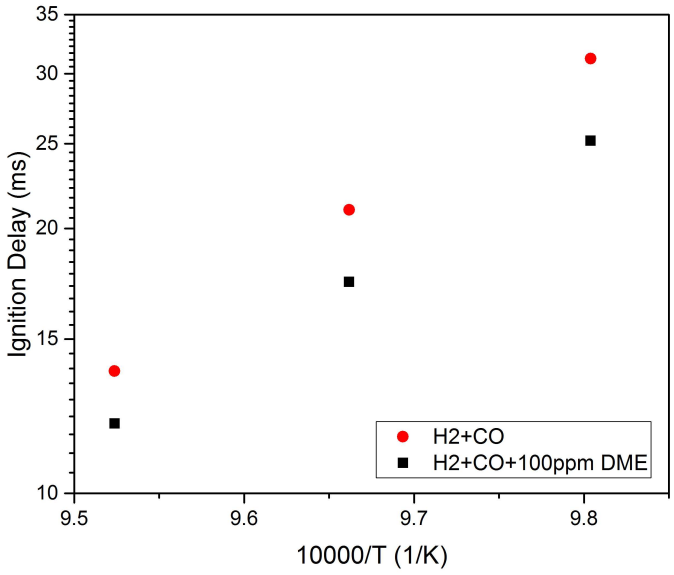

Figure 4.4: Predicted auto-ignition delay times for pure H_2 and CO, H_2 and CO +100 ppm DME at 10 atm with ϕ=0.1 and air dilute.

The addition of 100 ppm DME does have an ignition promoting effect through reducing ignition delay time by approximately 18%. While the DME follows the same trend as the HMDSO in reducing the ignition delay time, the impact is not nearly as significant as was observed in the physical HMDSO ignition experiments. Similarly, as shown in Figure 4.5, the addition of 100 ppm DME does not appear to have as significant an impact as HMDSO on the rate of pressure rise.

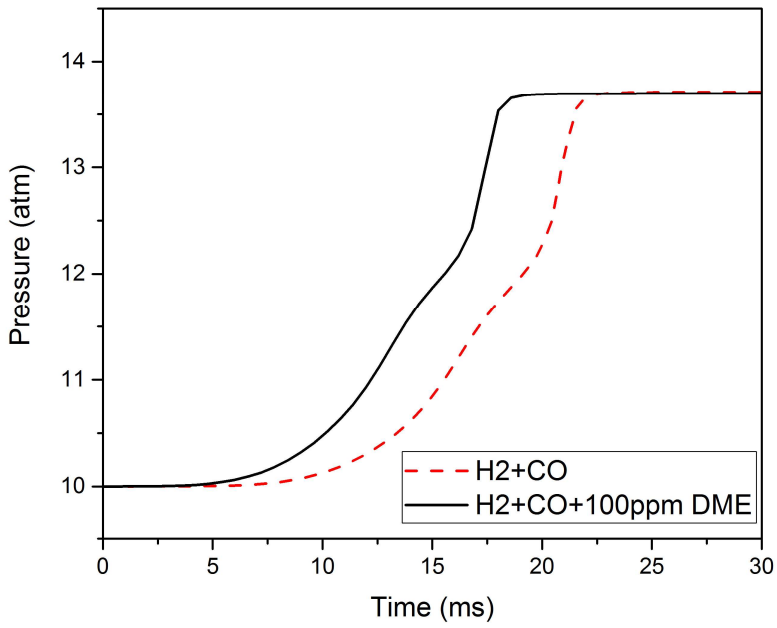

Figure 4.5: Predicted pressure-time histories for pure H_2 and CO, H_2 and CO +100 ppm DME at 10 atm, 1035 K with ϕ=0.1 and air dilute.

3.3 HMDSO Propagation Products

Figure 4.6 shows the predicted ignition delay times versus inverse temperature of the simulations of the HMDSO propagation reactions at 9.5 atm, and Figure 4.7 shows the simulation results for the pressure time histories for the baseline mixture and the two extreme branching limits: 100 ppm OH and 100 ppm HO_2 at 1040 K and 9.5 atm. As seen in the figures, the simulations results were nearly identical for all mixtures. The average percent decrease in ignition delay time for each mixture varied by less than 2% for all simulations and is reported in Table 4.3.

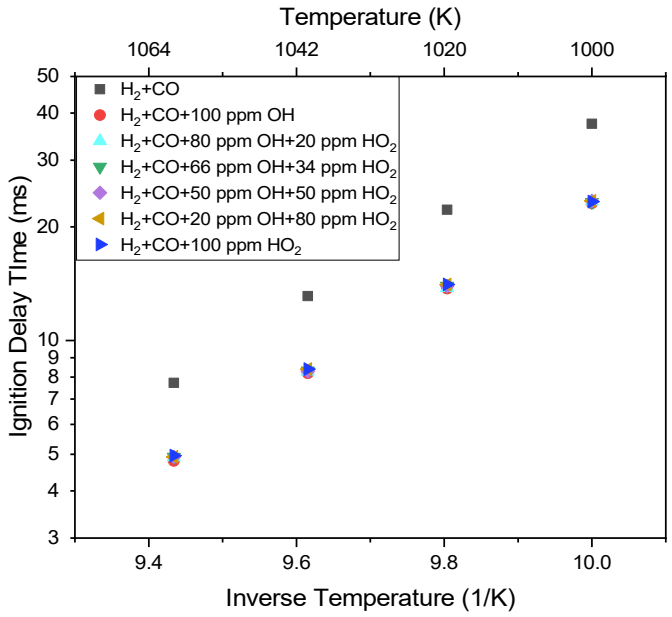

Figure 4.6: Effects of different initial mixture compositions on predicted ignition delay times for CO and H2.

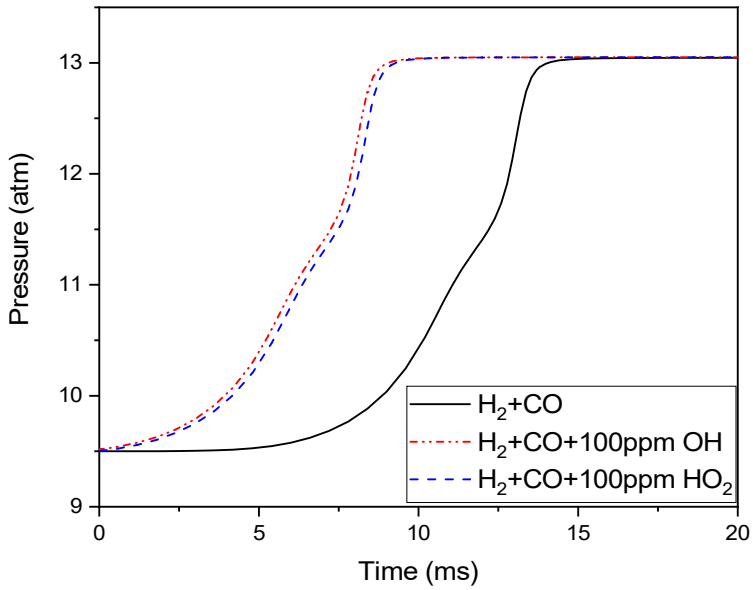

Figure 4.7: Effects of different initial mixture compositions on simulations of CO and H_2 ignition for an initial temperature of 1040 K.

Table 4.3. Average percent decrease in ignition delay time for each mixture relative to the baseline mixture

Case	HO_2 (ppm)	OH (ppm)	%decrease in τ_{ign}
1	--	--	--
7	--	100	38.0%
8	20	80	37.4%
9	34	66	37.0%
10	50	50	37.0%
11	80	20	36.6%
12	100	--	36.5%

4. Discussion

4.1 Radical Decomposition

While the simulations representing instantaneous decomposition of the siloxanes into radicals (see Figures 4.2 and 4.3) are a good starting point to understand how the structure of the silicon compounds may play a role on ignition behavior, they do not represent realistic decomposition rates and reactions of the silicon species. Due to the structure of the compounds, methyl loss would appear to be favored as the silicon-carbon bond is weaker than both the silicon-oxygen bond and the carbon-hydrogen bond. However, the presence of H is expected due to the observed production of H_2 and C_2H_4 in pyrolysis experiments [8], and the simulation results shown here indicate the methyl groups alone are not sufficient to cause the behavior observed in the experiments. While the addition of H atoms is closer to simulating the ignition promoting behavior seen with the addition of 100 ppm HMDSO, the instantaneous release of H atoms at the start of ignition is highly unrealistic especially at the relatively low temperatures studied in the RCF ignition experiments. Moreover, the energy required to break the bonds necessary to produce any of the radicals represented in these simulations is above the thermal energy available in the system at the state conditions studied. So, while the simulations indicate the siloxanes are most likely a rapid source of radicals causing the significant increase in reactivity

of the mixtures, instantaneous thermal decomposition to H, CH_3 or OH radicals is not the defining chemical characteristic of the siloxanes.

Additional insight may be gained through sensitivity and rate-of-production (ROP) analysis of the base H_2 and CO mixture. Results of sensitivity and ROP analyses for the syngas reference case are presented in Figure 4.8 for H_2 and in Figure 4.9 for CO, for T = 1040 K and P = 9.5 atm. The ROP results indicate H_2 is primarily consumed through the $H_2 + OH = H_2O + H$ reaction followed by the $O + H_2 = H + OH$ reaction. H_2 is most sensitive to the $H + O_2 (+M) = HO_2 (+M)$ and $H + O_2 = O + OH$ reactions. Figure 4.8 shows almost all of the carbon monoxide is consumed through the $CO + OH = CO_2 + H$ reaction, and CO is most sensitive to the same two $H + O_2$ reactions as identified in the H_2 sensitivity analysis. Comparison of Figures 4.7 and 4.8 show that H_2 is consumed in the first stage of ignition, and CO is consumed in the second stage. The results also indicate OH and HO_2 are critical to forming the radical pool which leads to ignition.

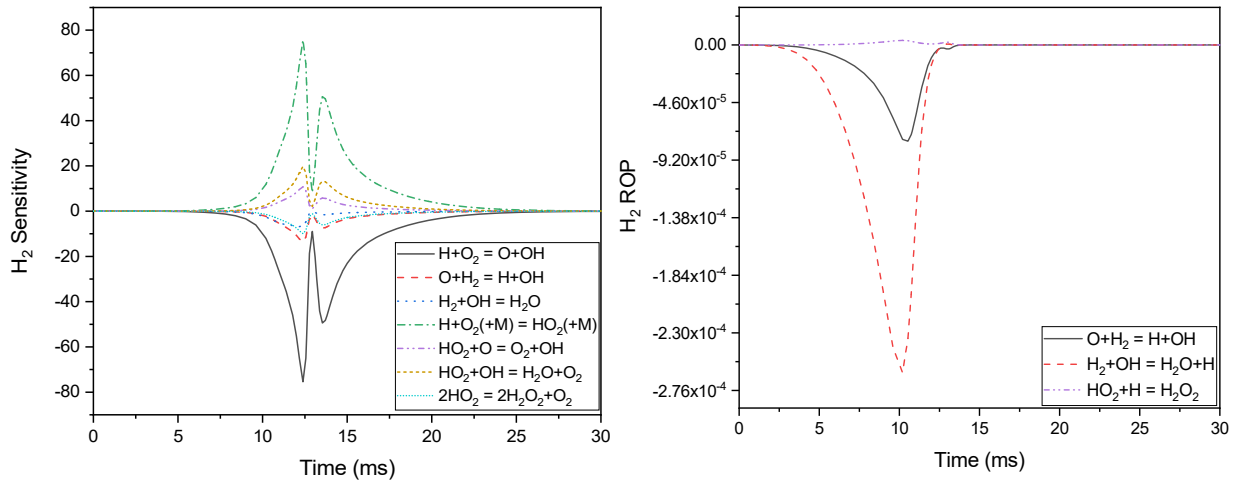

Figure 4.8: Sensitivity and rate of production results for H_2 for the baseline mixture of H_2 and CO at 1040 K and 9.5 atm (Case 1).

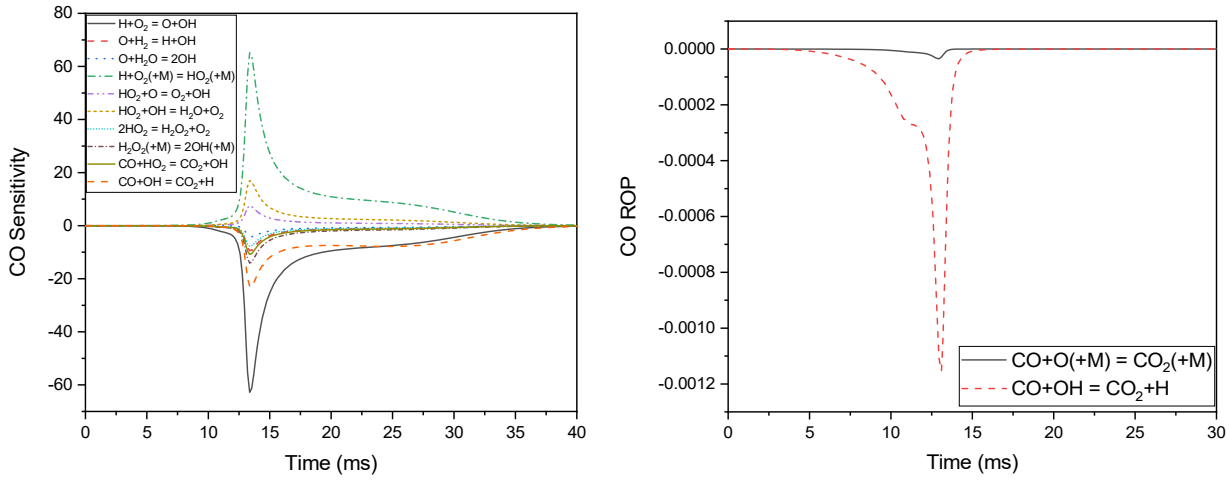

Figure 4.9: Sensitivity and rate of production results for CO for the baseline mixture of H_2 and CO at 1040 K and 9.5 atm (Case 1).

Mansfield and Wooldridge [5] proposed that the effects of TMSO on syngas ignition were due to reactions impacting HO_2 formation or consumption. It was hypothesized the addition of silicon-based species enhances the consumption of and/or disrupts the formation of HO_2 resulting in increased OH production. HO_2 must be impacted by the siloxane chemistry as the pressure dependence of the syngas ignition was affected by the addition of TMSO in Mansfield and Wooldridge [5] and HO_2 chemistry was attributed as the cause of the pressure dependence. Alternatively, the siloxanes could enhance OH production which could impact HO_2 through the reactions identified in the sensitivity analysis. The physical experiments in this work and those in Mansfield and Wooldridge [5] show both stages of ignition are affected by the addition of siloxanes. Since OH is the primary radical consuming CO, this may be an indication that enhanced OH production is connected with the siloxane reactions.

Based upon the experimental observations combined with the simulation results, it is proposed that reactivity is most likely initiated by radicals resulting from the combustion of the base syngas fuel, and the radicals then react with the trace siloxane compounds through chain

branching and propagating reactions which increase the radical pool and reactivity of the overall mixture.

4.2 Organic Analogue for HMDSO

The purpose of this computational study was to analyze the $R+O_2$ chemistry represented by the DME reaction pathways as an analog to HMDSO. Sensitivity analysis was performed for DME, and the three most significant reactions were $H+O_2(+M) = HO_2(+M)$, $H+O_2 = O +OH$ and $HO_2+OH = H_2O+O_2$. Not unexpectedly, the reactions are similar to those identified in the sensitivity analysis of the instantaneous-decomposition-to-radical simulations. The results of the ROP analysis for DME (Case 6) are presented in Figure 4.10, and show consumption of the DME is dominated by H-abstraction reactions leading to the radical CH_3OCH_2.

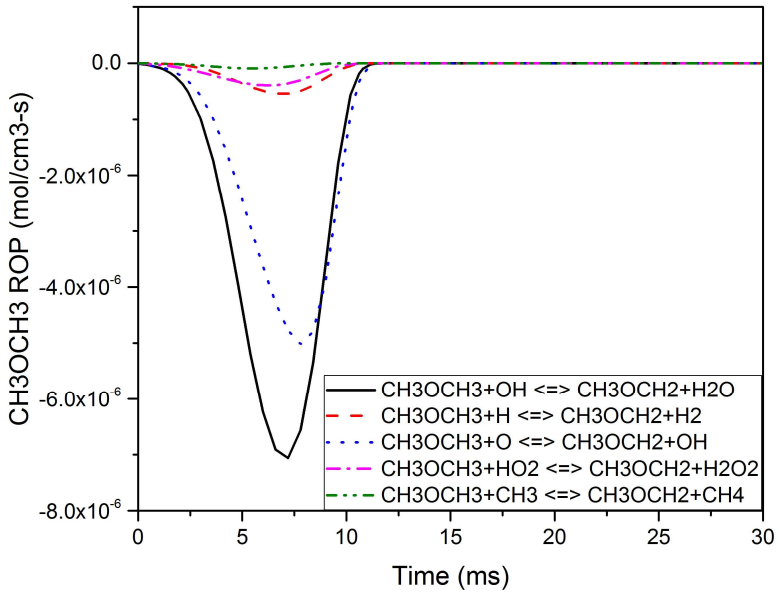

Figure 4.10: Predicted rate of production for 100 ppm of DME (CH_3OCH_3) in baseline syngas mixture for 1035 K and 10 atm (Case 6).

While direct decomposition channels were considered for DME, including bond fission and direct molecular channels, the results show none of the reactions were active. In addition to the consumption via H-abstraction by radical species, the ROP calculations also illustrate a relatively

low consumption of the DME by reaction with HO_2, and significant consumption by reaction with O atoms through a hydroxyl producing channel.

The DME ROP calculations show DME consumption is predominantly by interactions with radicals resulting from the initial reactions of the base syngas fuel to produce a radical species. ROP analysis was further conducted for the intermediate radical species CH_3OCH_2 to explore the impact of $R+O_2$ reaction chemistry. As shown in Figure 4.11, there are two main consumption pathways for the CH_3OCH_2 radical: an $R+O_2$ channel and a dissociation channel.

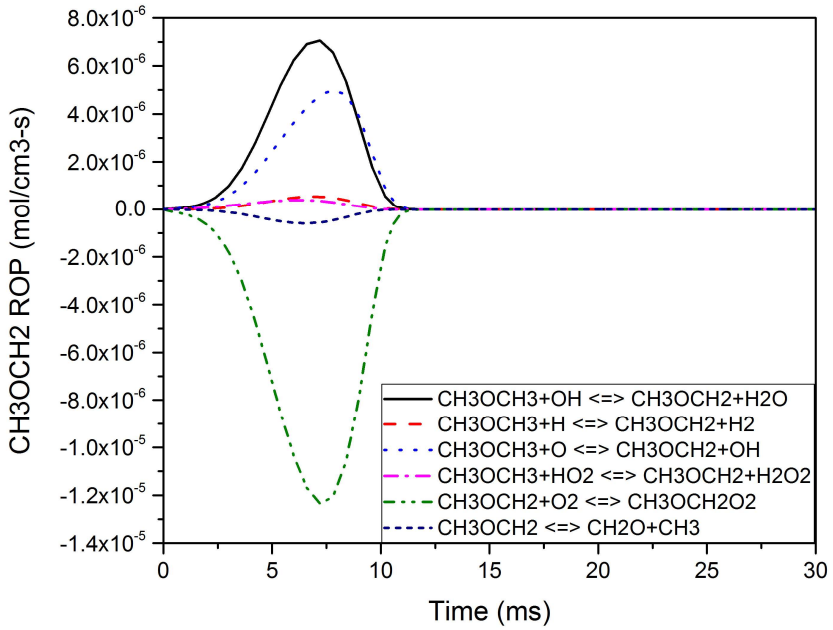

Figure 4.11: Predicted rate of production for CH_3OCH_2 for 1035 K at 10 atm.

Figure 4.10 shows CH_3OCH_2 radical production is through H-abstraction as opposed to bond fission. Figure 4.11 shows the main consumption of the CH_3OCH_2 radical is through the $R+O_2$ channel producing CH_3OCH_2OO. Further ROP analysis of the RO_2 product shows the major reaction consuming the CH_3OCH_2OO is a rearrangement to a QOOH species, CH_2OCH_2OOH. This species then dissociates to form a hydroxyl radical and formaldehyde. Figure 4.12 illustrates

the primary reaction pathways for the consumption of dimethyl ether in the H_2/CO combustion system.

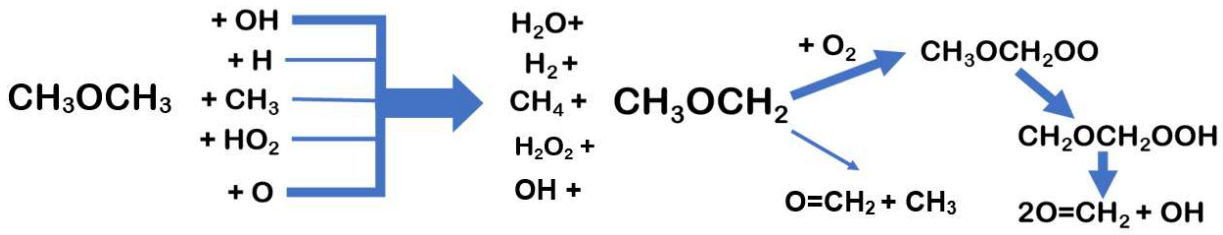

Figure 4.12: Main reaction pathways for the consumption of dimethyl ether in a doped H_2/CO system

While the addition of 100 ppm of dimethyl ether does not fully capture the ignition behavior observed of the addition of 100 ppm hexamethyldisiloxane to syngas, the sensitivity analysis and ROP analyses show potential for H-abstraction reactions to initiate reactions that will promote overall ignition, as opposed to thermal dissociation of the parent compound. The combustion of HMDSO at these conditions may follow similar pathways based upon the initial potential energy surface analysis. In addition, the larger and more complex HMDSO is likely to produce more radical channels, and thus more complex intermediate species than DME. Prior efforts to model silicon species like silanes using their complimentary organic structures (i.e., silane, SiH_4, compared with methane, CH_4) have shown some discrepancies with physical observations highlighting the different thermochemistry and reaction pathways between carbon and silicon species. These conclusions strongly motivate physical and computational studies of actual siloxane species and their intermediates instead of further pursuing organic analogues

4.3 HMDSO Propagation Channels

Based on the ROP analysis for DME, it appears likely H-atom abstraction from HMDSO to produce the first siloxane radical intermediate will be by an O or OH radical. After the RO_2 species is produced, there are three potential pathways that each lead to the production of at least

one radical species, a direct ejection of an HO_2 radical, and the formation of two separate QOOH species. Each of the QOOH species can lead to the production of an OH radical. Similar to the other simulations presented here, the predictions representing the $R+O_2$ pathways each promoted ignition, but none of the cases (Cases 7 – 12) demonstrated the magnitude of increase in reactivity observed in the physical auto-ignition experiments. Again, the instantaneous addition of the radicals is an unrealistic extreme, as radical production would require finite times – likely on the order of the characteristic time scales of ignition. The approach used to represent the $R+O_2$ reactions is also limited, as it treats the oxirane and cyclic species as inert and neglects additional pathways such as the continuation of the $QOOHO_2$ branching pathways.

As Mansfield and Wooldridge noted and further analysis here supports, OH and HO_2 chemistry control the behavior of the H_2/CO mixture with the likely reactions affected by the addition of siloxane species either increasing the production of OH and/or suppressing the production of HO_2. Each computational mixture studied here was chosen to probe potential branching ratios for the proposed HMDSO propagation routes. However, each of the seven radical seeding cases produced almost identical ignition delay times, with 100 ppm OH decreasing the ignition delay time by 38% and 100 ppm HO_2 decreasing the ignition delay time by 37%. The results show there is little sensitivity between the OH and HO_2 addition, so the increase in reactivity is most likely not due to uncertainty in branching fractions of the $R+O_2$ intermediate reactions these radicals represent. Specifically looking at the two cases representing the most extreme branching cases, all 100 ppm HMDSO producing an OH radical or all resulting in an HO_2 radical, there was negligible difference in the predicted ignition delay times. This further indicates the need for a better understanding of the siloxane specific chemistry.

In addition to considering only three of the five possible pathways currently identified for the siloxane reactions, these R+O_2 simulations omit two additional important factors. First, the reaction kinetics of the reactive siloxane intermediate species are not considered, as thermochemistry for these species is not available. These large silicon-containing intermediates account for significant energy as silicon oxidation is highly exothermic. Second, the simulations do not account for the initiation reactions involving the siloxane species which can lead to additional species propagation or termination reactions. The DME analogy and the pathways calculated in Chapter 2 indicate one of the abstraction pathways is HO_2 + HMDSO = H_2O_2 + HMDSOR. Sensitivity analysis of the base H_2/CO mixture shows that both stages of ignition are sensitive to the H_2O_2(+M) = 2OH(+M) reaction. While the DME simulations did not show the HO2+DME as the most active abstraction channel, the HMDSO + HO_2 reaction may be a propagation or radical chain branching channel in the HMDSO system, increasing the production of OH. Additionally, the DME ROP analysis showed the second most active DME consumption channel in the reaction system was CH_3OCH_3 + O = CH_3OCH_2 + OH. The siloxane equivalent could serve as another route to radical chain branching. Until accurate reaction rates and thermochemistry can be calculated for the relevant intermediate species, limited conclusions can be drawn. However, these calculations provide insight into the expected species and reaction pathways affected while highlighting the need for more comprehensive kinetic data for these compounds. For example, since the simulations do not reproduce the magnitude of acceleration observed in the physical ignition experiments, the results indicate that the silicon containing species are strong contributors to the increased energy release and reaction acceleration.

5. Conclusions

Sensitivity and rate of production analysis indicate the mechanism for enhanced reactivity is likely via accelerated production of OH radicals. Since OH and HO_2 chemistry control the behavior of the base syngas mixture, it appears likely the production of OH is increased and/or HO_2 formation is suppressed by the siloxane reactions. Simulation results of the rapid decomposition to the basic organic radical constituents support the hypothesis that the siloxanes are rapid sources of radicals, but the simulations also highlight that the nearly instantaneous decomposition to these species is not the only factor for the increased reactivity and the experimental observations.

Since it has been previously shown that thermal decomposition for both TMSO and HMDSO is not significant below 1200 K, further pathways leading to the increased reactivity and other pathways to radical production were explored. However, with little kinetic data available for the siloxane species and their reactive intermediates, the exploration is limited to organic analogues and representing other radical formation pathways. While the addition of 100 ppm of dimethyl ether accelerated ignition of a base syngas mixture, the approximately 20% decrease in auto-ignition delay time was not as large as observed with the addition of 100 ppm HMDSO in the physical ignition experiments. Simulation of the radical pathways proposed for HMDSO similarly did not capture the full effects observed in physical experiments although the simulations did predict a decrease in ignition delay time. The simulations showed low sensitivity to OH versus HO_2 especially at such the low concentrations of the experiments. Each set of simulations indicates silicon species play key roles in the increased reactivity of the syngas systems, and the siloxanes are not simply fast sources of additional organic radical species like CH_3, OH, HO_2, or H. Further physical and computational data on the thermophysical properties

and the reaction chemistry for the siloxane class of compounds are critical to further understand the impact of siloxanes on combustion and ignition behaviors.

6. Citations

[1] A. Teleki, B. Buesser, M.C. Heine, F. Krumeich, M.K. Akhtar, S.E. Pratsinis, *Ind. Eng. Chem. Res*. 48 (2008) 85-92.

[2] Miller, T. A., Wooldridge, M. S., Bozzelli, J. W. (2004) "Computational modeling of the $SiH_3 + O_2$ reaction and silane combustion," *Combust. Flame* 137:73-92.

[3] O. M. Feroughi, L. Deng, S. Kluge, T. Dreier, H. Wiggers, I. Wlokas, and C. Schlulz, Experimental and numerical study of a HMDSO-seeded premixed laminar low-pressure flame for SiO2 nanoparticle synthesis, *Proc. Combust. Inst*. 36 (2017) 1045–1053.

[4] Chernyshev, E. A., Krasnova, T. L., Sergeev, A. P., Abramova, E. S. (1997) "Siloxanes as sources of silanones," *Russian Chem. Bull*. 46:1586-1589.

[5] A. B. Mansfield and M. S. Wooldridge, The effect of impurities on syngas combustion, Combust. Flame 162 (2015) 2286–2295.

[6] CHEMKIN-PRO 15131, Reaction Design; San Diego, 2103.

[7] J. Li, Z. Zhao, A. Kazakov, M. Chaos, F. L. Dryer, and J. J. Scire, Comprehensive Kinetic Mechanism for CO, CH2O, and CH3OH Combustion, *Int. J. Chem. Kinet.* 39 (2006) 109–136.

[8] Almond, M. J., Becerra, R., Bowes, S.J., Cannady, J.P, Ogeden, J.S., Young, N.A., Walsh, R., A mechanistic study of the low pressure pyrolysis of linear siloxanes, *Phys. Chem. Chem. Phys.* 11 (2009) 9259–9267.

[9] Schwind, R.A, Wooldridge, M.S,. Effects of Organic Silicon Compounds on Syngas Auto-ignition Behavior, *Combust. Flame* in press (2019).

[10] E.W. Kaiser, T.J. Wallington, M. D. Hurley, J. Platz, H. J. Curran, W. J. Pitz, and C. K. Westbrook, *J. Phys. Chem.* A 104, (2000) 8194-8206.

[11] S.S. Zumdahl and S.A. Zumdahl, *Chemistry*, 5th ed, Houghton Mifflin College Division, 1990.

Chapter 5: Conclusions and Recommendations for Future Work

1. Conclusions

Understanding the reaction kinetics of siloxanes is relevant to a variety of applications, but they remain relatively unstudied. Prior research has mostly focused on compounds which are commonly used in chemical vapor deposition processes such as the reaction chemistry of silanes and silicon chlorides, but as more products and processes are relying on siloxanes, the need for defined reaction kinetics for siloxane compounds is apparent. As siloxanes are becoming more prevalent, they are making their way into waste streams and becoming trapped in the derived biogases. By understanding the fundamental reactions governing the behavior of siloxanes, it is possible to explore combustion strategies to mitigate the damaging effects, while simultaneously leveraging the increased energy contribution from these compounds. Such efforts could also potentially negate the need for removal/cleanup from biogas fuels and reduce preprocessing costs. Additionally, reducing the resources necessary for processing waste-to-energy fuels moves the approach closer to economic competitiveness. If landfill gas becomes a more economically attractive option, landfill operators will have more incentive to capture and utilize this harmful greenhouse gas.

This work has provided important new data on the combustion behavior of siloxane compounds which allows new options to be explored to improve biogas operations. First, the results demonstrate that relatively low concentrations of siloxanes significantly increase the reactivity and rate of energy release of a combustion system. While the deleterious effects silica (formed by oxidation of siloxanes) can have on engine operation are well documented, their

influence on the overall energy release of a combustion system has been overlooked. Further, the siloxanes studied in this work systematically considering chemical structure, enabling deeper interpretation of the results of the ignition and pyrolysis studies. Based on studies of analogous hydrocarbons in the literature, the siloxane compounds were expected to be rapid sources of radicals as found in cetane enhancers. However, the effects of HMDSO would then be double the effects (e.g., ignition delay times or pressure rise rates accelerated by a factor of two) of TMSO due to the similar structures, which was not observed. Further probing through computational simulations supported the notion that decomposition to simple radical species, CH_3 and OH, was not the main driver of the increased reactivity observed. When considering the fuel interaction space, this work highlighted the strong influence of base fuel chemistry in the initiating of oxidation reactions at low combustion temperatures. Prior studies have treated the siloxane additives as independent of the base fuel kinetics, but the analysis presented here shows that these interactions are a vital component of the reaction system.

While other studies have looked at the pyrolysis of hexamethyldisiloxane and hexamethylcyclotrisiloxane, the pyrolysis experiments conducted in this study produced first-of-their-kind results at combustion temperatures and time scales. Much of the prior work has focused on flow reactors at lower temperatures and atmospheric pressure. The current work has provided new data vital for deriving thermochemical data for siloxane compounds at high-temperature conditions. Though there have been prior attempts to define the thermochemistry for these compounds, this work identified that the most comprehensive attempt to date is not accurate for combustion or pyrolysis conditions. Prior to this effort, there has been very limited experimental data to validate the proposed models. The experimental data collected in this study provides the necessary basis to validate future thermochemical data as well as kinetic models and

mechanisms for reactions of these compounds. While the mechanism development related to this work is still on-going, notable strides have been made in identifying key reaction pathways. This work is the first to identify $R+O_2 \rightarrow RO_2 \rightarrow QOOH$ pathways as potential drivers for the reactivity observed. Attempts to explore this using an organic analogue, dimethyl ether, have further supported the notion that parallels between carbon and silicon compounds of similar structures are not mechanistically valid.

Furthermore, the TOF-MS data provides time resolved speciation data which allows identification of key intermediate species. The data have been essential to guiding mechanism development and proposing reaction pathways. Some of the most notable characteristics observed in the study are the absence of ethane and the limited detection of silicon species at masses greater than that of the parent molecule in HMDSO which were predicted to be produced in most prior low temperature studies. Specifically, the data collected at the ALS provide high fidelity measurements of time-resolved species concentrations. Due to the highly tunable nature of ionization energy provided by the photon source, compounds such as the inert bath gas do not provide interference and isomers and isobars can be differentiated based upon known ionization energies. This capability has allowed for the identification of masses or mass fragments which had previously been obscured in traditional electron impact ionization experiments. As the thermochemical data for siloxanes are developed, the TOF-MS data from this study will provide needed quantitative results for comparison and refinement.

Prior studies have used organic analogues either for defining reaction rates or identifying similar reaction schemes for siloxanes due to the dearth of siloxane specific data at combustion relevant conditions. This work has highlighted the discrepancy in such approaches and the necessity to understand the specific silicon chemistry in the gas phase. This work has made

strides towards more fundamental understanding of high temperature siloxane chemistry and provides a sound scientific foundation for further work on these important and interesting species.

2. Recommendations for Future Work

A challenge to advancing more fundamental understanding of siloxane combustion is the lack of valid thermochemical data for the stable parent compounds and key intermediates. Theoretical calculations and physical experiments can address this knowledge gap. Time-resolved speciation data can provide a basis for determining which species are key players in the reaction kinetics. Identifying relevant intermediate species for further studies is important as physical experiments are costly and time-consuming and calculating thermochemistry at even a basic theoretical level is extremely computationally expensive due the complexity of the siloxane structures.

This work has provided significant experimental data for three important siloxane compounds over a range of state conditions. Expanding the data set to higher pressures can provide more insights into the reaction chemistry since certain reaction pathways have already been identified as connected to pressure dependent behavior. This will allow for the determination of both HMDSO and TMSO have the same reduction of pressure dependence. Further, expanding the experimental space will provide additional details for developing and validating a more comprehensive mechanism focused on the initiating reactions.

The aim of this work was to understand the initial reaction steps relating to the gas-phase reactant species. However, it is known that siloxanes form silica in combustion systems where there is abundant O_2 for oxidation, and possibly other organosilicon nanoparticles can be formed as well. A key next step is consideration of the heterogeneous chemistry associated with the

formation of these nanoparticles. In particular, the condensed-phase compounds could be a considerable source of energy release due to their low energy state. Further, this will be vital to understanding and successfully modeling the combustion synthesis process for nanoparticles and other silica products that are facing increasing demands from various technical sectors, especially the semi-conductor industry.

There are multiple approaches to studying particle nucleation that can build on the gas-phase siloxane studies. For example, shocktube experiments can be designed to facilitate analysis of the particles deposited on the endwall. Direct kinetics cannot be derived from the particles because the deposits are the result of multiple shockwaves and quenching cycles, but compositional analysis can provide insight on elemental ratios compared with the mass spectrometer data.

Studies of the particle formation kinetics analysis will need to focus on longer reaction times, and flame studies could be well-suited for understanding the particle nucleation kinetics. Collecting speciation data a various heights above a burner surface would allow for both gas-phase intermediates and final condensed-phase products to be identified and quantified. As physical location in a flame is correlated with time in an ignition study, the kinetics identified in the auto-ignition experiments are an excellent basis to design burner experiments.

Overall this work has identified gaps in existing literature and worked towards addressing these needs. Due to the novel nature of this class of compounds as combustion species, a thorough understanding of their behavior in the gaseous phase has been lacking. The fundamental experiments outlined in this study have made significant progress towards addressing this gap, but combustion applications would benefit from further work to define the combustion behavior of siloxane compounds. Continued study of the initiation kinetics as well as

the particulate formation kinetics can provide a more comprehensive understanding relevant to both energy and industrial applications. Through this more thorough understanding, the ability to leverage the energy contribution of siloxane in biogas applications may be realized, leading to more widespread and more economical usage of biogas. Since direct release of biogas is a significant source of greenhouse gas emissions, biogas capture and utilization is also a means to mitigate climate change. The results are also valuable for improving industrial production of silicon products through combustion synthesis. Finally, these kinetics can also be applied to safety systems relating to the propagation of industrial fires and spontaneous combustion at landfills.

APPENDICES

APPENDIX A

Supplementary Material for Syngas Auto-igition Study

Table A.1 – Experimental mixture compositions, state conditions and ignition delay time results

Run-ID	N_2	Ar	O_2	H_2	CO	TMSO	HMDSO	Pressure	Temp	10^4/T	τ_{ign}
units	mol fraction							(atm)	K	(1/K)	ms
S.001	0.723	0.035	0.201	0.012	0.029			9.60	1042	9.60	31.2
S.002	0.723	0.035	0.201	0.012	0.028			9.45	1042	9.60	24.5
S.003	0.723	0.035	0.202	0.012	0.028			9.69	1054	9.49	16.4
S.004	0.723	0.035	0.201	0.012	0.028			8.99	1034	9.67	20.9
S.005	0.723	0.035	0.201	0.012	0.029			9.93	1055	9.48	20.7
S.006	0.723	0.035	0.201	0.012	0.028			9.00	1030	9.71	34.8
S.007	0.723	0.035	0.201	0.012	0.028			9.31	1029	9.72	31.0
S.008	0.723	0.035	0.201	0.012	0.028			9.11	1033	9.68	33.5
S.009	0.723	0.035	0.201	0.012	0.028			8.99	1034	9.67	32.9
S.010	0.723	0.035	0.201	0.012	0.028			9.06	1039	9.63	24.9
S.011	0.723	0.035	0.202	0.012	0.028			8.73	1017	9.83	32.9
S.012	0.723	0.035	0.201	0.012	0.028			9.35	1044	9.58	24.3
S.013	0.723	0.035	0.202	0.012	0.028			10.25	1058	9.45	16.3
S.014	0.723	0.035	0.201	0.012	0.028			9.34	1035	9.66	18.3
S.015	0.723	0.035	0.201	0.012	0.028			9.60	1041	9.60	18.1
S.016	0.723	0.035	0.202	0.012	0.028			10.07	1057	9.46	17.9
S.017	0.723	0.035	0.202	0.012	0.028			10.06	1058	9.45	15.9
H.001	0.722	0.036	0.201	0.012	0.029		0.0001	9.76	1060	9.43	9.3
H.002	0.722	0.036	0.201	0.012	0.029		0.0001	9.18	1043	9.59	8.3
H.003	0.723	0.035	0.202	0.012	0.028		0.0001	9.62	1053	9.50	13.1
H.004	0.723	0.035	0.202	0.012	0.028		0.0001	9.73	1057	9.46	9.0
H.005	0.723	0.035	0.202	0.012	0.028		0.0001	9.13	1029	9.72	18.4
H.006	0.723	0.035	0.202	0.012	0.028		0.0001	8.08	997	10.03	16.8
H.007	0.724	0.035	0.201	0.012	0.028		0.0001	9.26	1045	9.57	13.1
H.008	0.723	0.035	0.202	0.012	0.028		0.0001	9.38	1048	9.54	10.8
T.001	0.723	0.035	0.201	0.012	0.028	0.0001		10.14	1063	9.41	14.3
T.002	0.723	0.035	0.201	0.012	0.028	0.0001		9.87	1058	9.45	13.5
T.003	0.723	0.035	0.201	0.012	0.028	0.0001		9.69	1058	9.45	13.1
T.004	0.723	0.035	0.202	0.012	0.028	0.0001		9.48	1043	9.59	14.0
T.005	0.723	0.035	0.202	0.012	0.028	0.0001		9.36	1039	9.63	14.6
T.006	0.723	0.035	0.201	0.012	0.028	0.0001		9.58	1049	9.54	13.9
T.007	0.723	0.035	0.201	0.012	0.028	0.0001		9.42	1043	9.59	16.4
T.008	0.722	0.036	0.201	0.012	0.028	0.0001		9.99	1057	9.46	10.9
T.009	0.722	0.036	0.201	0.012	0.028	0.0001		10.17	1063	9.40	10.6

APPENDIX B

Supplementary Material for Thermal Decomposition Study of HMDSO, TMSO & HMCTSO

Table B.1 - Experimental mixture compositions and shock conditions for laser schlieren experiments.

*P_1 is the driven section initial pressure, P_4 is the driver section pressure, T_1 is the initial temperature of the mixture, t1-t4 are the time intervals of the shockwave passing between each of the pressure transducers (ie, t1=time transducer 2 trigger – time transducer 1 trigger, t2=3 trigger -2 trigger, etc), topt is the average time interval used to calculate shock velocity, DV/Dt is the voltage calibration for the angular deflection, T_2 and P_2 are the indicent shock conditions which are also the state reaction conditions. (Shocks shown in figures are highlighted)

Shock #	P_4 psia	P_1 torr	T_1 °C	t1	t2	t3	t4	topt	DV/Dt	T_2 K	P_2 torr
2% HMDSO in Krypton - July 2018											
1	33	38.5	22	116.2	116	115.8	115.6	115.9	13.005	1802	119
2	35.00	3.70	22.0	110.5	110.1	110.0	109.8	110.1	12.5158	1957	127
3	34.00	3.71	22.0	116.5	116.2	116.1	115.9	116.2	12.5158	1795	114
4	34.00	3.77	22.0	117.6	117.3	117.0	116.6	117.1	12.5600	1772	114
5	15.10	3.01	22.0	137.4	137.0	136.7	136.5	136.9	12.6650	1390	66
6	17.00	2.70	22.0	134.3	133.7	133.3	133.1	133.6	12.4558	1443	62
7	19.00	2.40	22.0	128.9	128.4	128.2	128.1	128.4	12.6542	1534	60
8	20.00	2.30	22.0	125.4	124.8	124.5	124.3	124.7	12.5475	1605	61
9	20.70	2.20	22.0	124.6	124.0	123.7	123.5	123.9	12.3033	1620	59
10	21.50	2.20	21.8	122.3	122.0	121.8	121.6	121.9	12.2983	1663	61
11	22.20	2.20	21.8	122.9	122.4	122.0	121.9	122.3	12.2717	1655	61
12	23.00	2.10	21.8	120.6	120.3	120.0	119.7	120.2	12.3000	1701	60
13	24.00	2.10	21.8	119.9	119.6	119.4	119.2	119.5	12.3308	1716	61
14	25.00	2.00	21.8	118.2	117.8	117.3	117.1	117.6	12.3592	1760	60
15	26.00	1.90	21.8	116.0	115.8	115.5	115.2	115.6	12.3583	1809	59
16	27.50	1.90	22.0	114.0	113.7	113.5	113.3	113.6	12.3192	1860	61
17	28.50	1.80	22.0	112.5	112.4	112.2	112.0	112.2	12.4325	1897	59
18	29.50	1.80	22.0	111.8	111.5	111.1	110.9	111.3	12.2942	1923	60
2% HMDSO in Krypton - February 2018											
1	20.00	6.01	21.9	139.8	138.8	138.8	138.5	138.9	14.0100	1360	128
2	22.00	5.20	21.9	134.3	133.6	133.4	133.2	133.6	14.1125	1443	120
3	25.00	5.00	21.9	129.1	128.5	128.2	128.0	128.4	14.2267	1534	125
4	27.00	4.80	21.9	125.9	125.5	125.3	125.1	125.4	14.1800	1590	126
5	29.00	4.61	21.9	122.6	122.1	121.9	121.8	122.1	14.0050	1660	128
6	30.00	4.00	21.9	119.0	118.7	118.5	118.3	118.6	14.0725	1737	118

Shock #	P_4 psia	P_1 torr	T_1 °C	t1	t2	t3	t4	topt	DV/Dt	T_2 K	P_2 torr
7	32.00	3.90	21.9	116.2	116.1	115.9	115.8	116.0	14.0417	1800	120
8	34.00	3.80	21.9	114.3	113.9	113.7	113.6	113.9	14.1600	1854	122
9	26.00	4.90	21.9	126.5	126.0	125.7	125.5	125.9	14.2058	1581	128
10	28.00	4.70	21.9	123.7	123.5	123.1	123.1	123.3	14.2800	1633	128
11	29.50	4.30	21.9	120.5	120.1	119.9	119.8	120.1	14.3208	1704	124
12	31.00	4.00	21.9	118.0	117.8	117.6	117.5	117.7	14.4175	1758	120
13	33.00	3.85	21.9	115.1	114.9	114.7	114.6	114.8	14.3208	1829	121
1% HMDSO in Krypton - April 2019											
2	33.00	3.85	21.2	114.0	116.1	113.2	113.0	114.0	36.4333	2060	117
3	33.00	3.85	21.2	114.4	116.6	113.6	113.3	114.4	36.0833	2048	117
4	31.00	3.95	21.1	116.3	115.7	115.5	115.3	115.7	36.4800	2010	117
5	29.00	4.15	21.0	118.9	118.2	118.1	117.8	118.3	36.1367	1938	118
6	27.00	4.35	21.2	121.9	121.5	121.3	121.0	121.4	36.4900	1855	117
7	26.00	4.56	21.3	124.1	123.4	123.2	122.9	123.4	36.2367	1806	118
8	25.00	4.85	21.3	125.9	125.6	125.4	125.1	125.5	36.1100	1756	122
9	24.00	4.95	21.3	128.8	128.5	128.3	127.9	128.4	35.6867	1693	119
10	23.00	5.15	21.3	130.6	130.2	129.9	129.6	130.1	0.0000	1657	120
11	22.00	5.30	21.4	132.5	131.9	131.5	131.2	131.8	35.8567	1622	120
12	21.00	5.45	21.3	136.1	135.5	135.2	134.8	135.4	35.8400	1553	117
13	20.00	5.85	21.3	139.0	138.6	138.3	137.9	138.4	36.0500	1499	120
14	19.00	6.10	21.3	143.0	142.4	142.0	141.6	142.2	36.0133	1436	118
15	21.50	5.45	21.3	134.8	134.2	133.8	133.5	134.1	36.1867	1578	119
16	28.00	4.37	21.5	121.3	120.7	120.4	120.1	120.6	35.1267	1876	119
17	30.00	4.17	21.5	118.3	117.7	117.7	117.5	117.8	36.7967	1951	119
19	30.00	1.75	20.8	105.8	105.7	105.5	105.3	105.5	40.4700	2350	63
20	23.00	2.06	20.9	115.2	114.9	115.0	114.8	115.0	39.8267	2032	62
21	22.00	2.05	20.9	117.5	117.3	117.2	116.9	117.2	39.2267	1967	59
22	21.00	2.15	21.0	119.0	118.8	118.6	118.3	118.7	39.1667	1926	60
23	20.00	2.25	21.0	121.6	121.3	121.1	120.9	121.2	39.2433	1860	61
24	19.00	2.32	21.0	124.0	123.9	123.8	123.6	123.8	38.9033	1796	60
25	18.00	2.40	21.0	126.3	125.9	125.7	125.3	125.8	38.4700	1749	60
26	17.00	2.47	21.0	130.0	129.7	129.4	129.2	129.6	38.4767	1667	58
27	16.00	2.80	21.0	134.3	133.8	133.5	133.3	133.7	38.8633	1584	62
28	15.00	2.81	21.0	137.4	137.1	136.7	136.3	136.8	37.8433	1527	59
29	16.50	2.65	21.1	132.8	132.4	132.2	131.8	132.3	37.2533	1611	60
30	17.50	2.47	21.1	128.8	128.2	127.8	127.4	128.1	37.7700	1699	59
31	22.00	0.90	21.1	106.9	106.6	106.4	106.2	106.5	37.5500	2314	32
32	18.00	1.05	21.1	114.0	113.8	113.7	113.5	113.7	37.1200	2069	32
33	17.50	1.05	21.1	115.9	115.4	115.2	114.8	115.3	37.1300	2021	31
34	17.00	1.05	21.1	116.3	115.9	115.9	115.7	115.9	37.4767	2003	31
35	16.50	1.10	21.1	119.3	118.7	118.5	118.2	118.7	37.1967	1927	31

Shock #	P_4 psia	P_1 torr	T_1 °C	t1	t2	t3	t4	topt	DV/Dt	T_2 K	P_2 torr
36	16.00	1.11	21.1	120.4	120.0	119.7	119.3	119.8	37.2267	1896	31
37	15.40	1.14	21.1	122.1	121.7	121.3	120.9	121.5	37.6767	1853	31
38	14.80	1.18	21.2	124.5	124.0	123.6	123.3	123.9	37.0500	1794	30
39	14.20	1.23	21.2	126.7	126.4	126.1	125.7	126.2	36.7533	1740	30
40	13.60	1.28	21.2	129.2	128.5	128.3	127.9	128.5	37.7133	1690	31
41	13.10	1.30	21.1	131.4	130.9	130.5	130.2	130.7	37.5967	1643	30
42	12.50	1.34	21.2	133.2	132.6	132.4	132.2	132.6	37.0100	1606	30
43	11.90	1.38	21.1	133.8	133.6	133.4	133.1	133.5	37.3900	1589	31
44	11.50	1.40	21.0	137.5	136.9	136.6	136.2	136.8	36.5767	1527	29
45	16.75	1.05	21.2	117.1	116.6	116.3	116.0	116.5	36.5833	1987	31
0.5% HMDSO in Krypton - April 2019											
7	27.00	4.50	21.7	120.3	120.0	119.9	119.7	120.0	39.5533	2010	119
8	26.00	4.65	21.8	122.1	121.7	121.5	121.2	121.6	38.7933	1963	120
9	25.00	4.80	21.8	123.4	123.3	123.0	122.7	123.1	38.5167	1924	121
11	23.00	5.00	21.8	127.7	127.2	127.1		127.3	36.0500	1816	118
12	24.00	4.90	21.8	125.9	125.4	125.1		125.5	37.1367	1862	119
13	22.00	5.21	21.9	130.4	129.9	129.5		129.9	37.0967	1756	117
14	21.00	5.60	21.8	134.2	133.6	133.1		133.6	36.5100	1676	119
15	20.00	5.85	21.8	138.6	137.9	137.5		138.0	36.5200	1589	117
16	19.00	6.25	21.9	142.4	141.9	141.5		141.9	37.0067	1518	118
17	19.50	6.10	21.9	142.0	141.4	141.0		141.4	37.0933	1526	116
18	20.50	5.80	21.9	137.2	136.9	136.5		136.8	36.4067	1611	118
19	21.70	5.50	21.9	131.3	130.7	130.3		130.7	36.5600	1738	122
20	20.00	2.25	22.0	120.1	120.0	119.8		120.0	36.8433	2010	60
21	19.00	2.35	22.0	122.6	122.1	121.8		122.2	36.4033	1949	60
22	18.00	2.45	22.0	126.2	125.7	125.4		125.8	37.2400	1855	59
23	18.50	2.40	22.0	123.8	123.5	123.1		123.4	36.5433	1914	60
24	17.50	2.50	22.0	127.1	126.7	126.5		126.8	36.7533	1830	59
25	16.80	2.55	22.0	129.9	129.6	129.3		129.6	36.6367	1764	58
26	17.00	2.55	22.0	128.1	127.9	127.6		127.8	35.8500	1805	59
27	16.50	2.60	22.0	130.2	129.8	129.5		129.8	36.0733	1758	59
28	16.00	2.70	22.0	132.0	131.6	131.3		131.6	37.0600	1719	59
29	15.50	2.80	22.0	134.8	134.2	133.8		134.3	36.8833	1663	59
30	15.00	2.95	22.0	137.2	136.6	136.3		136.7	36.0800	1614	60
31	14.50	3.10	22.0	139.7	139.4	139.1		139.4	35.8933	1563	61
32	15.40	1.14	22.0	120.2	119.7	119.3		119.7	36.7800	2017	30
33	15.00	1.18	22.0	121.1	120.8	120.8		120.9	35.9667	1984	31
34	14.50	1.21	22.0	122.7	122.4	122.4		122.5	35.5833	1940	31
35	14.00	1.24	22.0	125.4	124.7	124.4		124.8	35.6267	1879	30

Shock #	P_4 psia	P_1 torr	T_1 °C	t1	t2	t3	t4	topt	DV/Dt	T_2 K	P_2 torr
38	13.50	1.27	21.0	127.5	126.8	126.5	126.1	126.7	41.6200	1831	30
39	13.00	1.30	21.0	128.5	128.2	128.0	127.6	128.1	42.2033	1799	30
40	12.30	1.35	21.1	132.4	131.9	131.5	131.1	131.7	42.6900	1715	30
41	12.50	1.32	21.3	131.4	131.0	130.7	130.2	130.8	40.8500	1736	29
42	11.80	1.40	21.3	135.7	135.4	135.1	134.6	135.2	40.6667	1643	29
43	11.50	1.45	21.3	135.1	134.4	134.2	133.8	134.4	40.0900	1660	31
2% TMSO in Krypton - July 2018											
3	22.50	5.80	22.9	133.1	132.7	132.4	132.1	132.6	12.8667	1591	129
4	27.00	5.20	23.0	125.7	125.2	124.8	124.5	125.0	13.2292	1749	130
5	24.00	5.60	23.0	132.6	132.4	132.2	132.0	132.3	13.1692	1596	125
6	24.00	5.60	23.0	130.2	129.7	129.5	129.4	129.7	13.1642	1648	130
7	25.50	5.40	23.0	127.8	127.3	127.0	126.9	127.2	12.8758	1700	130
8	28.50	5.00	23.2	122.9	122.4	122.2	122.0	122.4	13.0742	1812	130
9	30.00	4.80	23.0	121.1	120.5	120.3	120.0	120.5	13.1792	1859	129
10	31.50	4.60	23.0	117.9	117.5	117.3	117.2	117.5	13.1883	1938	130
11	32.50	4.50	23.2	116.8	116.4	116.3	116.1	116.4	13.1958	1969	130
12	15.00	3.00	23.2	136.7	136.4	136.2	136.0	136.3	13.0767	1522	63
13	16.00	2.85	23.2	133.0	132.7	132.6	132.5	132.7	13.0525	1589	63
14	17.00	2.70	23.2	130.9	130.5	130.2	130.0	130.4	13.1700	1634	62
15	17.00	2.61	22.5	129.9	129.2	128.9	128.8	129.2	12.5608	1658	61
16	17.70	2.60	22.5	128.1	127.6	127.2	127.1	127.5	12.6000	1694	63
17	18.50	2.50	22.5	125.9	125.3	124.9	124.7	125.2	12.6267	1745	62
18	19.20	2.40	22.5	123.6	123.2	122.8	122.6	123.0	12.4658	1795	62
19	20.00	2.30	22.5	122.4	121.8	121.6	121.5	121.8	12.5258	1825	61
20	20.70	2.21	22.5	118.9	118.9	118.6	118.4	118.7	12.5125	1906	61
21	21.50	2.10	22.5	116.9	116.8	116.5	116.3	116.6	12.4058	1962	61
22	22.20	2.00	22.7	114.6	114.3	114.1	114.0	114.2	12.4517	2030	60
23	12.00	1.70	22.7	136.5	136.2	135.9	135.7	136.1	12.4758	1526	36
24	13.30	1.51	22.7	129.6	129.3	129.1	129.0	129.2	12.4558	1657	35
25	14.00	1.40	22.7	127.6	126.9	126.5	126.1	126.8	12.4417	1710	34
26	14.00	1.40	22.5	128.4	128.0	127.6	127.3	127.8	12.9692	1687	33
27	14.70	1.30	22.4	124.9	124.4	124.2	124.0	124.4	12.9350	1764	33
28	14.40	1.20	22.4	121.6	121.1	120.6	120.4	120.9	12.8733	1848	32
29	16.10	1.10	22.4	119.5	119.1	118.9	118.8	119.0	12.6775	1896	30
30	16.80	1.10	22.4	117.8	117.5	117.1	116.8	117.3	12.7725	1943	31
31	17.50	1.10	22.4	117.0	116.3	116.0	115.9	116.3	12.6058	1971	32
32	18.20	1.10	22.5	113.9	113.7	113.5	113.3	113.6	12.5558	2050	33
33	18.70	1.05	22.5	112.8	112.7	112.5	112.4	112.6	12.5683	2080	33

Shock #	P_4 psia	P_1 torr	T_1 °C	t1	t2	t3	t4	topt	DV/Dt	T_2 K	P_2 torr
34	19.20	0.97	22.5	110.7	110.5	110.5	110.5	110.5	12.5750	2146	31
35	15.00	1.25	22.5	122.4	122.0	121.7	121.5	121.9	12.4683	1823	33
1% TMSO in Krypton - April 2019											
1	29.00	4.15	22.2	117.6	117.0	116.9	116.7	117.0	37.7133	2084	115
2	29.00	4.35	22.2	117.4	117.0	116.9	116.6	116.9	37.0967	2087	121
3	28.00	4.20	22.2	117.9	117.6	117.3	117.0	117.5	36.8933	2071	116
4	27.00	4.25	22.2	120.0	119.3	119.1	118.8	119.3	36.6900	2016	114
5	27.00	4.45	22.2	119.1	119.1	119.1	118.9	119.0	37.4933	2025	120
6	26.00	4.55	22.3	122.5	122.2	122.1	121.8	122.1	37.0600	1938	116
7	26.50	4.55	22.3	121.5	121.2	120.9	120.7	121.1	37.2800	1967	118
8	25.50	4.70	22.3	123.2	122.7	122.6	122.3	122.7	36.6567	1923	119
9	25.50	4.70	22.3	125.4	125.2	124.9	124.4	125.0	36.7200	1864	114
10	23.50	5.05	22.3	128.4	128.1	127.9	127.5	127.9	36.7100	1792	117
11	22.00	5.35	22.3	132.2	131.7	131.3	130.9	131.5	36.7133	1711	117
12	22.50	5.40	22.3	131.0	130.7	130.3	130.0	130.5	36.6833	1734	120
13	21.50	5.60	22.3	134.9	134.3	133.9	133.4	134.1	36.5733	1656	118
14	20.50	5.95	22.3	137.6	137.1	136.7	136.2	136.9	36.2467	1601	120
15	19.50	6.25	22.3	140.5	140.0	139.7	139.3	139.9	36.4100	1546	121
16	21.00	2.15	22.5	117.1	117.1	116.7	116.3	116.8	36.2133	2091	60
17	22.00	2.07	22.5	115.3	115.1	114.9	114.7	115.0	36.3000	2149	60
18	20.00	2.23	22.5	120.9	120.4	120.2	119.9	120.3	36.0800	1988	58
19	20.50	2.21	22.5	118.4	118.3	118.2	118.0	118.2	35.4133	2049	60
20	19.50	2.35	22.5	122.0	121.7	121.5	121.1	121.6	35.7167	1953	60
22	19.00	2.39	21.6	123.8	123.5	123.3	123.0	123.4	40.9067	1904	60
23	18.50	2.43	21.6	124.9	124.5	124.4	124.1	124.5	40.2367	1876	60
24	18.00	2.47	21.8	125.8	124.9	124.4	124.2	124.8	40.1333	1867	60
25	17.50	2.51	21.8	128.1	127.7	127.3	127.0	127.5	39.6567	1802	59
26	17.00	2.59	21.8	129.2	128.6	128.3	127.9	128.5	39.2467	1779	60
27	16.50	2.65	21.8	130.7	130.5	130.3	130.0	130.4	39.6333	1736	59
28	16.00	2.75	21.9	134.2	133.8	133.5	133.2	133.7	39.3767	1665	58
29	15.50	2.93	21.9	136.0	135.8	135.6	135.2	135.7	38.7933	1625	60
30	15.00	3.09	21.9	138.1	137.8	137.5	137.1	137.6	37.8233	1587	62
31	16.25	2.73	21.9	131.2	130.8	130.7	130.4	130.8	38.0267	1727	61
32	15.40	1.14	21.9	120.4	120.0	119.7	119.5	119.9	37.3933	1999	30
33	15.80	1.10	21.9	119.2	118.7	118.3	118.1	118.6	37.2767	2038	30
34	16.20	1.06	21.9	118.3	117.8	117.3	116.9	117.6	37.1100	2068	29
35	16.60	1.06	21.9	117.4	117.2	117.0	116.9	117.1	36.9800	2082	29
36	17.00	1.06	21.9	116.4	116.2	116.1	116.0	116.1	36.8467	2111	30

Shock #	P_4 psia	P_1 torr	T_1 °C	t1	t2	t3	t4	topt	DV/Dt	T_2 K	P_2 torr
37	17.04	1.05	21.9	115.8	115.6	115.3	114.9	115.4	37.0167	2136	30
38	18.20	1.03	21.9	113.6	113.4	113.0	112.7	113.2	37.1367	2208	31
39	17.80	1.03	21.9	113.7	113.6	113.5	113.4	113.5	36.8433	2196	30
40	15.00	1.18	22.0	122.7	122.1	121.7	121.3	122.0	36.5867	1942	30
41	14.60	1.22	22.0	123.5	123.1	122.8	122.5	123.0	36.6167	1915	31
42	14.20	1.24	22.0	125.0	124.9	124.7	124.5	124.8	36.6267	1869	30
43	13.80	1.27	22.1	126.9	126.6	126.3	125.9	126.4	40.1100	1828	30
44	13.40	1.30	22.1	128.6	128.1	127.9	127.7	128.1	39.6933	1789	30
45	13.00	1.34	22.1	129.9	129.5	129.2	128.9	129.4	39.4100	1759	30
46	12.60	1.39	22.1	131.8	131.5	131.2	130.7	131.3	39.6400	1716	31
0.5% TMSO in Krypton - April 2019											
2	27.00	4.45	21.8	119.7	119.0	118.6	118.2	118.9	40.8000	2182	115
3	26.00	4.65	21.8	121.2	120.9	120.6	120.4	120.8	41.5000	2045	119
4	25.00	4.85	21.9	122.9	122.5	122.2	122.0	122.4	41.4300	1999	121
5	24.00	5.01	21.9	125.0	124.7	124.4	124.2	124.6	40.1833	1939	121
6	23.00	5.15	21.9	126.9	126.8	126.5	126.2	126.6	40.6200	1886	120
7	22.00	5.30	21.9	130.0	129.9	129.3	128.8	129.5	40.3100	1814	118
8	21.00	5.50	21.9	132.6	132.1	131.9	131.5	132.0	39.5333	1756	118
9	20.00	5.75	21.9	135.5	134.9	134.5	134.1	134.7	38.8900	1697	118
10	19.00	6.05	21.9	139.1	138.5	138.2	137.8	138.4	38.4367	1623	117
11	18.00	6.40	22.0	143.0	142.3	141.8	141.3	142.1	38.6367	1553	118
12	21.50	5.25	22.0	131.6	131.0	130.8	130.6	131.0	37.5833	1780	114
13	22.50	5.25	21.9	128.9	128.3	128.1	128.0	128.3	39.4433	1843	119
14	19.50	5.90	21.9	138.1	137.6	137.3	137.0	137.5	39.1600	1640	116
15	20.50	2.20	22.0	118.4	118.0	117.8	117.5	117.9	38.4833	2132	59
16	21.50	2.15	21.9	116.7	116.3	115.8	115.5	116.1	39.1933	2192	60
17	19.50	2.29	22.0	120.3	120.4	120.0	119.6	120.1	38.4600	2066	59
18	18.50	2.36	21.9	122.1	121.8	121.6	121.5	121.7	38.7567	2017	59
19	17.50	2.45	21.9	125.0	124.6	124.5	124.3	124.6	37.7333	1938	59
20	16.50	2.55	22.0	129.0	128.6	128.2	128.0	128.4	37.4833	1840	58
21	16.00	2.63	22.0	130.1	129.8	129.4	129.1	129.6	37.2233	1812	58
22	15.00	2.80	22.0	133.3	132.8	132.4	132.2	132.7	36.8767	1741	59
23	14.50	2.90	22.0	136.2	135.5	135.1	134.7	135.4	36.5400	1683	59
24	18.00	2.40	22.0	123.9	123.3	123.3	123.1	123.4	37.0600	1971	59
25	17.00	2.60	22.0	127.7	127.1	126.8	126.5	127.0	36.7100	1875	60
26	15.50	2.73	22.0	131.4	131.1	130.8	130.6	131.0	36.2833	1780	59
28	14.60	1.22	22.2	122.6	122.7	122.7	122.5	122.6	39.0167	1992	30
29	15.00	1.18	22.2	121.9	121.7	121.5	121.4	121.6	39.2067	2021	30

Shock #	P_4 psia	P_1 torr	T_1 °C	t1	t2	t3	t4	topt	DV/Dt	T_2 K	P_2 torr
30	15.40	1.14	22.2	119.3	119.2	119.3	119.3	119.3	38.4167	2090	30
31	15.80	1.10	22.2	119.5	119.6	119.5	119.3	119.5	38.1667	2084	29
32	16.20	1.08	22.2	118.1	117.8	117.6	117.3	117.7	37.7100	2139	29
33	16.60	1.08	22.2	116.9	116.6	116.7	116.7	116.7	37.3167	2171	30
34	14.20	1.26	22.2	125.3	125.4	125.1	124.6	125.1	37.5633	1925	30
35	14.40	1.24	22.3	123.6	123.0	122.8	122.9	123.1	37.1367	1980	31
36	14.00	1.30	22.2	124.7	124.6	124.3	124.0	124.4	37.4967	1945	31
37	13.60	1.28	22.2	127.2	126.7	126.4	126.2	126.6	37.2400	1886	30
38	13.20	1.30	22.2	127.2	127.1	126.8	126.5	126.9	37.0867	1879	30
39	12.80	1.32	22.3	129.1	128.5	128.2	127.9	128.4	36.7600	1840	30
40	12.40	1.34	22.3	129.8	129.7	129.5	129.3	129.6	36.1267	1813	30
41	12.00	1.36	22.3	131.8	131.1	130.7	130.6	131.0	35.6300	1779	29
2% HMCTSO in Krypton - July 2018											
1	22.10	5.20	22.0	137.0	136.3	136.0	135.9	136.3	12.2008	1415	117
2	23.00	5.20	22.0	136.0	135.0	134.9	134.4	135.0	12.2667	1435	119
3	30.00	5.00	22.0	120.9	120.7	120.5	120.4	120.6	12.3258	2127	126
4	24.50	5.10	22.0	133.5	132.7	132.5	132.3	132.7	12.2592	1473	121
5	26.00	5.00	22.0	131.9	131.1	130.8	130.7	131.1	12.2742	1501	122
6	26.00	5.00	22.0	130.1	129.7	129.4	129.2	129.6	12.2000	1529	125
7	29.50	4.80	22.0	127.0	126.3	126.1	125.8	126.3	12.2842	1591	126
8	31.00	4.65	22.0	125.2	124.9	124.7	124.6	124.8	12.3517	1620	125
9	33.00	4.50	22.2	123.4	122.9	122.7	122.6	122.9	12.4233	1661	125
10	35.00	4.30	22.2	121.3	120.6	120.2	120.0	120.5	12.5592	1712	124
11	37.00	4.10	22.2	118.4	118.2	117.9	117.8	118.1	12.0975	1769	124
12	39.00	3.90	22.2	116.2	116.0	115.7	115.6	115.8	12.1400	1824	122
13	41.00	3.70	23.8	114.5	114.3	113.9	113.7	114.1	12.3642	1870	119
14	43.10	3.70	23.8	113.6	113.2	113.0	112.7	113.1	12.4033	1896	121
15	45.50	3.60	23.8	111.3	111.1	110.9	110.7	111.0	12.3308	1955	123
16	16.00	3.00	24.0	136.7	136.6	136.1	135.9	136.3	12.1967	1416	67
17	17.00	3.85	24.0	139.4	139.0	138.8	138.6	139.0	12.0900	1375	83
18	17.00	2.85	24.0	134.4	133.7	133.4	133.2	133.7	12.3925	1459	66
19	18.00	2.60	24.0	131.1	130.7	130.3	130.0	130.5	12.5533	1514	64
20	19.00	2.45	24.0	128.5	128.1	127.9	127.7	128.0	12.5208	1559	62
21	20.70	2.45	24.0	126.0	125.6	125.4	125.2	125.5	12.4775	1607	65
22	22.00	2.41	24.0	123.6	123.5	123.3	123.2	123.4	12.5458	1651	66
23	23.50	2.41	24.3	122.5	122.3	122.1	121.9	122.2	12.5483	1677	67
24	25.00	2.30	24.3	121.2	120.8	120.4	120.1	120.6	12.5033	1712	66
25	26.50	2.20	24.3	118.4	118.2	117.8	117.5	118.0	12.3475	1773	66

Shock #	P_4 psia	P_1 torr	T_1 °C	t1	t2	t3	t4	topt	DV/Dt	T_2 K	P_2 torr
26	28.00	2.10	24.3	116.4	115.9	115.5	115.4	115.8	12.1842	1826	66
27	29.60	2.00	24.3	113.8	113.5	113.2	113.0	113.4	12.1883	1890	65
28	31.00	1.90	24.3	112.8	112.5	112.1	111.8	112.3	11.9950	1919	63
29	33.00	1.90	24.3	110.2	109.7	109.5	109.4	109.7	11.7975	1993	66
30	34.60	1.80	24.3	109.1	108.9	108.7	108.5	108.8	11.8592	2020	64
31	12.00	2.00	24.3	140.1	139.0	139.0	138.6	139.1	11.9750	1373	43
32	13.00	1.70	24.3	135.1	133.9	133.8	133.5	134.0	11.9592	1453	39
33	14.20	1.60	24.3	130.1	129.8	129.6	129.5	129.8	11.9792	1527	40
34	15.10	1.41	24.4	126.5	126.0	125.8	125.6	126.0	11.9333	1599	37
35	15.00	1.10	24.4	124.4	123.9	123.7	123.5	123.9	11.8783	1642	30
36	16.10	1.10	24.4	121.6	121.4	121.1	120.9	121.2	12.0500	1698	31
37	17.00	1.10	24.4	120.3	119.9	119.6	119.5	119.8	12.1842	1731	32
38	18.00	1.05	23.4	117.6	117.2	117.0	116.9	117.2	11.7217	1792	32
39	19.00	1.00	23.2	116.5	116.1	115.9	115.7	116.0	11.8325	1820	31
40	20.00	0.95	23.2	114.2	113.9	113.8	113.6	113.8	11.7417	1876	31
41	21.00	0.90	23.2	111.6	111.4	111.2	111.1	111.3	11.6425	1946	31
42	22.00	0.90	23.2	111.3	111.0	111.0	110.8	111.0	11.6258	1954	31
43	23.10	0.85	23.2	108.9	108.6	108.5	108.5	108.6	11.5733	2025	30

Table B.2 - Experimental mixture compositions and shock conditions for DFST-TOFMS experiments.

*P_1 is the driven section initial pressure, P_4 is the driver section pressure, t1-t3 are the time intervals of the shockwave passing the pressure transducers (i.e. t1 is the time of the wave passing transducer 2 minus the time of the wave passing transducer 1, t2 is time it passes 3 minus the time it passes 2, etc) with the average used to calculate shock velocity, T_2 and P_2 are the incident shock conditions, T_5 and P_5 are the reflected shock conditions which are also the reaction conditions. The nozzle and skimmer size are listed as well. (Shocks averaged for figures are highlighted)

Shock #	P_4 psia	P_1 torr	T_1 °C	t1	t2	t3	T_2 K	P_2 torr	T_5 K	P_5 torr
1	30	5	22	59.2	-	-	1008	54	1948	241
2	30	5	22	59.1	-	-	1010	54	1954	242
3	20	5	22	64.6	-	-	893	46	1667	193
4	15	10	22	76.9	75.6	105	711	64	1230	240
5	15	10	22	76.8	75.5	75.4	713	65	1236	242
6	20	5	21.7	66.6	65.8	65.5	862	43	1594	179
7	20	5	21.7	66.4	65.4	65.2	865	44	1601	182
8	20	5	21.7	66	65.1	64.8	869	44	1610	183
9	20	5	21.7	66	65.1	64.9	869	44	1610	183
10	20	5	21.7	65.9	65.2	64.9	871	44	1615	184
11	20	5	21.7	65.8	64.9	64.7	874	44	1624	186
12	20	5	21.7	67.2	66.3	66.1	847	42	1557	174
13	20	5	21.7	66.1	65.2	65	869	44	1610	183
14	20	5	21.7	66	65	64.8	873	44	1619	185
15	20	5	21.7	65.9	65	64.8	873	44	1619	185
16	20	5	21.7	65.7	64.8	64.6	876	44	1628	186
17	20	5	21.7	66.4	65.5	65.2	863	43	1597	181
18	23	4.7	21.7	63.4	62.5	62.2	922	45	1740	193
19	21.5	4.85	21.7	64.3	63.5	63.3	902	45	1690	191
20	24.5	4.55	21.7	62.2	61.3	61.1	948	45	1803	197
21	26	4.38	21.7	61	60.2	59.9	975	45	1870	199
22	27.5	4.18	21.7	59.9	59.1	58.8	1002	45	1934	200
23	29	3.9	21.7	59.1	58.4	58.1	1020	43	1977	192
1	23	4.7	21.8	63.7	62.7	62.6	947	42	1799	170
2	20	5	21.8	65.8	64.7	-	906	42	1698	166
3	17	5.3	21.8	69.5	-	-	829	39	1514	147
4	15.5	5.45	21.8	72.7	71.3	-	765	39	1360	154
5	15.5	5.4	21.8	71.3	70	70.1	787	41	1413	164
6	14.5	5.4	21.8	72	-	-	765	39	1360	153
7	15.5	5.4	22	71.6	70.1	-	783	40	1402	160
8	15.5	5.4	22	71.2	-	-	780	40	1395	159
9	15.5	5.4	22	71	69.7	-	789	41	1416	163

Shock #	P_4 psia	P_1 torr	T_1 °C	t1	t2	t3	T_2 K	P_2 torr	T_5 K	P_5 torr
10	15.5	5.4	22	71.1	70	-	787	41	1413	162
11	15.5	5.4	22	71	69.6	-	790	41	1420	163
12	15.5	5.4	22	71	69.7	-	790	41	1420	163
13	15.5	5.4	22	71.1	69.8	-	789	41	1416	163
14	15.5	5.4	22	71.3	69.7	-	787	41	1413	162
15	15.5	5.4	22	71.1	69.6	-	789	41	1416	163
16	15.5	5.4	22	70.7	69.4	-	793	41	1427	165
17	15.5	5.4	22	70.7	69.4	-	793	41	1427	165

Table B.3a- TOF-MS settings for DFST TOF-MS experiments
*A pulse duration of 1 us and frequency of 100 kHz were set for each experiment

Shocks	Liner V	Lens V	Central Grid V	Last Grid V	Repeller V	Extractor V	Deflect X	Deflect Y	MCP V	Ionization Energy V
0.5% HMDSO, 2.0% Argon, 97.5% Neon – March 2018										
1-5	8990	9000	3200	220	800	800	5	1.06	1560	-32
6-7	8990	9000	3200	220	800	800	5	1.06	1650	-32
8-23	8990	9000	3200	220	800	800	5	1.06	1650	-28
0.5% TMSO, 2.0% Argon, 97.5% Neon – April 2018										
1	8990	9000	3200	220	800	800	5	1.06	1600	-32
2-18	8990	9000	3200	220	800	800	5	1.06	1560	-27.5

Table B.3b- TOF-MS species used for calibration for DFST TOF-MS experiments
*m/z listed here are the widely accepted values reported in literature

Shocks	Species	m/z	TOF us
0.5% HMDSO, 2.0% Argon, 97.5% Neon – March 2018			
1-2	Neon, 20	19.9924	2.34567
	Argon, 40	39.9623	3.22962
	Krypton, 84	83.9115	4.60007
	HMDSO, 147	147	6.00634
3-5	Helium, 4	4.0026	1.16116
	Neon, 20	19.9924	2.34567
	Argon, 40	39.9623	3.22962
	Krypton, 84	83.9115	4.60007
	HMDSO, 147	147	6.00634
6-7	Helium, 4	4.0026	1.14808
	Neon, 20	19.9924	2.34758
	Argon, 40	39.9623	3.23024
	Krypton, 84	83.9115	4.56807
	HMDSO, 147	147	6.00002
8-23	Helium, 4	4.0026	1.15446
	Neon, 20	19.9924	2.33289
	Argon, 40	39.9623	3.2161
	HMDSO, 147	147	5.99225
0.5% TMSO, 2.0% Argon, 97.5% Neon – April 2018			
1-3	Helium, 4	4.0026	1.14805
	Neon, 20	19.9924	2.33119
	Neon, 22	21.9914	2.43902
	Argon, 40	39.9623	3.21411
	TMSO, 75	75	4.33303

Shocks	Species	m/z	TOF us
4-6	Helium, 4	4.0026	1.14805
	Neon, 20	19.9924	2.33119
	Neon, 22	21.9914	2.43902
	Argon, 40	39.9623	3.21411
	TMSO, 75	75	4.33303
	OMTSO, 221	221	7.31213
7-17	Helium, 4	4.0026	1.17015
	Neon, 20	19.9924	2.33009
	Argon, 40	39.9623	3.21573
	TMSO, 75	75	4.33303
	Xenon, 129	129	5.64191
	Xenon, 131	131	5.68304
	Xenon, 132	132	5.70417
	OMTSO, 221	221	7.31213

Table B.4 - Experimental mixture compositions and shock conditions for HRRST experiments.

*P_1 is the driven section initial pressure, P_4 is the driver section pressure as measure, T_5 and P_5 are the reflected shock conditions which are also the reaction conditions. (Battalions used in figures are highlighted)

Battalion #	# of Shocks	Repetition Rate	P_1 Torr	T_1 °C	P_4 Torr	P_5 Torr	T_5 Torr	Ionization Energy eV
0.6% HMDSO in Argon - June 30, 2019								
16	100	1 Hz	370	23	255	1580	9300	12
17	100	1 Hz	370	23	255	1580	9300	11.75
18	100	1 Hz	370	23	255	1580	9300	11.5
19	100	1 Hz	370	23	255	1580	9300	11.25
20	100	1 Hz	370	23	255	1580	9300	11
21	100	1 Hz	370	23	255	1580	9300	10.75
22	100	1 Hz	370	23	255	1580	9300	10.5
23	100	1 Hz	370	23	255	1580	9300	10.25
24	100	1 Hz	370	23	255	1580	9300	10
25	100	1 Hz	370	23	255	1580	9300	9.75
26	100	1 Hz	370	23	255	1580	9300	9.5
27	100	1 Hz	370	23	255	1580	9300	9.25
28	100	1 Hz	370	23	255	1580	9300	9
29	100	1 Hz	370	23	255	1580	9300	8.75
30	100	1 Hz	370	23	255	1580	9300	8.5
31	100	1 Hz	370	23	255	1580	9300	8.25
32	100	1 Hz	370	23	255	1580	9300	8
33	100	1 Hz	370	23	255	1580	9300	7.75
37	100	1 Hz	370	23	255	1580	9300	10.75
38	100	1 Hz	370	23	255	1580	9300	10.5
39	100	1 Hz	370	23	255	1580	9300	10
40	100	1 Hz	370	23	255	1580	9300	9.5
41	100	1 Hz	370	23	255	1580	9300	9
42	100	1 Hz	370	23	255	1580	9300	8.5
43	100	1 Hz	370	23	255	1580	9300	8
44	100	1 Hz	370	23	255	1580	9300	7.75
51	100	1 Hz	215	23	103	1600	4700	12
52	100	1 Hz	215	23	103	1600	4700	11.75
53	100	1 Hz	215	23	103	1600	4700	11.5
54	100	1 Hz	215	23	103	1600	4700	11.25
55	100	1 Hz	215	23	103	1600	4700	11
56	100	1 Hz	215	23	103	1600	4700	10.75
57	100	1 Hz	215	23	103	1600	4700	10.5
58	100	1 Hz	215	23	103	1600	4700	10.25
59	100	1 Hz	215	23	103	1600	4700	10

Battalion #	# of Shocks	Repetition Rate	P_1 Torr	T_1 °C	P_4 Torr	P_5 Torr	T_5 Torr	Ionization Energy eV
60	100	1 Hz	215	23	103	1600	4700	9.75
61	100	1 Hz	215	23	103	1600	4700	9.5
62	100	1 Hz	215	23	103	1600	4700	9.25
63	100	1 Hz	215	23	103	1600	4700	9
64	100	1 Hz	215	23	103	1600	4700	8.75
65	100	1 Hz	215	23	103	1600	4700	8.5
66	100	1 Hz	215	23	103	1600	4700	8.25
67	100	1 Hz	215	23	103	1600	4700	8
68	100	1 Hz	215	23	103	1600	4700	7.75
69	100	1 Hz	215	23	103	1600	4700	10.75
70	100	1 Hz	215	23	103	1600	4700	10.5
71	100	1 Hz	215	23	103	1600	4700	10.25
72	100	1 Hz	215	23	103	1600	4700	10
73	100	1 Hz	215	23	103	1600	4700	9.75
74	100	1 Hz	215	23	103	1600	4700	9.5
75	100	1 Hz	215	23	103	1600	4700	9.25
76	100	1 Hz	215	23	103	1600	4700	9
77	100	1 Hz	215	23	103	1600	4700	8.5
78	100	1 Hz	215	23	103	1600	4700	8
79	100	1 Hz	215	23	103	1600	4700	7.75
83	100	1 Hz	375	23	230	1715	10800	12
84	100	1 Hz	375	23	230	1715	10800	11.75
85	100	1 Hz	375	23	230	1715	10800	11.5
86	100	1 Hz	375	23	230	1715	10800	11.25
87	100	1 Hz	375	23	230	1715	10800	11
88	100	1 Hz	375	23	230	1715	10800	10.75
89	100	1 Hz	375	23	230	1715	10800	10.5
90	100	1 Hz	375	23	230	1715	10800	10.25
91	100	1 Hz	375	23	230	1715	10800	10
92	100	1 Hz	375	23	230	1715	10800	9.75
93	100	1 Hz	375	23	230	1715	10800	9.5
94	100	1 Hz	375	23	230	1715	10800	9.25
95	100	1 Hz	375	23	230	1715	10800	9
96	100	1 Hz	375	23	230	1715	10800	8.75
0.6% TMSO in Argon – June 29, 2019								
8	100	1 Hz	370	23	190	1500	4600	13
9	100	1 Hz	370	23	190	1500	4600	12.75
10	100	1 Hz	370	23	190	1500	4600	12.5
11	100	1 Hz	370	23	190	1500	4600	12.25

Battalion #	# of Shocks	Repetition Rate	P_1 Torr	T_1 °C	P_4 Torr	P_5 Torr	T_5 Torr	Ionization Energy eV
12	100	1 Hz	370	23	190	1500	4600	12
13	100	1 Hz	370	23	190	1500	4600	11.75
14	100	1 Hz	370	23	190	1500	4600	11.5
15	100	1 Hz	370	23	190	1500	4600	11.25
16	100	1 Hz	370	23	190	1500	4600	11
17	100	1 Hz	370	23	190	1500	4600	10.75
18	100	1 Hz	370	23	190	1500	4600	10.5
19	100	1 Hz	370	23	190	1500	4600	10.25
20	100	1 Hz	370	23	190	1500	4600	10
21	100	1 Hz	370	23	190	1500	4600	9.75
22	100	1 Hz	370	23	190	1500	4600	9.5
23	100	1 Hz	370	23	190	1500	4600	9.25
24	100	1 Hz	370	23	190	1500	4600	9
25	100	1 Hz	370	23	190	1500	4600	8.75
26	100	1 Hz	370	23	190	1500	4600	8.5
27	100	1 Hz	370	23	190	1500	4600	8.25
28	100	1 Hz	370	23	190	1500	4600	8
29	100	1 Hz	370	23	190	1500	4600	10.75
30	100	1 Hz	370	23	190	1500	4600	10.5
31	100	1 Hz	370	23	190	1500	4600	10
32	100	1 Hz	370	23	190	1500	4600	9.5
33	100	1 Hz	370	23	190	1500	4600	9
34	100	1 Hz	370	23	190	1500	4600	8.5
35	100	1 Hz	370	23	190	1500	4600	8
61	100	1 Hz	380	23	170	1380	7400	12
62	100	1 Hz	380	23	170	1380	7400	11.75
63	100	1 Hz	380	23	170	1380	7400	11.5
64	100	1 Hz	380	23	170	1380	7400	11.25
65	100	1 Hz	380	23	170	1380	7400	11
66	100	1 Hz	380	23	170	1380	7400	10.75
67	100	1 Hz	380	23	170	1380	7400	10.5
68	100	1 Hz	380	23	170	1380	7400	10.25
69	100	1 Hz	380	23	170	1380	7400	10
70	100	1 Hz	380	23	170	1380	7400	9.75
71	100	1 Hz	380	23	170	1380	7400	9.5
72	100	1 Hz	380	23	170	1380	7400	9.25
73	100	1 Hz	380	23	170	1380	7400	9
74	100	1 Hz	380	23	170	1380	7400	8.75
75	100	1 Hz	380	23	170	1380	7400	8.5

Battalion #	# of Shocks	Repetition Rate	P_1 Torr	T_1 °C	P_4 Torr	P_5 Torr	T_5 Torr	Ionization Energy eV
76	100	1 Hz	380	23	170	1380	7400	8.25
77	100	1 Hz	380	23	170	1380	7400	8
78	100	1 Hz	380	23	170	1380	7400	7.75
79	100	1 Hz	380	23	170	1380	7400	10.75
80	100	1 Hz	380	23	170	1380	7400	10.5
81	100	1 Hz	380	23	170	1380	7400	10
82	100	1 Hz	380	23	170	1380	7400	9.5
83	100	1 Hz	380	23	170	1380	7400	9.25
84	100	1 Hz	380	23	170	1380	7400	9
85	100	1 Hz	380	23	170	1380	7400	8.5
86	100	1 Hz	380	23	170	1380	7400	8.25
87	100	1 Hz	380	23	170	1380	7400	8
88	100	1 Hz	380	23	170	1380	7400	7.75
94	100	1 Hz	240	23	360	1580	9100	12
95	100	1 Hz	240	23	360	1580	9100	11.75
96	100	1 Hz	240	23	360	1580	9100	11.5
97	100	1 Hz	240	23	360	1580	9100	11.25
98	100	1 Hz	240	23	360	1580	9100	11
99	100	1 Hz	240	23	360	1580	9100	10.75
100	100	1 Hz	240	23	360	1580	9100	10.5
101	100	1 Hz	240	23	360	1580	9100	10.25
102	100	1 Hz	240	23	360	1580	9100	10
103	100	1 Hz	240	23	360	1580	9100	9.75
104	100	1 Hz	240	23	360	1580	9100	9.5
105	100	1 Hz	240	23	360	1580	9100	9.25
106	100	1 Hz	240	23	360	1580	9100	9
107	100	1 Hz	240	23	360	1580	9100	8.75
108	100	1 Hz	240	23	360	1580	9100	8.5
109	100	1 Hz	240	23	360	1580	9100	8.25
110	100	1 Hz	240	23	360	1580	9100	8
111	100	1 Hz	240	23	360	1580	9100	7.75
119	100	1 Hz	240	23	360	1580	9100	10.75
120	100	1 Hz	240	23	360	1580	9100	10.5
121	100	1 Hz	240	23	360	1580	9100	10
122	100	1 Hz	240	23	360	1580	9100	9.5
123	100	1 Hz	240	23	360	1580	9100	9
124	100	1 Hz	240	23	360	1580	9100	8.5
125	100	1 Hz	240	23	360	1580	9100	8.25
126	100	1 Hz	240	23	360	1580	9100	8

Battalion #	# of Shocks	Repetition Rate	P_1 Torr	T_1 °C	P_4 Torr	P_5 Torr	T_5 Torr	Ionization Energy eV
127	100	1 Hz	240	23	360	1580	9100	7.75
132	100	1 Hz	230	23	128	1650	5500	12
133	100	1 Hz	230	23	128	1650	5500	11.75
134	100	1 Hz	230	23	128	1650	5500	11.5
135	100	1 Hz	230	23	128	1650	5500	11.25
136	100	1 Hz	230	23	128	1650	5500	11
137	100	1 Hz	230	23	128	1650	5500	10.75
138	100	1 Hz	230	23	128	1650	5500	10.5
139	100	1 Hz	230	23	128	1650	5500	10.25
140	100	1 Hz	230	23	128	1650	5500	10.25
141	100	1 Hz	230	23	128	1650	5500	10
142	100	1 Hz	230	23	128	1650	5500	9.75
143	100	1 Hz	230	23	128	1650	5500	9.5
144	100	1 Hz	230	23	128	1650	5500	9.25
145	100	1 Hz	230	23	128	1650	5500	9
146	100	1 Hz	230	23	128	1650	5500	8.75
147	100	1 Hz	230	23	128	1650	5500	8.5

Table B.5a- TOF-MS settings for HRRST TOF-MS experiments

*Deflect X and Deflect Y are pentiometer settings used to position ions on detector

Battalions	Liner	Lens	Cetnral Grid	Last Grid	Repeller	Extractor	Deflect X	Deflect Y	MCP
0.6% HMDSO - June 30, 2019									
16-33	6990	6900	2450	500	800	800	11.7	3.25	1800
36-44	6990	6900	2450	500	800	800	11.7	3.25	1950
51-68	6990	6900	2450	500	800	800	11.7	3.25	1800
69-79	6990	6900	2450	500	800	800	11.7	3.25	1950
83-96	6990	6900	2450	500	800	800	11.7	3.25	1800
0.6% TMSO - Junr 29, 2019									
8-28	6990	6900	2450	500	800	800	11.7	3.25	1800
29-35	6990	6900	2450	500	800	800	11.7	3.25	2050
61-78	6990	6900	2450	500	800	800	11.7	3.25	1800
79-88	6990	6900	2450	500	800	800	11.7	3.25	2050
94-111	6990	6900	2450	500	800	800	11.7	3.25	1800
119-127	6990	6900	2450	500	800	800	11.7	3.25	2050
132-147	6990	6900	2450	500	800	800	11.7	3.25	1800

Table B.5b- Beamline settings for HRRST TOF-MS experiments

Battalions	MgF	M2	M3	HBDA Width	HBDA Pos	VBDA Width	VBDA Pos	M4 Yaw	M4 Roll
0.6% HMDSO - June 30, 2019									
16-33	No	-4.2006	-46.20933	4.0	0.0	6.0	0.0	-1.1565	-0.04994
36-44	Yes	-4.2004	-46.20933	4.0	0.0	6.0	0.0	-1.1565	-0.04994
51-68	No	-4.2004	-46.20933	4.0	0.0	6.0	0.0	-1.1565	-0.04994
69-79	Yes	-4.2004	-46.20933	4.0	0.0	6.0	0.0	-1.1565	-0.04994
83-96	No	-4.2004	-46.20933	4.0	0.0	6.0	0.0	-1.1565	-0.04994
0.6% TMSO - June 29, 2019									
8-28	No	-4.2004	-46.2095	4.0	0.0	6.0	0.0	-1.1600	-0.04994
29-35	Yes	-4.2004	-46.2095	4.0	0.0	6.0	0.0	-1.1600	-0.04994
61-78	No	-4.2004	-46.2095	4.0	0.0	6.0	0.0	-1.1600	-0.04994
79-88	Yes	-4.2004	-46.2095	4.0	0.0	6.0	0.0	-1.1600	-0.04994
94-111	No	-4.2004	-46.2095	4.0	0.0	6.0	0.0	-1.1600	-0.04994
119-127	Yes	-4.2004	-46.2095	4.0	0.0	6.0	0.0	-1.1500	-0.04994
132-147	No	-4.2004	-46.2095	4.0	0.0	6.0	0.0	-1.1500	-0.04994

Table B.6a- Product mass peaks identified for 0.5% HMDSO in Ar/Neon (2%/97.5%) with their appearance times (in reaction time) for DFST TOF-MS experiments at 1610 K & 185 Torr

*Mass peaks known to be associated with HMDSO, argon, and neon were not tabulated as they were identified in the pre-shock region

m/z	Appearance time us
2	20
15	35
16	35
25	60
26	35
27	35
28	20
29	40

Table B.6b- Product mass peaks identified for 0.5% TMSO in Ar/Neon (2%/97.5%) with their appearance times (in reaction time) for DFST TOF-MS experiments at 1410 K & 155 Torr

*Mass peaks known to be associated with TMSO, HMDSO, argon, and neon were not tabulated as they were identified in the pre-shock region

m/z	Appearance time us
2	65
15	40
16	40
25	40
26	50
27	41
28	25
29	40
207	50

Table B.7a- Species used for m/z calibration for analysis of siloxane data collected at the ALS

*m/z listed here are the widely accepted values reported in literature

Species	TOF us	m/z
H2O	2.36504	31.999
O2	3.08298	18.015
TMSO	4.61087	75.161
TMSO	5.03108	90.196

Table B.7b- Mass peaks identified for HMDSO with their appearance times (in reaction time) and ionization energy of first appearance with and without the MgF_2 window for HRRST experiments at 1580 K & 12.2 atm

*Due to higher harmonic light leakage, ionization energies cannot be determined for experiments without the MgF_2 window. Determination of non-trivial higher harmonic light comes from the ability to detect water, oxygen, and argon in the preshock for battalions with ionization energies as low as 7.75 eV

HMDSO Species (with MgF2 window)								
m/z	Appearance time us	Ionization Energy eV	m/z	Appearance time us	Ionization Energy eV	m/z	Appearance time us	Ionization Energy eV
28.2	70	10.5	75.3	60	9	149.3	0	7.75
29.2	100	10.5	78.3	60	9.5	150.3	0	7.75
39.2	75	7.75	117.3	65	9	151.2	0	8
40.2	65	8.5	118.3	65	10.5	152.2	0	8
41.2	110	8.5	131.3	60	10.5	153.3	0	8
42.2	55	8.5	132.3	52	8.5	154.3	0	8
43.2	110	8.5	133.3	60	9.5	155.3	0	8
50.2	110	10.5	134.4	0	9	162.3	0	7.75
52.3	81	9.5	146.3	57	9	163.3	0	8
54.3	78	9	147.3	0	7.75	164.3	0	8
73.3	60	8.5	148.3	0	7.75	165.3	0	8
HMDSO Species (no MgF2 window)								
15.03	100		73.3	0		153	0	
16.05	70		75.3	0		154	0	
18.04	0		78.3	94		155	0	
20	60		103.3	39		156	0	
26.1	65		104.3	39		157	0	
27.1	67		117.3	42		158	0	
28.1	44		118.3	42		162.3	0	
29.2	67		119.3	42		163.3	0	
30.2	55		120.3	50		164.4	0	
32.1	0		131.3	0		165.3	0	
39.2	70		132.3	43		191.3	95	
40.2	0		133.3	0		205.2	88	
41.2	45		134.4	0		206.2	88	

m/z	Appearance time us	Ionization Energy eV	m/z	Appearance time us	Ionization Energy eV	m/z	Appearance time us	Ionization Energy eV
41.2	45		134.4	0		206.2	88	
42.2	0		135.2	0		207.2	88	
50.3	92		146.33	45		221.3	52	
52.3	75		147.33	0		234.1	135	
54.3	68		148.33	0				
56.3	0		149.3	0				
57.3	0		150.3	0				
58.7	0		151.2	0				
59.3	55		152	0				

Table B.7c- Mass peaks identified for TMSO with their appearance times (in reaction time) and ionization energy of first appearance with and without the MgF_2 window for HRRST experiments at 1580 K & 12.0 atm

*Due to higher harmonic light leakage, ionization energies cannot be determined for experiments without the MgF_2 window. Determination of non-trivial higher harmonic light comes from the ability to detect water, oxygen, and argon in the preshock for battalions with ionization energies as low as 7.75 eV

TMSO Species (with MgF2 window)								
m/z	Appearance time us	Ionization Energy eV	m/z	Appearance time us	Ionization Energy eV	m/z	Appearance time us	Ionization Energy eV
28.1	99	10.5	103.5	90	10	150.6	0	7.75
40.2	140	8.5	104.5	80	9	151.6	147	7.75
52.3	164	8.5	132.6	89	8	152.6	147	7.75
54.3	164	9.5	133.5	138	8	162.8	0	9
58.3	164	10	134.5	138	8	163.8	0	9.5
75.3	0	7.75	146.6	93	9.5	164.8	0	9.5
76.3	0	9.5	147.6	0	7.75	207.9	105	8
77.3	0	8.5	148.6	0	7.75	235	156	10.5
90	0	7.75	149.6	0	7.75	251	160	9.5

TMSO Species (no MgF2 window)								
m/z	Appearance time us	Ionization Energy eV	m/z	Appearance time us	Ionization Energy eV	m/z	Appearance time us	Ionization Energy eV
16.1	90		103	0		208	91	
18.04	0		104	0		209	91	
20	80		105	80		220	175	
25	225		117	77		221.3	92	
26.1	70		118	77		222	92	
27.1	105		119	91		223	82	
28.1	20		131.3	69		235	125	
29.2	84		132.3	75		236	125	
30.2	65		133.3	75		237	125	
31	97		134.4	45		238	125	
32.1	0		135.2	78		239	125	
39.2	166		136	78		251	112	
40.2	0		146.33	84		252	112	
41.2	45		147.33	0		253	112	
42.2	108		148.33	0		254	112	
45	67		149.3	0		265	120	
46	67		150.3	0		266	120	
47	67		151.2	0		267	120	
50	195		152	0		268	120	
52	118		153	0		269	120	
54	118		154	0		282	100	
56	110		155	0				
58	0		156	0				
59	109		157	0				
60	75		158	0				
73	95		162.3	0				
74	95		163.3	0				
75	0		164.4	0				
76	0		165.3	0				
77	0		191.3	92				
78	0		192.3	92				
79	0		193.2	92				
90	0		205	100				
91	0		206	100				
92	0		207.2	78				